



저작자표시-비영리-변경금지 2.0 대한민국

이용자는 아래의 조건을 따르는 경우에 한하여 자유롭게

- 이 저작물을 복제, 배포, 전송, 전시, 공연 및 방송할 수 있습니다.

다음과 같은 조건을 따라야 합니다:



저작자표시. 귀하는 원저작자를 표시하여야 합니다.



비영리. 귀하는 이 저작물을 영리 목적으로 이용할 수 없습니다.



변경금지. 귀하는 이 저작물을 개작, 변형 또는 가공할 수 없습니다.

- 귀하는, 이 저작물의 재이용이나 배포의 경우, 이 저작물에 적용된 이용허락조건을 명확하게 나타내어야 합니다.
- 저작권자로부터 별도의 허가를 받으면 이러한 조건들은 적용되지 않습니다.

저작권법에 따른 이용자의 권리는 위의 내용에 의하여 영향을 받지 않습니다.

이것은 [이용허락규약\(Legal Code\)](#)을 이해하기 쉽게 요약한 것입니다.

[Disclaimer](#)

공학박사학위논문

**스파크제트 액츄에이터의 주파수와 성능
특성에 대한 수치해석 연구**

**Numerical Investigation on Frequency and
Performance Characteristics of SparkJet Actuator**

2021 년 2 월

서울대학교 대학원

기계항공공학부

김 형 진

스파크제트 액추에이터의 주파수와 성능 특성에 대한 수치해석 연구

Numerical Investigation on Frequency and
Performance Characteristics of SparkJet Actuator

지도교수 김 규 홍

이 논문을 공학박사 학위논문으로 제출함

2021 년 2 월

서울대학교 대학원

기계항공공학부

김 형 진

김형진의 공학박사 학위논문을 인준함

2020 년 12 월

위 원 장 : 이 관 중

부위원장 : 김 규 홍

위 원 : 도 형 록

위 원 : 신 지 천

위 원 : 김 민 기

Abstract

Numerical Investigation on Frequency and Performance Characteristics of SparkJet Actuator

Hyung-Jin Kim

Department of Aerospace Engineering

The Graduate School

Seoul National University

Conventional flow control devices are not widely utilized in high speed flow regimes such as supersonic flow since they rarely have effects on. Plasma actuators show greater effects on such regimes compared to other flow control devices because they use both momentum and heat transfer to perturb surrounded flow. Among them, a SparkJet actuator, which is a kind of synthetic jet actuator, has gathered interests for potentials to be used in high speed flow control because it ejects jet flow and pressure waves while having a relatively simple structure without mechanically moving parts. A lot of investigations are conducted, but many of them are limited to qualitative studies. So far, the characteristics of a SparkJet actuator is not fully understood yet, and studies regarding the quantitative analyses are lacking.

Thus, in the present study, qualitative and quantitative numerical investigations on SparkJet actuator is conducted by using three dimensional unsteady Navier – Stokes equation solver capable of analyzing equilibrium plasma. To this end, jet flow

characteristics of a SparkJet actuator is analyzed. Thrust and total impulse performance characteristics are analyzed and natural frequencies of the actuator are confirmed by conducting Fast Fourier transform (FFT) of thrust. Their origins are found through flow patterns inside the cavity, and effects on the performance characteristics are investigated. In addition, influences of design variables on performance characteristics are analyzed through parametric studies. The following conclusions are reached.

The flow of SparkJet actuator has nonequilibrium phenomena at the beginning of energy deposition stage, but equilibrium flow analysis secures the accuracy with reduced computational time costs. During the jet flow ejection, pressure waves are exhausted intermittently which makes a lot of oscillations in thrust. These cause thrust loss and negative thrust, while total impulse increases nearly monotonically in overall, then level offs to a certain value. Two natural frequencies of SparkJet actuator are confirmed by FFT of thrust. These are originated from the pressure wave behaviors inside the cavity. The higher natural frequency is named as the first natural frequency f_1 , and the second natural frequency f_2 for the lower one.

By changing the electrode shape and taper angle, following frequency characteristics of SparkJet actuator are confirmed. The reflected pressure waves in the $r - axis$ direction is the origin of the first natural frequency f_1 , and the reflected pressure waves in the $z - axis$ direction is responsible for the second natural frequency f_2 . The two natural frequencies are independent from each other which is named direction separable property. Total impulse is decreased by approximately 11 % when the first natural frequency f_1 is removed, and by approximately 15 % when the most of the oscillations are removed. It is concluded that consideration of oscillations is required for the predictions and/or estimations of

performance, and application of the actuator into a system.

Parametric studies regarding the performance characteristics of SparkJet actuator are conducted for the effects of design variables. Electrode shape affects total impulse up to approximately 3 %. This is caused by the disappearance of the reflected pressure waves in the $r - axis$ direction. The aspect ratio of energy deposition region close to unity is good for the total impulse of the actuator. Related design variables are electrode diameter, electrode gap, and cavity diameter. Taper angle changes total impulse up to approximately 16 %. Flow expansion and separation around the cavity upper wall and orifice throat cause reduction in the orifice throat area so that the mass flow is reduced for the too small taper angle cases. Taper angle variation results in leakage of high temperature flow so that the energy for driving force of the actuator is lost. The high temperature outflow is enhanced by out of phase resonance of pressure wave behaviors inside the cavity. The in phase resonance effects are expected to trap high temperature flow inside the cavity, and thus have positive effects on the performance. The resonance effects are related to the ratio of the natural frequencies and ratio of cavity diameter to height. Orifice diameter affects approximately up to 20 % of total impulse. Mass flow increases with respect to the orifice area. However, pressure drops after pressure waves ejections are also increased so that total impulse is even decreased in some period. These parametric studies provide fundamental considerations for designing of SparkJet actuator.

Keywords: Flow control, Plasma flow control, Plasma actuator, SparkJet actuator, Performance characteristics, Frequency characteristics, Computational Fluid Dynamics

Student Number: 2016-30184

Student Name: Kim, Hyung-Jin

Table of Contents

| | |
|--|-------------|
| Abstract..... | I |
| Table of Contents..... | IV |
| Nomenclature..... | VI |
| List of figure..... | X |
| List of tables..... | XIII |
| Chapter 1. Introduction | 1 |
| 1.1 Overview of SparkJet Actuator..... | 1 |
| 1.2 Previous Research..... | 5 |
| 1.3 Objectives and Scope of the Dissertation | 9 |
| Chapter 2. Physical Model..... | 11 |
| 2.1 Governing Equation..... | 11 |
| 2.2 Non – dimensionalization of Governing Equation | 14 |
| 2.3 Gas Dynamic Model | 17 |
| 2.4 Plasma Energy Deposition Model | 31 |
| Chapter 3. Numerical Method and Validations | 33 |
| 3.1 Numerical Methods | 33 |
| 3.2 Validations | 41 |
| Chapter 4. Numerical Analysis of Baseline Model..... | 54 |
| 4.1 Jet Flow Characteristics | 55 |
| 4.2 Performance Characteristics | 60 |
| 4.3 Frequency Characteristics..... | 66 |
| 4.4 Pressure Wave Behaviors Inside the Cavity | 70 |
| Chapter 5. Numerical Analysis of Frequency Characteristics..... | 76 |
| 5.1 Oscillations in the $r - axis$ direction: Electrode Shape..... | 78 |
| 5.2 Oscillations in the $z - axis$ direction: Taper Angle | 85 |
| 5.3 Effects of Oscillations on the Performance | 90 |
| 5.4 Summary..... | 93 |

| | |
|--|------------|
| Chapter 6. Numerical Analysis of Performance Characteristics..... | 95 |
| 6.1 Electrode Shape | 96 |
| 6.2 Taper Angle..... | 101 |
| 6.3 Electrode Height | 116 |
| 6.4 Orifice Diameter | 126 |
| 6.5 Summary..... | 132 |
| Chapter 7. Conclusions | 137 |
| 7.1 Summary..... | 137 |
| 7.2 Contribution..... | 141 |
| 7.3 Future Works..... | 145 |
| Reference..... | 148 |
| 국문 초록 | 154 |

Nomenclature

English symbols

| | |
|----------------|--|
| A | Area |
| a | Number of kilogram – atoms per kilogram – mole |
| b | Number of kilogram – atoms in per kilogram |
| c | Speed of sound |
| c_p | Specific heat capacity at constant pressure |
| c_v | Specific heat capacity at constant volume |
| E | Energy |
| E | Convective flux vector of x direction |
| E_v | Viscous flux vector of x direction |
| e | Energy |
| e_{hof} | Heat of formation energy |
| $e_{internal}$ | Internal energy |
| $e_{kinetic}$ | Kinetic energy |
| e_t | Total energy |
| F | Helmholtz free energy |
| F | Convective flux vector of y direction |
| F | Numerical flux |
| F_v | Viscous flux vector of y direction |
| f | Helmholtz free energy per kilogram |
| f | Pressure – weighted function |
| f_1 | First natural frequency |
| f_2 | Second natural frequency |
| G | Gibbs free energy |
| G | Convective flux vector of z direction |
| G_v | Viscous flux vector of z direction |
| g | Gibbs free energy per kilogram |
| H | Total enthalpy |
| I_{aver} | Average total impulse |

| | |
|--------------|---------------------------------|
| I_{total} | Total impulse |
| J | Jacobian |
| Q | Conservative vector |
| Q | Heat |
| R | Residual vector |
| \dot{q}_x | Heat transfer in x direction |
| \dot{q}_y | Heat transfer in y direction |
| \dot{q}_z | Heat transfer in z direction |
| s | Entropy |
| L | Characteristic length |
| M | Molecular weight |
| M | Mach number |
| Ma | Mach number |
| m | Mach number |
| \dot{m} | Mass flow rate |
| n | Number of kilogram – moles |
| Pr | Prandtl number |
| p | Pressure |
| R | Universal gas constant |
| Re | Reynolds number |
| S | Source term vector |
| S_{plasma} | Energy deposition by plasma |
| S_{joule} | Joule heating energy |
| S_{rad} | Radiation energy |
| T | Thrust |
| T | Temperature |
| T_e | Temperature of electron |
| T_g | Temperature of gas |
| T_i | Temperature of ion |
| T_n | Temperature of neutral particle |
| t | Time |
| U | Velocity in x direction |

| | |
|-----|---------------------------|
| u | Velocity in x direction |
| V | Volume |
| V | Velocity |
| V | Velocity in y direction |
| v | Velocity in y direction |
| w | Velocity in z direction |
| x | Mole fraction |

Greek symbols

| | |
|-----------|--|
| α | Number of kilogram – atoms |
| α | Stoichiometric coefficient |
| γ | Specific heat ratio |
| η | Energy transfer efficiency |
| θ | |
| κ | |
| λ | Lagrangian multiplier |
| μ | Viscosity |
| μ | Chemical potential per kilogram – mole |
| ρ | Density |
| τ | Viscous shear stress |
| Φ | Flux vector |
| ϕ | Viscosity interaction coefficient |
| ϕ | Flux vector |
| ψ | Interaction coefficient |

Subscripts

| | |
|-------|-------------------|
| fr | Frozen |
| irr | Irreversible |
| L | Left side of cell |
| m | Maximum |
| n | Normal |

| | |
|------------|--------------------|
| <i>ori</i> | Orifice |
| <i>R</i> | Right side of cell |
| <i>re</i> | Reaction |
| <i>rev</i> | Reversible |
| ∞ | Freestream value |
| $1/2$ | Cell interface |
| 0 | Initial state |

Superscripts

| | |
|---|---|
| * | Non – dimensionalized value |
| * | Critical |
| + | Across cell interface in positive direction |
| – | Across cell interface in negative direction |

Abbreviations

| | |
|--------|---|
| ANOVA | An Analysis of Variance |
| AUSM | Advection Upstream Splitting Method |
| AUSMPW | Advection Upstream Splitting Method by pressure based weight function |
| CEA | Chemical Equilibrium with Application |
| CFD | Computational Fluid Dynamics |
| DOE | Design of Experiments |
| Exp | Experiment |
| FFT | Fast Fourier transformation |
| MUSCL | Monotonic Upstream – centered Scheme for Conseravtion Laws |
| NG | Number of gases |
| NM | Number of gaseous species for the calculations |
| NR | Number of reactions |
| NS | Number of species |
| TVD | Total variation diminishing |

List of figure

| | |
|---|----|
| Figure 1.1 Examples for plasma actuator applications..... | 2 |
| Figure 1.2 Schematic of SparkJet actuator. | 4 |
| Figure 1.3 SparkJet actuator operating mechanism and its configuration. | 4 |
| Figure 2.1 Pressure and temperature relation for electron and heavy particles [45]. | 18 |
| Figure 2.2 Comparison of viscosity calculated by CEA and Sutherland's law. | 29 |
| Figure 2.3 Comparison of thermal conductivity calculated by CEA and Sutherland's law. | 30 |
| Figure 3.1 Example of jet front position comparison. | 41 |
| Figure 3.2 Configuration of a SparkJet actuator. | 43 |
| Figure 3.3 Computational domain and the grid system. | 44 |
| Figure 3.4 Voltage across the capacitor and current of the discharge [62]. | 45 |
| Figure 3.5 Time history of energy deposition applied as a source term. ONERA case. | 46 |
| Figure 3.6 Density and pressure fields of SparkJet actuator: | 47 |
| Figure 3.7 Comparison of jet front positions for validation. ONERNA case [22]. . | 47 |
| Figure 3.8 Time history of applied voltage and current. Ulsan Univ. case..... | 50 |
| Figure 3.9 Time history of Joule heating energy. Ulsan Univ. case. | 50 |
| Figure 3.10 Comparison of jet front positions for validation. Ulsan Univ.case. | 51 |
| Figure 3.11 Schlieren images from experiment and density flow field from CFD. . | 52 |
| Figure 4.1 Density fields of SparkJet actuator: | 57 |
| Figure 4.2 Jet front positions comparison of equilibrium gas and calorically perfect gas [22]. | 57 |
| Figure 4.3 Density contour and streamlines at 60 μs | 59 |
| Figure 4.4 Thrust and total impulse of baseline. | 61 |
| Figure 4.5 Flow fields near orifice: (a) pressure contour, (b) Z direction velocity contour and streamlines. | 64 |
| Figure 4.6 Fast Fourier Transform of thrust: (a) full range and region I, (b) full range and region II, (c) full range and region III. | 69 |
| Figure 4.7 Schematic diagram of the reflected pressure wave inside the cavity: (a) The r – axis direction, (b) The z – axis direction.. | 71 |
| Figure 4.8 Pressure contour of baseline at z = 0.002 | 73 |
| Figure 4.9 Pressure contour of baseline at x = 0 | 74 |
| Figure 4.10 Fast Fourier transform of thrust for different energy depositions. | 75 |
| Figure 5.1 The configurations of energy deposition for different electrode shape.. | 78 |
| Figure 5.2 Full range Fast Fourier transform of thrust for different electrode shape. | 80 |
| Figure 5.3 Fast Fourier transform of thrust for different electrode shape: (a) region I, (b) region II, (c) region III. | 81 |
| Figure 5.4 Pressure contour and streamline for different electrode shape: (a) baseline, | |

| | |
|--|-----|
| (b) case A, (c) case B, (d) case C | 84 |
| Figure 5.5 The configurations of cavity for different taper angle..... | 85 |
| Figure 5.6 Full range Fast Fourier transform of thrust for different taper angle. | 86 |
| Figure 5.7 Fast Fourier transform of thrust for different taper angle: (a) region I, (b) region II, (c) region III. | 89 |
| Figure 5.8 Thrust and total impulse of baseline and their smoothing results. | 91 |
| Figure 6.1 Thrust and total impulse for different electrode shape..... | 98 |
| Figure 6.2 Cavity average pressure for different electrode shape. | 99 |
| Figure 6.3 Total impulse and average total impulse comparison for different electrode shape. | 100 |
| Figure 6.4 Thrust and total impulse for different taper angle..... | 102 |
| Figure 6.5 Cavity average pressure for different different taper angle..... | 103 |
| Figure 6.6 Total impulse, average total impulse, and max average pressure comparison for different electrode shape..... | 103 |
| Figure 6.7 Effect of the taper angle on flow structure: (a) Smooth flow in the baseline, (b) the stagnation point in case D, and (c) the flow expansion, stagnation point, and narrowed flow path in case D..... | 105 |
| Figure 6.8 Temperature contour and streamlines of case D at 40 μs and 60 μs | 107 |
| Figure 6.9 Temperature contour and streamlines of case E at 40 μs and 60 μs | 107 |
| Figure 6.10 Temperature contour and streamlines of case F at 40 μs and 60 μs | 107 |
| Figure 6.11 Temperature contour and streamlines of baseline at 40 μs and 60 μs | 108 |
| Figure 6.12 Cavity average temperature for case D and E. | 108 |
| Figure 6.13 Natural frequency and length ratios and their differences..... | 111 |
| Figure 6.14 Velocity contour in y and z direction for case E at 35 μs | 111 |
| Figure 6.15 Velocity contour in y and z direction for case E at 40 μs | 112 |
| Figure 6.16 Velocity contour in y and z direction for case E at 45 μs | 112 |
| Figure 6.17 Velocity contour in y and z direction for case E at 40 μs | 112 |
| Figure 6.18 The pressure total impulse component and the differences of ratio... | 113 |
| Figure 6.19 Enlarged thrust and total impulse of baseline and G..... | 114 |
| Figure 6.20 Thrust and total impulse for different electrode height. | 117 |
| Figure 6.21 Cavity average pressure for different different electrode height..... | 118 |
| Figure 6.22 Temperature contour of case H at 60 μs | 120 |
| Figure 6.23 Temperature contour of baseline at 60 μs | 120 |
| Figure 6.24 Temperature contour of case I at 60 μs | 121 |
| Figure 6.25 Momentum total impulse for different electrode height. | 121 |
| Figure 6.26 Full range Fast Fourier transform of thrust for different eletrode height. | 122 |
| Figure 6.27 Fast Fourier transform of thrust for different electrode height: (a) region | |

| | |
|--|-----|
| I, (b) region II, (c) region III. | 125 |
| Figure 6.28 Thrust and total impulse for different orifice diameter. | 127 |
| Figure 6.29 Momentum total impulse for different orifice diameter. | 128 |
| Figure 6.30 Cavity average pressure for different orifice diameter. | 129 |
| Figure 6.31 Cavity average density for different orifice diameter. | 129 |
| Figure 6.32 Pressure thrust for different orifice diameter. | 130 |
| Figure 6.33 Pressure total impulse for different orifice diameter. | 130 |
| Figure 6.34 Average total impulse with respect to electrode shape. | 135 |
| Figure 6.35 Average total impulse with respect to taper angle. | 135 |
| Figure 6.36 Average total impulse with respect to electrode height. | 136 |
| Figure 6.37 Average total impulse with respect to orifice diameter. | 136 |
| Figure 7.1 Coparison of performance between the models and CFD. | 143 |
| Figure 7.2 Comparison of velocity at orifice exit between the models and CFD.. | 144 |

List of tables

| | |
|--|-----|
| Table 3.1 Design variables of ONERA case..... | 42 |
| Table 3.2 Design variables of Ulsan University case. | 48 |
| Table 5.1 Designe variables for Frequency Characteristics Analysis. | 77 |
| Table 5.2 Comparison of the natural frequencies for different electrode shape. | 80 |
| Table 5.3 Comparison of the natural frequencies for different taper angle. | 86 |
| Table 5.4 Effect of oscillations on the performance | 91 |
| Table 6.1 Thrust and average total impulse for different electrode shape. | 97 |
| Table 6.2 Thrust and average total impulse for different taper angle. | 102 |
| Table 6.3 Frequency ratios, length ratios, and their differences. | 110 |
| Table 6.4 Design variables for performance characteristics analysis for electrode height..... | 116 |
| Table 6.5 Thrust and average total impulse for different electrode height. | 117 |
| Table 6.6 Design variables for performance characteristics analysis for orifice diameter. | 126 |
| Table 6.7 Thrust and average total impulse for different orifice diameter..... | 127 |

Chapter 1. Introduction

1.1 Overview of SparkJet Actuator

Many kinds of active and passive flow control devices are used widely to improve aerodynamic performances and efficiency of aircrafts by altering the flow field [1]. Typical applications of such devices include drag reduction, lift enhancement, mixing augmentation, noise suppression, and many more. Passive flow control devices are usually involved in the geometrical configuration of vehicle itself, such as vortex generator, wing tip, cavity, guided vane, and etc. Thus, they are unable to change their roles depending on the situations of flow field. On the other hands, active flow control devices can be operated regarding the states of flow field according to the intention of an operator. They disturb the flow field by exerting momentum and/or energy. Devices such as synthetic jet, suction/blow, surface heater and various kinds of actuators exist. Among them, plasma actuators are widely investigated as a promising flow control device because of their own physical properties and advantages over others. This actuator utilizes plasma so that both of momentum and energy transfer, generated by electric field and Joule heating [2, 3], are able to be used for flow control. By these aspects, they have more capacity on controlling high speed flow due to the perturbing the flow more effectively compared to other devices. Several kinds of plasma actuators are already investigated on controlling the supersonic flows [4-7]. Figure 1.1 shows some of their possible applications for any of flow regimes [5, 8-10]. Figure 1.1 (a) show plasma actuator

used in flow separation control in subsonic flow. Also, plasma actuator used in transonic tip clearance flow control is shown in Figure 1.1 (b). In Figure 1.1 (c) and (d), plasma actuators show effectiveness in supersonic flow control. Plasma actuators also have advantages such as; relatively simple structure with no mechanically moving parts, and does not intrude into the flow field. They can be pasted on the surface or buried so that unfavorable aerodynamic drag, aerodynamic heating, and shock waves can be reduced. Among many kinds of plasma actuators, a SparkJet actuator is widely investigated for a couple of decades thereafter.

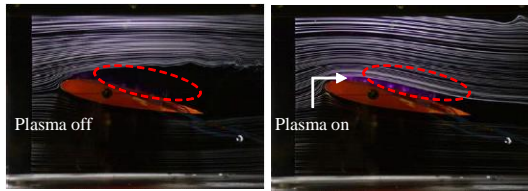


Figure 1.1 (a) Separation control [8].

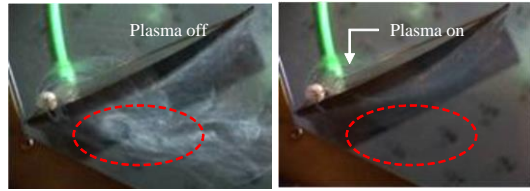


Figure 1.1 (b) Tip clearance flow control [9].

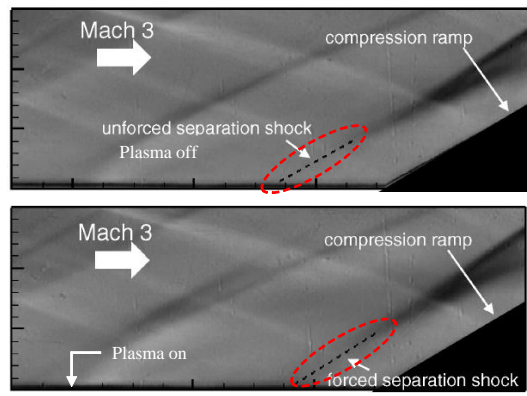
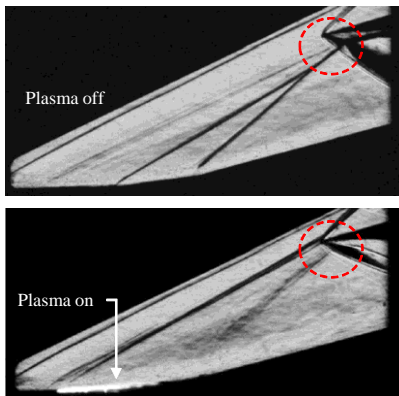


Figure 1.1 (d) Inlet shock wave control [5]. Figure 1.1 (c) Supersonic separation control [10].

Figure 1.1 Examples for plasma actuator applications

A SparkJet actuator utilizes plasma to generate pressure wave (or sometimes shock wave) and momentum jet flow. This device belongs to a family of synthetic jet actuator since jet flow is ejected from a cavity through an orifice. Its schematic

view of perturbing external flow field is shown in Figure 1.2. Unlike from other kinds of synthetic jet actuators, SparkJet actuator exhausts not only jet flow but also pressure wave because of its unique operating mechanism. The three – stage operating mechanism and typical configuration of a SparkJet actuator is shown in Figure 1.3. There is a pair of electrodes placed inside a cavity. When voltage higher than the breakdown voltage is applied onto the electrodes, a plasma is generated and it deposits energy onto the air around it. This is the first stage called the energy deposition stage. The second stage is called the discharge stage. By energy deposition, pressure and temperature inside the confined cavity increase. Given enough time, pressure wave and jet flow discharge through an orifice which faces outwards. By these exhausting physical aspects, SparkJet actuator disturbs external flow fields. Due to these ejections, the pressure and density of cavity becomes lower than the outside. Then, the third stage starts which is called the refresh stage. Since the reverse pressure and density is formed inside the cavity, air flows back into the cavity. Basically, this whole process is done without refilling the cavity so that it is a zero – net – mass – flow synthetic jet device. Some applications of having a couple of electrodes, having three electrodes one for trigger [11, 12], and multiple orifices [13, 14] are also possible.

As one kind of synthetic jet actuator, SparkJet actuator has its own advantages including those of plasma actuator mentioned earlier so that the actuator can be used for a variety of flow control including general situations such as flow separation control, drag reduction, lift enhancement, and so on. This actuator is capable of making supersonic jet flow. Also it is a reusable actuator that can be operated repetitively. These aspects make it possible for SparkJet actuator to be applied as a replacement of side jet or rocket motor used in supersonic vehicle such as launch

vehicle and missile for reaction control system. Since the actuator is reusable, cost reduction is expected when it is applied on the reusable launch vehicle. In addition, it can replace the control surface of fixed – wing aircrafts so that their structure and configuration would be simplified.

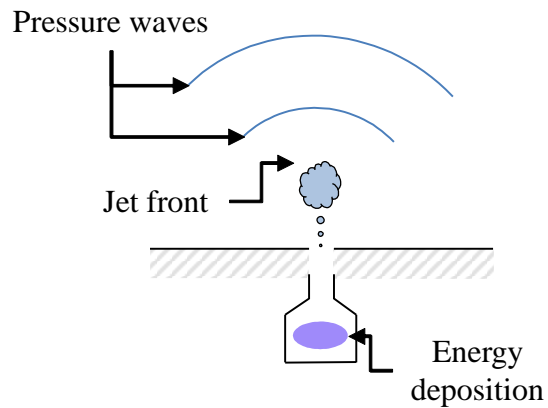


Figure 1.2 Schematic of SparkJet actuator.

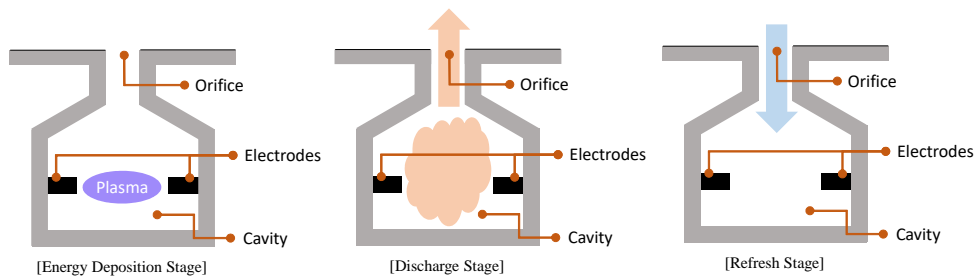


Figure 1.3 SparkJet actuator operating mechanism and its configuration.

1.2 Previous Research

The SparkJet actuator was first proposed by research team of Johns Hopkins University Applied Physics Laboratory (JHU – APL) in 2003 [15, 16]. In the very first paper, the concept of the actuator was introduced by computational and experimental approach. Possible application in high speed flow control was presented based on the fact that a SparkJet actuator produces relatively high speed jet flow compared to existing micro – actuator jets. The research team targeted development of a micro – actuated flow control system for enhanced aerodynamic performance of small, highly maneuverable, high – speed vehicle as an ultimate goal. Thereafter, JHU – APL research team progressed several investigations. They used particle image velocimetry (PIV) techniques to measure peak velocity in the entrained jet flow which showed 53 m/s . Also, digital speckle tomography (DST) technique was used to measure peak temperature of jet flow which showed 1616.3 K [17]. However, they had difficulties in seeding the particles for PIV method due to the smallness of the actuator and both PIV and DST method are limited to two dimensional plane. They developed an analytic model assuming an isentropic process for a SparkJet actuator which calculates peak temperature and pressure inside the cavity so that pressure, temperature, and density of orifice and orifice exit velocity can be predicted [18]. They concluded that maximum efficiency of their device was 35% based on the cavity pressure when experimental results are compared to computational results. However, the model was not able to predict the behavior of the actuator in the refresh stage which might be a weakness in considering repetitive actuation. Later, they modified the model to consider the refresh stage[19]. Together with Florida State University's Center for Aero –

Propulsion (FSU – FCAAP), JHU – APL tested a SparkJet actuator on a flat plate around a Mach 1.5 crossflow [14]. The results revealed that 5° of flow deflection angle was created by the actuator. JHU – APL proposed and started the research on the SparkJet actuator and showed its potential application on flow control. However, their efforts were mostly limited to qualitative studies based on experiment.

ONERA also tried to investigate a SparkJet actuator in a wide range of fields [20], then performed detailed research one by one. They tested the effects for two kinds of power supplies, in particular on the role of the rate of energy dissipation of plasma [21]. The two kinds of power supplies are inductive power supply (IPS) and capacitive power supply (CPS). They concluded that the CPS type produces more powerful jet flow, which means higher velocity in shorter expulsion time. Also, gas and cavity heating were less significant than the IPS type. They also established physical model for computational analysis which uses “real” gas physics [22]. An arc plasma used in a SparkJet actuator is usually known as equilibrium plasma. Thus, they used equilibrium gas thermodynamic model to consider thermal and chemical properties of plasma. Not only that, ONERA reflected the energy terms related to the plasma physically; Joule heating energy and radiation loss. Both of the terms were added in energy balance equation of Navier – Stokes equation. When calculating the Joule heating energy, the RLC circuit equation was used. Meanwhile, tables for radiative energy depending on temperature and pressure was used. They verified their physical assumptions by comparing the jet front positions with respect to time from Schlieren images taken from experiment [23]. ONERA made great strides in the numerical simulation of a SparkJet actuator by considering some of practical physical aspects. However, their analyses were not detailed enough to take advantage of a computational analysis, which could reveal more diverse, complex, and detailed

physical phenomena.

A research group at the University of Texas at Austin conducted a number of experiments both in a quiescent air and Mach 3 supersonic flow environments. In a quiescent air experiment, they found that a certain amount of time should be secured for refresh stage so that cavity is enough of air that plasma is stably discharged when actuated by repetitive pulses [4]. Thus, there must exist a certain frequency for a repetitive actuation that stemmed from geometric configurations of a SparkJet actuator. Their optical emission spectroscopy measurement revealed the presence of nonequilibrium effects between rotational and vibrational mode in the SparkJet actuator flow. Also, the gas heating efficiency of plasma was 10 %. They measured the penetration distance of a SparkJet actuator using Schlieren image in their first experiment in Mach 3 crossflow, which penetrated 1.5 times of boundary layer thickness. In other experiments, they controlled the shock/boundary layer interaction generated by a compression ramp in a Mach 3 flow [7, 10, 24]. They found that the actuator was effective for shifting the frequencies of oscillation of the separated flow which was formed ahead of a compression ramp. Also, surface pressure was decreased due to the actuations. They concluded that a SparkJet actuator is an effective control device to avoid structural – panel resonance by shifting the dominant frequencies of oscillation of the separated flow to other frequency band. However, the most of the investigations are limited to qualitative using Schlieren image.

Lately, research teams in China conducted a variety of studies for a SparkJet actuator. Especially, research teams at Air Force Engineering University and Xi'an Jiaotong University collaborated together. They investigated distinguishable flow patterns and jet flow characteristics of a SparkJet actuator according to capacitor

input energy [25] and geometry [26]. Also, an analytic model was developed considering heat transfer effects and the inertia of the throat gas including refresh stage. Unfortunately, the fluxes they derived was too simplified [27]. By using developed model, they investigated the behavior of the actuator in a repetitive working condition. One of the researcher once was in Air Force Engineering University conducted a number of studies in Delft University of Technology in the Netherlands with others. Measurements using Schlieren image and PIV methods were conducted to found out effects of geometric features, and energy deposition of a SparkJet in a quiescent air and subsonic flow environments [12, 28-30]. They concluded that shock waves, jet flow, and vortex structures are dependent on orifice diameter. The actuator affected velocity profile, yet short – lived and locally confined. They evaluated a SparkJet actuator that it has enough flow control authority, yet to study further for practical usages.

1.3 Objectives and Scope of the Dissertation

Reviews of previous researches addressed in the earlier sections tell the potentials of a SparkJet actuator as a promising flow control device even for the supersonic flow regime which was difficult for conventional flow control devices. As mentioned earlier, however, the most of the studies were focused on the limited fields of areas; possible uses of the actuator, methods to analyze the actuator, and the other similar contents. Detailed physical flow characteristics of SparkJet actuator's jet and cavity flows are not fully understood yet. Understanding these aspects are essential to utilize SparkJet actuator for certain situations. Moreover, the quantitative analyses regarding the performance factors have not done yet, which are prerequisites for the design and constructions for the practical usage. Consequently, this study tries to solve those limitations of the previous researches and provide detailed physics of a SparkJet actuator which would contribute to the design of the actuator for the practical usage.

The first objective is to understand detailed physics of SparkJet actuator qualitatively and quantitatively by computational analyses. To reflect the physical properties of equilibrium plasma used in SparkJet actuator, local thermodynamic equilibrium is assumed. The investigations include general jet flow characteristics, performance characteristics, and frequency characteristics. For the performance characteristics, thrust and total impulse analyses are conducted. For the frequency characteristics, a Fast Fourier transformation is applied.

The second objective is to verify the origins of frequency characteristics of SparkJet actuator. When the actuator is utilized on the practical flow control, the actuator frequency affects its control authority. The current frequency characteristics

analyses contribute to the fundamentals of it.

The third objective is to correlated some of design variables with performance factors. To do this, numerical parametric studies are conducted. This would contribute to the determination of design variables for the enhancement of performance for SparkJet actuator.

To this ends, this paper is organized in the following orders: Followed by Introduction in Chapter 1, physical models are described in Chapter 2. Here, governing equation, gas dynamic model, and plasma energy deposition model are introduced. Numerical methods are described in the following Chapter 3. Some validation cases for SparkJet actuators are presented to ensure the physical models and numerical methods.

In Chapter 4, fundamental analyses of baseline model are carried out. Such analyses include jet flow characteristics, performance characteristics, and frequency characteristics. A Fast Fourier transformation (FFT) of thrust is conducted for the frequency characteristics analysis.

In Chapter 5, analyses on the origins of frequencies for SparkJet actuator are conducted. Some of design variables are changed to find out the source of the primary frequencies. Also, effects of the oscillations aroused from periodical behavior appeared through frequencies are investigated.

In Chapter 6, analyses on the effects of some of design variables are conducted throughout numerical parametric studies. Performance factors such as thrust and total impulse according to the design variable changes are investigated. Flow inside the cavity are investigated to find out causes of the performance factors changes.

Lastly, conclusions of this dissertation are addressed in the Chapter 7. Summary, contribution and future works are included.

Chapter 2. Physical Model

2.1 Governing Equation

To describe fluid motions of a SparkJet actuator, the unsteady three – dimensional equilibrium Navier – Stokes equation is solved [31-40]. Since a SparkJet actuator is operated by using plasma, an additional source term is employed in the energy balance equation. The system of governing equations in the conservation vector form is written as follows.

$$\frac{\partial Q}{\partial t} + \frac{\partial E}{\partial x} + \frac{\partial F}{\partial y} + \frac{\partial G}{\partial z} = \frac{\partial E_v}{\partial x} + \frac{\partial F_v}{\partial y} + \frac{\partial G_v}{\partial z} + S \quad (2.1)$$

The conservative vector, convective flux vectors, viscos flux vectors, and source term are expressed as follows.

$$Q = \begin{bmatrix} \rho \\ \rho u \\ \rho v \\ \rho w \\ \rho e_t \end{bmatrix}$$
$$E = \begin{bmatrix} \rho u \\ \rho u^2 + p \\ \rho uv \\ \rho uw \\ (\rho e_t + p)u \end{bmatrix}$$

$$F = \begin{bmatrix} \rho v \\ \rho uv \\ \rho v^2 + p \\ \rho vw \\ (\rho e_t + p)v \end{bmatrix}$$

$$G = \begin{bmatrix} \rho w \\ \rho uw \\ \rho vw \\ \rho w^2 + p \\ (\rho e_t + p)w \end{bmatrix}$$

$$E_v = \begin{bmatrix} 0 \\ \tau_{xx} \\ \tau_{xy} \\ \tau_{xz} \\ -q_x + \tau_{xx}u + \tau_{xy}v + \tau_{xz}w \end{bmatrix}$$

$$F_v = \begin{bmatrix} 0 \\ \tau_{yx} \\ \tau_{yy} \\ \tau_{yz} \\ -q_y + \tau_{yx}u + \tau_{yy}v + \tau_{yz}w \end{bmatrix}$$

$$G_v = \begin{bmatrix} 0 \\ \tau_{zx} \\ \tau_{zy} \\ \tau_{zz} \\ -q_z + \tau_{zx}u + \tau_{zy}v + \tau_{zz}w \end{bmatrix}$$

$$S = \begin{bmatrix} 0 \\ 0 \\ 0 \\ 0 \\ S_{plasma} \end{bmatrix}$$

Where, e_t is the total energy which is expressed as $e_t = e_{internal} + e_{hof} + h_{kinetic}$. Each one of energy refers to the internal energy, heat of formation energy, and kinetic energy, respectively. The internal and heat of formation energy are calculated under the equilibrium assumption. Also, q_x , q_y , and q_z are the heat conduction rate in x , y , and z directions, respectively. These terms are calculated

by using the Fourier's Law which are given as follows.

$$q_x = -\kappa \frac{\partial T}{\partial x}, \quad q_y = -\kappa \frac{\partial T}{\partial y}, \quad q_z = -\kappa \frac{\partial T}{\partial z}$$

The terms τ_{ij} are viscous shear stress tensors which are expressed as follows by using Stokes' hypothesis.

$$\tau_{xx} = 2\mu \frac{\partial u}{\partial x} - \frac{2}{3}\mu \left(\frac{\partial u}{\partial x} + \frac{\partial v}{\partial y} + \frac{\partial w}{\partial z} \right)$$

$$\tau_{yy} = 2\mu \frac{\partial v}{\partial y} - \frac{2}{3}\mu \left(\frac{\partial u}{\partial x} + \frac{\partial v}{\partial y} + \frac{\partial w}{\partial z} \right)$$

$$\tau_{zz} = 2\mu \frac{\partial w}{\partial z} - \frac{2}{3}\mu \left(\frac{\partial u}{\partial x} + \frac{\partial v}{\partial y} + \frac{\partial w}{\partial z} \right)$$

$$\tau_{xy} = \tau_{yx} = \left(\frac{\partial u}{\partial y} + \frac{\partial v}{\partial x} \right)$$

$$\tau_{xz} = \tau_{zx} = \left(\frac{\partial u}{\partial z} + \frac{\partial w}{\partial x} \right)$$

$$\tau_{yz} = \tau_{zy} = \left(\frac{\partial v}{\partial z} + \frac{\partial w}{\partial y} \right)$$

The term S_{plasma} in the source term vector S in Equation (2.1) is the energy deposition made by plasma. By this term, describing a SparkJet actuator is available.

To close the system of equations, the equation of state is necessary for pressure calculation. Since the plasma is considered as equilibrium, data on the equilibrium air are used instead of the equation of state. Further explanations are addressed in Section 2.3, which deals with gas dynamic model adapted in this study.

2.2 Non – dimensionalization of Governing Equation

In order to avoid numerical errors from differences of order of magnitude between the variables, the governing equation is non – dimensionalized by following variables. Here, superscript * refers to non – dimensionalized value and subscript ∞ refers to freestream value.

$$t^* = \frac{t}{L_\infty/c_\infty}, \quad x^* = \frac{x}{L_\infty}, \quad y^* = \frac{y}{L_\infty}, \quad z^* = \frac{z}{L_\infty}$$

$$\rho^* = \frac{\rho}{\rho_\infty}, \quad p^* = \frac{p}{\rho_\infty c_\infty^2}, \quad T^* = \frac{T}{T_\infty}, \quad e^* = \frac{e}{c_\infty^2}$$

$$u^* = \frac{u}{c_\infty}, \quad v^* = \frac{v}{c_\infty}, \quad w^* = \frac{w}{c_\infty}$$

$$\mu^* = \frac{\mu}{\mu_\infty}, \quad \kappa^2 = \frac{\kappa}{\kappa_\infty}$$

$$S_{plasma}^* = \frac{S_{plasma}}{(\rho_\infty c_\infty^3)/L_\infty}$$

Some of dimensionless parameters are defined as follows.

$$Ma_\infty = \frac{V_\infty}{c_\infty}, \quad Re_{a_\infty} = \frac{\rho_\infty c_\infty L_\infty}{\mu_\infty}, \quad Pr_\infty = \frac{c_p \mu_\infty}{\kappa_\infty}$$

Here, the Reynolds number is defined by using the speed of sound instead of freestream velocity. The Mach number and Prandtl number are defined as usual. The system of the governing equations becomes as follows as a result of non – dimensionalization. The superscript * is omitted for convenience.

$$\frac{\partial Q}{\partial t} + \frac{\partial E}{\partial x} + \frac{\partial F}{\partial y} + \frac{\partial G}{\partial z} = \frac{\partial E_v}{\partial x} + \frac{\partial F_v}{\partial y} + \frac{\partial G_v}{\partial z} + S \quad (2.2)$$

$$Q = \begin{bmatrix} \rho \\ \rho u \\ \rho v \\ \rho w \\ \rho e_t \end{bmatrix}$$

$$E = \begin{bmatrix} \rho u \\ \rho u^2 + p \\ \rho uv \\ \rho uw \\ (\rho e_t + p)u \end{bmatrix}$$

$$F = \begin{bmatrix} \rho v \\ \rho uv \\ \rho v^2 + p \\ \rho vw \\ (\rho e_t + p)v \end{bmatrix}$$

$$G = \begin{bmatrix} \rho w \\ \rho uw \\ \rho vw \\ \rho w^2 + p \\ (\rho e_t + p)w \end{bmatrix}$$

$$E_v = \begin{bmatrix} 0 \\ \frac{1}{Re_{a_\infty}} \tau_{xx} \\ \frac{1}{Re_{a_\infty}} \tau_{xy} \\ \frac{1}{Re_{a_\infty}} \tau_{xz} \\ -\frac{1}{Re_{a_\infty}} \frac{1}{Pr_\infty(\gamma_\infty - 1)} q_x + \frac{1}{Re_{a_\infty}} (\tau_{xx}u + \tau_{xy}v + \tau_{xz}w) \end{bmatrix}$$

$$F_v = \begin{bmatrix} 0 \\ \frac{1}{Re_{a_\infty}} \tau_{yx} \\ \frac{1}{Re_{a_\infty}} \tau_{yy} \\ \frac{1}{Re_{a_\infty}} \tau_{yz} \\ -\frac{1}{Re_{a_\infty}} \frac{1}{Pr_\infty (\gamma_\infty - 1)} q_y + \frac{1}{Re_{a_\infty}} (\tau_{yx} u + \tau_{yy} v + \tau_{yz} w) \end{bmatrix}$$

$$G_v = \begin{bmatrix} 0 \\ \frac{1}{Re_{a_\infty}} \tau_{zx} \\ \frac{1}{Re_{a_\infty}} \tau_{zy} \\ \frac{1}{Re_{a_\infty}} \tau_{zz} \\ -\frac{1}{Re_{a_\infty}} \frac{1}{Pr_\infty (\gamma_\infty - 1)} q_z + \frac{1}{Re_{a_\infty}} (\tau_{zx} u + \tau_{zy} v + \tau_{zz} w) \end{bmatrix}$$

$$S = \begin{bmatrix} 0 \\ 0 \\ 0 \\ 0 \\ \frac{S_{plasma}}{(\rho_\infty c_\infty^3)/L_\infty} \end{bmatrix}$$

2.3 Gas Dynamic Model

2.3.1 Characteristics of Plasma

In general, plasma is known as the fourth state of matter [41-45]. When the energy of gas is increased and become greater than a certain value, ionization of neutral gas particle occurs and the gas molecule departs into ions and electrons. Many other kinds of chemical reaction take places inside the plasma including ionization, recombination, dissociation, and etc. Thus, plasma consist of neutral molecule, neutral atom, positive/negative ions, and electrons. Due to the mixture of charged particles, plasma has many interesting and complicated properties. There are two possible ways to provide energy for generating plasma; heating and applying electromagnetic field.

Plasma is usually classified into two by its temperature which affects its ionization level; equilibrium plasma and nonequilibrium plasma. Temperature here does not always mean the thermodynamic temperature, but kinetic energy which is commonly measured in electron volts or kelvin. In many cases, it refers to the electron temperature of plasma. If plasma temperature is high enough, Coulomb – collision dominates in plasma and kinetic energy transfer occurs between the particles. So that the temperatures of electron, ion, and neutral particles become almost the same; that is $T_e \approx T_i \approx T_n$, where each one refers to electron temperature, ion temperature, and neutral particle temperature, respectively. This is called thermal equilibrium plasma, or just thermal plasma or equilibrium plasma in short. Equilibrium plasma is formed in the relatively high pressure environment. Thus, if pressure is not high enough, Coulomb – collision is not dominated in plasma so that the kinetic energy is not transferred frequently between the particles due to

differences in mass. The temperature of ion and neutral particles cannot reach as high as electron temperature. Since ions and neutral particles are so heavy that collision of electrons cannot transfer the energy. This is called nonequilibrium plasma.

For SparkJet actuator, plasma is employed to generate jet flow and pressure wave ejections. The actuator may be applied to aircraft such as airplane, drone, and missile for practical flow control. Most of the aircrafts are flying under the altitude of 16,000 m, except ICBMs, where, pressure environment is usually lower than 5 kPa. In Figure 2.1, pressure and temperature relation of electron and heavy particles, including ions and neutral particles, are shown [46]. It is observed that the two temperatures are not deviated and acts together approximately above 5 kPa. Thus, for the possible usage regimes of SparkJet actuator as a flow control device, plasma can be dealt as an equilibrium plasma. This makes the analyses easier because temperature of the plasma and the air can be considered as the same and share the same thermodynamic properties and transport coefficients so that the plasma and the air can be treated as one fluid. Studies of other researcher also approached in this

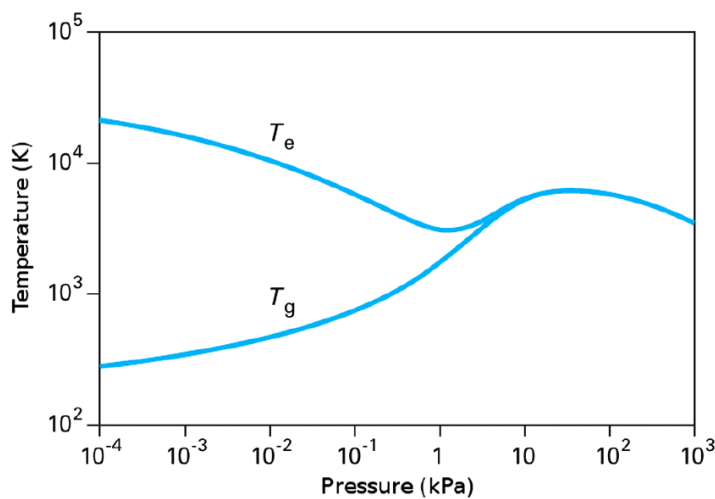


Figure 2.1 Pressure and temperature relation for electron and heavy particles [45].

way and referred as the “real gas” approach [22]. In this study, equilibrium thermodynamic properties and transport coefficients provided by NASA are used. Further descriptions regarding the equilibrium states are addressed in Sec. 2.3.2.

2.3.2 Chemical Equilibrium with Application (CEA)

For the several decades of research for space program, NASA has investigated thermodynamic properties and transport coefficients for the flow of high temperature and pressure which include the plasma state. The Chemical Equilibrium with Application (CEA) database is one of them and provided in the name of NASA Reference 1311 [47, 48]. The CEA provide property data for more than 2,000 chemical species including commonly used air and combustions gas mixtures. In this study, data for general air provided by the CEA is used to calculate thermodynamic properties and transport coefficient. Instead of using the existing calculating program, the equilibrium properties were tabulated in advance to reduce computational time cost. The minimization – of – free – energy calculation method is utilized in the CEA. Since the CEA database valid for temperature higher than 150 K, the calorically perfect gas assumption is used for below 150 K. In this range, the equation of state $p = \rho(\gamma - 1)e_{internal}$ is used for the pressure calculation. Also, Sutherland’s law is used to calculate viscosity and thermal conductivity.

2.3.2.1 Minimization – of – Free – Energy Method

The free energy minimization method utilized in the CEA to calculate the equilibrium state property is the another name of the 2nd law of thermodynamic.

$$\oint \frac{\partial Q}{T} \leq 0 \quad (2.3)$$

Above inequality is called the Clasius theorem. The equality holds for reversible process and the inequality holds for irreversible processes. The integrand function $\frac{\partial Q}{T}$ is the entropy ds . The entropy can be written as follows.

$$ds = \frac{\partial Q_{rev}}{T} + ds_{irr} = ds_{rev} + ds_{irr} \geq 0 \quad (ds_{irr} \geq 0) \quad (2.4)$$

The subscripts *rev* and *irr* refers to reversible and irreversible, respectively. The entropy always increases in a closed system. The Gibbs free energy and the Helmholtz free energy are expressed as follows by using entropy.

$$G \equiv E - Ts + pV \quad (2.5)$$

$$dG = dE - Tds + pdV$$

$$dG = \delta Q - pdV - Tds + pdV$$

$$dG = Tds_{rev} - Tds = -Tds_{irr} \leq 0 \quad (2.6)$$

$$F = E - Ts \quad (2.7)$$

$$dF = dE - Tds$$

$$dF = \delta Q - Tds$$

$$dF = Tde_{rev} - Tds = -Tds_{irr} \leq 0 \quad (2.8)$$

Equation (2.5) and (2.6) holds in constant temperature and pressure. Equation (2.7) and (2.8) holds for constant temperature and volume(density). Since entropy increases in the processes of chemical reactions, the free energies are always less than 0 as stated in Equation (2.6) and (2.8). The stop of entropy increases means that the free energies reach the minimum value. The CEA uses these Gibbs free energy and Helmholtz free energy minimization methods to calculate the equilibrium chemical composition at a given condition.

The Gibbs free energy per kilogram of mixture g for a mixture of the number of species (NS) is given by

$$g = \sum_{j=1}^{NS} \mu_j n_j \quad (2.9)$$

Here, n_j is the number of kilogram – moles of species j . The chemical potential per kilogram – mole μ_j of species j is defined as

$$\mu_j = \left(\frac{\partial g}{\partial n_j} \right)_{T,P,n_{i \neq j}} \quad (2.10)$$

For the minimization of free energy for chemical equilibrium, it is subject to a certain constraint. Following mass – balance constraints are one of such.

$$\sum_{j=1}^{NS} a_{ij} n_j - b_i^0 = b_i - b_i^0 = 0, \quad (i = 1, \dots, l) \quad (2.11)$$

Here, α_{ij} is the number of kilogram – atoms of element i per kilogram – mole of specie j and b_i is the number of kilogram – atoms of element i per kilogram of mixture.

Let us define a term G , that is

$$G = g + \sum_{i=1}^l \lambda_i (b_i - b_i^0) \quad (2.12)$$

Where λ_i are Lagrangian multipliers. For the condition of equilibrium, G becomes,

$$\delta G = \sum_{j=1}^{NS} \left(\mu_j + \sum_{i=1}^l \lambda_i a_{ij} \right) \delta n_j + \sum_{i=1}^l (b_i - b_i^0) \delta \lambda_i = 0 \quad (2.13)$$

By treating the terms δn_j and $\delta \lambda_i$ as independent,

$$\mu_j + \sum_{i=1}^l \lambda_i a_{ij} = 0, \quad (j = 1, \dots, NS) \quad (2.14)$$

and also gives the mass – balance equation, which is Equation (2.11).

The chemical potential can be written as follows.

$$\mu = \begin{cases} \mu_j^0 + RT \ln \frac{n_j}{n} + RT \ln P & (j = 1, \dots, NG) \\ \mu_j^0 & (j = NG + 1, \dots, NS) \end{cases} \quad (2.15)$$

Where μ_j^0 for gases ($j = 1, \dots, NG$) and for condensed phases ($j > NG$) are the chemical potential in the standard state.

Equation (2.11) and (2.14) permit the determination of equilibrium compositions for thermodynamic states specified by assigned temperature T_0 and pressure P_0 .

Instead of the Gibbs free energy, Helmholtz free energy can be used by using the following relations.

$$f = g - PV \quad (2.16)$$

Here, f is the Helmholtz free energy per kilogram of mixture. By substituting Equation (2.9), Equation (2.16) becomes

$$f = \sum_{j=1}^{NS} \mu_j n_j - PV \quad (2.17)$$

The chemical potential per kilogram – mole μ_j of species j is defined as

$$\mu_j = \left(\frac{\partial f}{\partial n_j} \right)_{T, P, n_{i \neq j}} \quad (2.18)$$

The Helmholtz free energy in the condition of equilibrium and subject to mass – balance equation are as follows.

$$F = f + \sum_{i=1}^l \lambda_i (b_i - b_i^0) \quad (2.19)$$

$$\delta F = \sum_{j=1}^{NS} \left(\mu_j + \sum_{i=1}^l \lambda_i a_{ij} \right) \delta n_j + \sum_{i=1}^l (b_i - b_i^0) \delta \lambda_i = 0 \quad (2.20)$$

The chemical potential can be written as,

$$\mu = \begin{cases} \mu_j^0 + RT \ln \frac{n_j R' T}{V} & (j = 1, \dots, NG) \\ \mu_j^0 & (j = NG + 1, \dots, NS) \end{cases} \quad (2.21)$$

Here, $R' = R \times 10^{-5}$.

While the equilibrium thermodynamic states are specified by assigned temperature and pressure for Gibbs free energy, assigned temperature T_0 and volume V_0 (density ρ_0) specify the states for Helmholtz free energy. In either way, equations are not linear and therefore an iterative calculation is required to obtain the equilibrium composition. Thus, in the CEA, Newton – Raphson method is used to solve the equations. For the detailed explanations, refer to NASA reference 1311 [47, 48]

2.3.2.2 Thermodynamic Properties of CEA

As a result of minimization – of – free – energy, chemical composition at equilibrium state is obtained. By using the compositions, thermodynamic properties of flow are calculated. Specifically, density and enthalpy are calculated by following

equations.

$$\rho = \frac{p}{RT} \frac{\sum_{j=1}^{NS} n_j M_j}{\sum_{j=1}^{NS} n_j} \quad (2.22)$$

$$h = \frac{\sum_{j=1}^{NS} n_j H_j^0}{\sum_{j=1}^{NS} n_j} \quad (2.23)$$

Here, M_j is the molecular weight of species j . H_j^0 is the standard – state molar enthalpy of species j .

The specific heat at constant pressure is expressed in the form of combination of frozen and reaction contributions.

$$c_{p,eq} = c_{p,fr} + c_{p,re} \quad (2.24)$$

The contributions to specific heat of frozen and reaction are calculated by following manners.

$$c_{p,fr} = \frac{\sum_{i=1}^{NM} x_i C_i^0}{\sum_{i=1}^{NM} x_i M_i} \quad (2.25)$$

$$c_{p,re} = \frac{R \sum_{i=1}^{NR} \frac{\Delta_r H_r^0}{RT} X_i}{\sum_{i=1}^{NM} x_i M_i} \quad (2.26)$$

Here, NR and NM indicate the total number of chemical reactions of gaseous species and the number of gaseous species for the calculations, respectively. C_i^0 is the standard – state molar specific heat of species i . The term $\Delta_r H_r^0$ is calculated

by following equations.

$$\Delta_r H_r^0 = \sum_{k=1}^{NM} \alpha_{ik} H_k^0 \quad (2.27)$$

$$\sum_{k=1}^{NM} \alpha_{ik} A_k = 0 \quad (i = 1, 2, \dots, NR)$$

Here, α_{ik} are the stoichiometric coefficient for chemical reactions involving species A_k .

The term X_i is calculated by following equations.

$$\sum_{j=1}^{NR} d_{ij} X_i = \frac{\Delta_r H_r^0}{RT} \quad (i = 1, 2, \dots, NR) \quad (2.28)$$

$$d_{ij} = \sum_{k=1}^{NM-1} \sum_{l=k+1}^{NM} x_k x_l \left(\frac{\alpha_{ik}}{x_k} - \frac{\alpha_{il}}{x_l} \right) \left(\frac{\alpha_{jk}}{x_k} - \frac{\alpha_{jl}}{x_l} \right)$$

Here, x_i is the mole fraction of species i relative to the NM gaseous species involved in the calculation.

The standard – state value appeared in Equation (2.23) and (2.26) are given in the form of least – square coefficients.

$$\frac{H^0}{RT} = -a_1 T^{-2} + a_2 \frac{\ln T}{T} + a_3 + a_4 \frac{T}{2} + a_5 \frac{T^2}{3} + a_6 \frac{T^3}{4} + a_7 \frac{T^4}{5} + \frac{a_8}{T} \quad (2.29)$$

$$\frac{C_p^0}{R} = a_1 T^{-2} + a_2 T^{-1} + a_3 + a_4 T + a_5 T^2 + a_6 T^3 + a_7 T^4 \quad (2.30)$$

Each one of coefficients a_i is provide in the CEA database.

2.3.2.3 Transport Coefficients of CEA

In order to calculate viscosity and thermal conductivity of equilibrium state, those of individual species are calculated in advance in CEA. Based on the database in the CEA, those transport coefficients are calculated in the form of least – square coefficients.

$$\left. \begin{matrix} \ln \mu \\ \ln \kappa \end{matrix} \right\} = A \ln T + \frac{B}{T} + \frac{C}{T^2} + D \quad (2.31)$$

Here, μ and κ refer to viscosity and thermal conductivity, respectively. Based on the individual transport coefficients, the equilibrium transport coefficients are calculated as follows.

$$\mu = \sum_{i=1}^{NM} \frac{x_i \mu_i}{x_i + \sum_{j=1}^{NM} x_j \phi_{ij}} \quad (2.32)$$

$$\phi_{ij} = \frac{1}{4} \left[1 + \left(\frac{\mu_i}{\mu_j} \right)^{\frac{1}{2}} \left(\frac{M_j}{M_i} \right)^{\frac{1}{4}} \right]^2 \left(\frac{2M_j}{M_i + M_j} \right)^{\frac{1}{2}}$$

$$\kappa_{eq} = \kappa_{fr} + \kappa_{re} \quad (2.33)$$

$$\kappa_{fr} = \sum_{i=1}^{NM} \frac{x_i \kappa_i}{x_i + \sum_{j=1}^{NM} x_j \psi_{ij}}$$

$$\kappa_{eq} = R \sum_{i=1}^{NR} \frac{\Delta_r H_i^0}{RT} \kappa_{r,i}$$

$$\psi_{ij} = \phi_{ij} \left[1 + \frac{2.41(M_i - M_j)(M_i - 0.142M_j)}{(M_i + M_j)^2} \right]$$

Here, ϕ_{ij} ($\phi_{ij} \neq \phi_{ji}$) is the viscosity interaction coefficient between species i and j , and ψ_{ij} ($\psi_{ij} \neq \psi_{ji}$) is the interaction coefficient between species i and j . The required terms $\kappa_{r,i}$ in the calculation of κ_{eq} are found by solving the following set of linear equations.

$$\sum_{j=1}^{NR} g_{ij} \kappa_{r,j} = \frac{\Delta_r H_i^0(T)}{RT} \quad (i = 1, 2, \dots, NR)$$

$$g_{ij} = \sum_{k=1}^{NM-1} \sum_{l=k+1}^{NM} \left(\frac{RT}{PD_{kl}} x_k x_l \right) \left(\frac{\alpha_{ik}}{x_k} - \frac{\alpha_{il}}{x_l} \right) \left(\frac{\alpha_{jk}}{x_k} - \frac{\alpha_{jl}}{x_l} \right)$$

$$\frac{RT}{PD_{kl}} = \frac{5M_k M_l}{3A_{kl}^* \mu_{kl} (M_k + M_l)}$$

Viscosity and thermal conductivity in equilibrium state calculated by CEA is shown in Figure 2.2 and Figure 2.3, respectively. Also, those transport coefficients calculated by Sutherland's law are plotted together for comparison. The results are similar to each other below 1,000 K. However, they start to show differences above 1,000 K. Since local temperature of cavity may exceed 1,000 K due to the energy deposition, the equilibrium assumption is necessary for SparkJet actuator analysis.

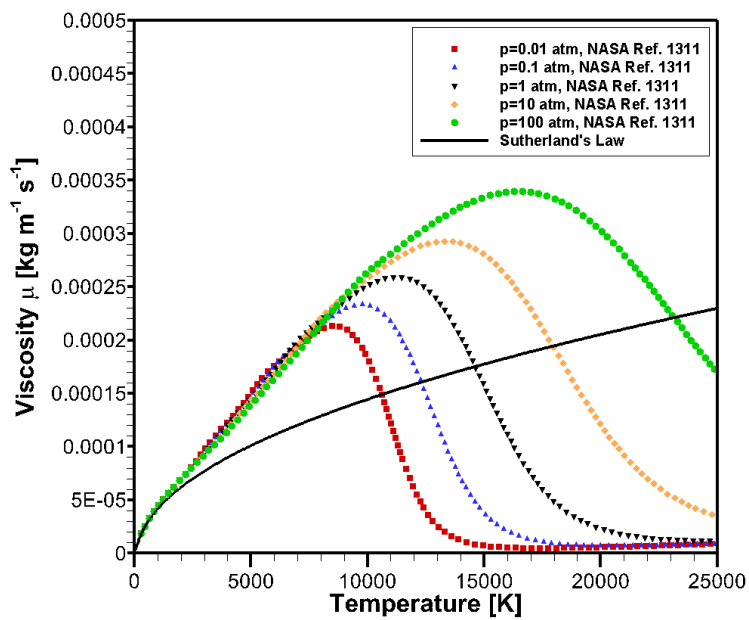


Figure 2.2 Comparison of viscosity calculated by CEA and Sutherland's law.

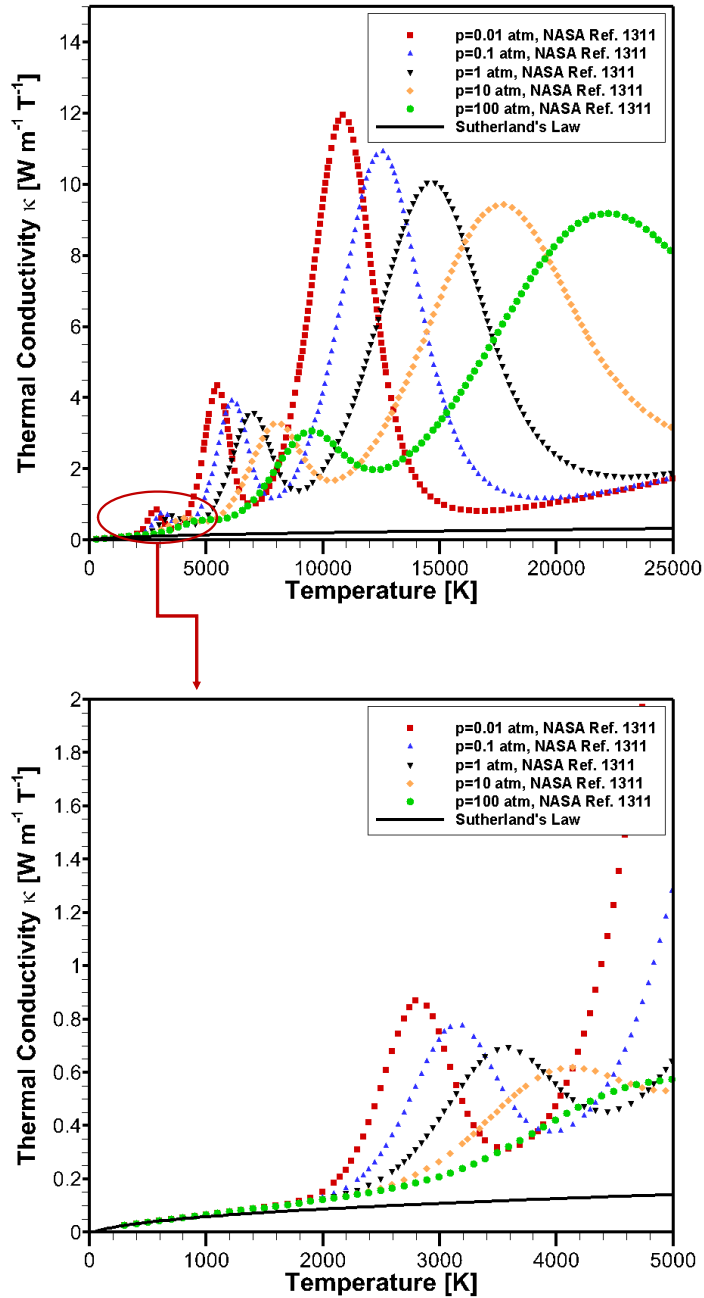


Figure 2.3 Comparison of thermal conductivity calculated by CEA and Sutherland's law.

2.4 Plasma Energy Deposition Model

In order to simulate a SparkJet actuator numerically, energy deposition made by plasma must be included in the governing equation. Plasma energy deposition is represented as a source term S_{plasma} in Equation (2.1). In general, this term can be expressed as $S_{plasma} = S_{joule} - S_{rad} = \eta S_{joule}$, where S_{joule} is the thermal energy generated by the Joule heating process of plasma and S_{rad} is the energy loss through radiation of plasma. Since the radiation energy loss is a function of many variables, energy transfer efficiency η with proper approximation is used to estimate energy deposition amount S_{plasma} in many cases to avoid difficulties in obtaining S_{rad} . By using this factor, it is assumed that only a certain percentage of the Joule heating energy is deposited on to flow and other is lost through the radiation. It is reported that the energy transfer efficiency is approximately a few percent to 30 % [49] depending on the size of the actuator, input power, operating environment, and many others. Since it is relatively easy to obtain energy deposition amount S_{plasma} by adopting the energy transfer efficiency η , there are many studies to determine the factor with proper physical considerations [19, 21, 27, 49]. These leaves only obtaining S_{joule} to calculate S_{plasma} .

Basically, there are three ways to obtain the Joule heating energy S_{plasma} and each one of them requires experimental measurements. The first one is to measure the voltage and current of the plasma – generating circuit which is the most intuitive. By multiplying the measured voltage and current, the power dissipated from plasma is calculated which is stemmed from the Joule heating energy. The second one is to use the measured current and solving Gauss' Law. By solving the equation, it is able to calculate voltage across the plasma [50]. The Joule heating energy is calculated

by the measured current and calculated voltage. The last way is to solve RLC circuit equation with the appropriate values of circuit elements such as resistance, inductance, and capacitance [22]. In this method, adequate assumption and/or measurement are required for the determination of the circuit elements. The solution of the RLC circuit equation gives voltage and current which can be used to calculate the Joule heating energy.

Since such experimental measurements are not available in the current study, the net energy source term S_{plasma} is applied directly as a time – dependent function [23]. The source term function is obtained by curve fitting which is originally obtained and cross checked by the first and the third methods mentioned above in the reference. Thus, the use of the time – dependent function is reasonable to reduce the costs and efforts. In this manner, moreover, the estimation and/or prediction of energy needed for desired performance of a SparkJet is possible. Also, draft design and construction of a plasma – generating circuit is available.

Chapter 3. Numerical Method and Validations

3.1 Numerical Methods

3.1.1 Spatial Discretization

For the spatial discretization of convective flux terms of governing equation, the AUSMPW+ scheme is used [51]. This flux scheme has advantage in controlling and removing oscillations occur in AUSM+, where near wall and strong shock waves, while maintaining the accuracy of the original scheme. The AUSMPW+ scheme controls the advection characteristics of the flow by introducing a pressure – weighting function. Since shock waves are generated by plasma energy deposition when a SparkJet actuator is operated, a flux scheme which has strength in dealing shock waves is used.

The numerical flux of the AUSMPW+ scheme is written as follows.

$$F_{1/2} = \overline{M}_L^+ c_{1/2} \Phi_L + \overline{M}_R^- c_{1/2} \Phi_R + (P_L^+ P_L + P_R^- P_R) \quad (3.1)$$

Here, $\Phi = (\rho, \rho u, \rho H)^T$ and $P = (0, p, 0)^T$. Basically, the numerical flux is divided into convective and pressure terms. The subscript 1/2 and (L,R) represent the cell interface and left and right of the cell interface, respectively. The Mach number at the cell interface is defined by

$$m_{\frac{1}{2}} = M_L^+ + M_R^- \quad (3.2)$$

By using Mach number interpolation function $\overline{M}_{L,R}^{\pm}$ at the left and the right side across the cell interface, the Mach number at the cell interface is defined.

$$\text{i) } m_{\frac{1}{2}} = M_L^+ + M_R^- \geq 0$$

$$\begin{aligned}\overline{M}_L^+ &= M_L^+ + M_R^- \cdot [(1 - w) \cdot (1 + f_R) - f_L] \\ \overline{M}_R^- &= M_R^- \cdot w \cdot (1 + f_R)\end{aligned}\tag{3.3}$$

$$\text{ii) } m_{\frac{1}{2}} < 0$$

$$\begin{aligned}\overline{M}_L^+ &= M_L^+ \cdot w \cdot (1 + f_L) \\ \overline{M}_R^- &= M_R^- + M_L^+ \cdot [(1 - w) \cdot (1 + f_L) - f_R]\end{aligned}\tag{3.4}$$

The functions f and w are the pressure – weighted functions which are given by

$$w(p_L, p_R) = 1 - \min\left(\frac{p_L}{p_R}, \frac{p_R}{p_L}\right)^3\tag{3.5}$$

$$f_{L,R} = \left(\frac{p_{L,R}}{p_s} - 1\right) \times \min\left(1, \frac{\min(p_{1,L}, p_{1,R}, p_{2,L}, p_{2,R})}{\min(p_L, p_R)}\right)^2, p_s \neq 0\tag{3.6}$$

Here, $p_s = P_L^+ p_L + P_R^- p_R$.

The Mach number and pressure of AUSMPW+ across a cell interface are given by

$$M^{\pm} = \begin{cases} \pm \frac{1}{4}(M \pm 1)^2, & |M| \leq 1 \\ \frac{1}{2}(M \pm |M|), & |M| > 1 \end{cases} \quad (3.7)$$

$$P^{\pm} = \begin{cases} \frac{1}{4}(M \pm 1)^2(2 \mp M), & |M| \leq 1 \\ \frac{1}{2}(M \pm \text{sign}(M)), & |M| > 1 \end{cases} \quad (3.8)$$

The Mach number of each side of a cell interface and speed of sound at a cell interface are

$$M_{L,R} = \frac{U_{L,R}}{\frac{c_1}{2}} \quad (3.9)$$

$$c_{\frac{1}{2}} = \min(c_s^{*2} / \max(|U_L|, c_s^*), c_s^{*2} / \max(|U_R|, c_s^*),) \quad (3.10)$$

Here, c_s^* is the critical speed of sound which is given by $\sqrt{\frac{1(\gamma-1)}{(\gamma+1)} H_{normal}}$,

where H_{normal} is the total enthalpy normal to a cell interface expressed as

$$H_{normal} = 0.5(H_L - 0.5V_L^2 + H_R - 0.5V_R^2).$$

To improve spatial accuracy for high resolution, the MUSCL scheme with a minmod limiter is used which is expressed as follows [52].

$$\begin{aligned} \phi(r) &= \max[0, \min(1, r)] \\ \lim_{r \rightarrow \infty} \phi(r) &= 1 \end{aligned} \quad (3.11)$$

For the viscous flux terms, the second order central differencing is used.

3.1.2 Time Integration

Since the changes in the flow field is very localized for a SparkJet actuator in a quiescent air, the Runge – Kutta time integration method is used. When the changes are localized compared to entire computational domain, the changes are hard to propagate properly throughout the domain [53, 54]. Thus, the solution might converge to wrong one when implicit method is used. In this regards, the direct time marching method is used to calculate the unsteady terms.

The discretized system of equations of Navier – Stokes equation is written as ordinary differential equation.

$$\frac{1}{J} \frac{dQ}{dt} = -R(Q) \quad (3.12)$$

$$Q_t = f(Q)$$

The Q represents the vector of flow variables, J represents the jacobian matrix whose inverse is the volume of a computational cell, and $R(Q)$ is the residual vector which consist of convective flux vectors, viscous flux vectors, and source term vector. For a convinience, the solution of n^{th} time step Q_n is expressed as $f(Q)$. Then, the variation of n^{th} and $(n+1)^{\text{th}}$ time step is limited by applying Total Variation Diminishing (TVD) as following manner for the high order accuracy [55].

$$TV(Q^n) = \sum_j |Q_{j+1}^n - Q_j^n| \quad (3.13)$$

$$TV(Q^{n+1}) \leq TV(Q^n)$$

Many kinds of differencing methods exist satisfying the Equation (3.46). In this study, the 3rd order Runge – Kutta methods are used.

$$\begin{aligned}
 Q^{(1)} &= Q^n + \Delta t f(Q^n) \\
 Q^{(2)} &= \frac{3}{4}Q^n + \frac{1}{4}Q^{(1)} + \frac{1}{4}\Delta t f(Q^{(1)}) \\
 Q^{n+1} &= \frac{1}{3}Q^n + \frac{2}{3}Q^{(2)} + \frac{2}{3}\Delta t f(Q^{(2)})
 \end{aligned} \tag{3.14}$$

3.1.3 Initial Conditions and Boundary Conditions

In this study, a SparkJet actuator operated in a quiescent air is analyzed whose environment has no initial flow. The initial conditions are 101,325 Pa for pressure and 300 K for temperature. This pressure and temperature are applied to entire computational domain. The initial density is 1.171 kg/m³ accordingly. This density is maintained for plasma an initial condition which has higher pressure and temperature. The reason for different initial condition for plasma is that the computations are carried out under the assumption that plasma is already formed and is in the equilibrium state. Simulating the formation of plasma needs to consider thermochemical nonequilibrium effects of plasma chemical reactions. Theses requires much more complicated and time consuming computations. Since, in this study, plasma is considered as equilibrium and thus, the plasma formation phase is reflected as plasma initial conditions.

An adiabatic nonslip boundary condition is applied at the wall including cavity. It is arguable that surface temperature affects the temperature inside the cavity, and thus the performance of SparkJet actuator. Because there possibly be heat transfer

across the wall which is a source of energy loss for driving force for the actuator. However, certain temperature distribution inside the cavity is unknown yet. Thus, applying an adiabatic condition of the current study would be a baseline for the further study. Pressure is extrapolated at the outer boundary of the external domain. Finally, in order to reduce computational time cost, symmetry boundary condition is applied on the symmetry wall. The symmetry boundary condition reduces the entire computational domain by 75 %.

3.1.4 Fast Fourier Transformation

To analyze frequency characteristics of a SparkJet actuator, fast Fourier Transformation (FFT) is conducted. By performing the FFT, physical properties in time domain are transformed into frequency domain. The FFT is one way of Discrete Fourier Transformation (DFT) that utilizes better algorithm to perform DFT with reduced number of computations from $2N^2$ to $2N \log_2 N$ [56]. The DFT converts an equally – spaced finite sequence of samples in a function of time into a function of frequency. A sequence of N complex number x_n are transformed into X_k by following definition.

$$\begin{aligned}
 X_k &= \sum_{n=0}^{N-1} x_n \cdot e^{-i2\pi kn/N}, \quad k = 0, \dots, N-1 \\
 x_n &= \frac{1}{N} \sum_{k=0}^{N-1} X_k \cdot e^{i\pi kn/N}
 \end{aligned} \tag{3.15}$$

For the FFT, the sampling number N is broken down into $M = N/2$. Then the equation (3.48) departs into two parts; an odd part and an even part.

$$\begin{aligned}
X_n &= \sum_{n=0}^{N-1} x_n \cdot e^{-i2\pi kn/N} \\
&= \sum_{n=0}^{N/2-1} x_{2n+1} \cdot e^{-i2\pi k(2n+1)/N} + \sum_{n=0}^{N/2-1} x_{2n} \cdot e^{-i2\pi k(2n)/N} \\
&= e^{-i2\pi k/N} \sum_{n=0}^{N/2-1} x_{2n+1} \cdot e^{-i2\pi kn/(N/2)} + \sum_{n=0}^{N/2-1} x_{2n} \cdot e^{-i2\pi kn/(N/2)}
\end{aligned} \tag{3.16}$$

The number of computations of equation (3.48) requires $2N^2$, but equation (3.49) requires $2N \log_2 N$ [57].

Even though a result from an FFT provides insight of a signal, it has limitation that the actual FFT assumes a finite set of data in a cyclical topology. The two endpoints of the data on the time domain are considered to be connected. However, a data set is not an integer number of periods and discontinuities occur in both endpoints. It may be truncated and, in some cases, periods are unknown before they are analyzed. These result in different characteristics from an original data set so that an FFT result does not reflect the accurate frequency spectrum. The result may be smeared or the frequency may be leaked into other frequencies.

A technique called windowing can minimize these phenomena [58]. Windowing reduces discontinuities at the both boundaries of a data set. Windowing is performed by multiplying a pre – designed function in time domain that smoothly and gradually reduces the edge of a data set. Many kinds of window functions exist for different types of data. Window function should be selected depending on the

characteristics of a data set. In general, Hanning window function satisfies most of the cases and gives good frequency resolution with reduced signal leakage. Since, the original frequency characteristics of data set for a FFT in this study is unknown, Hanning window function is applied when performing a FFT. The function is given by as follows [59].

$$w_0(x) = \begin{cases} \frac{1}{2} \left(a + \cos\left(\frac{2\pi x}{L}\right) \right) = \cos^2\left(\frac{\pi x}{L}\right), & |x| \leq L/2 \\ 0, & |x| \geq L/2 \end{cases} \quad (17)$$

3.2 Validations

For numerical analysis of SparkJet actuator in the current study, developed in-house code is used [60, 61]. The code considered all of the physical models and numerical methods mentioned earlier. In this section, the used equilibrium flow analysis solver is validated for the use of analyzing SparkJet actuator. However, precise measurements of any flow properties such as pressure, temperature and velocity are hardly available to compare because SparkJet actuator is so small. Especially, it is more difficult to measure flow state inside the cavity, which affects the performance of SparkJet actuator. Because not only it is so small to install any measuring instruments, but also such things may influence the actuator. Thus, only macroscopic comparing and validating is possible for numerically analyzed SparkJet actuator with experimental data. In many cases, time history of jet front positions from Schlieren images and computation results are compared to validate the numerical analyses as shown in Figure 3.1. Thus, in this study, two cases of SparkJet actuators from references are numerically analyzed and compared by this manner for the validation of the equilibrium flow solver.

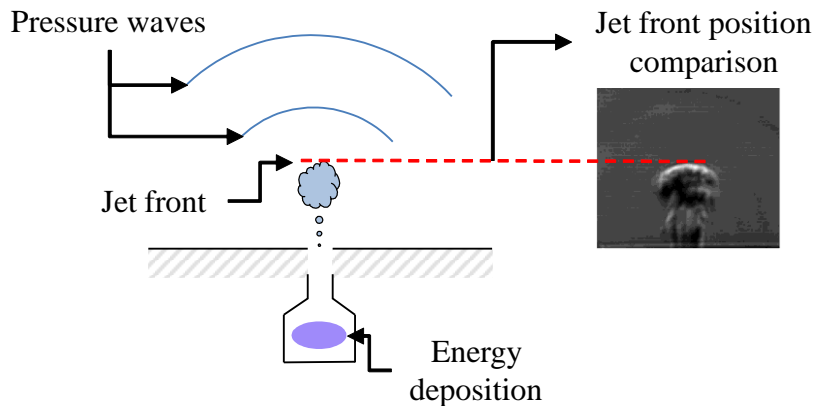


Figure 3.1 Example of jet front position comparison.

3.2.1 ONERA Case

To validate the usage of equilibrium flow solver in SparkJet actuator analysis, experimental measurement and numerical simulation results provided by ONERA are compared [23]. In the reference, the SparkJet actuator has cylindrical shape with a taper angle forming converging section. It has 4.6 mm of cavity diameter and 4.0 mm of cavity height, which make the cavity volume 66.47 mm³. On the top of the cavity, there is a converging section with 45° taper angle, and then orifice. The orifice throat length is 1 mm and orifice diameter is 1 mm, respectively. A pair of electrodes with 1 mm of diameter is placed inside the cavity and departed by 1.2 mm. Also the pair is 2.0 mm from the bottom of the cavity. The region between the electrodes which is formed by the electrode gap and diameter is energy deposition area. In Table 3.1 and Figure 3.2, configurations used in the validation is shown.

Table 3.1 Design variables of ONERA case.

| Design variables | Value |
|----------------------------|-------|
| Orifice exit diameter (mm) | 1.0 |
| Orifice throat length (mm) | 1.0 |
| Orifice taper angle (°) | 45 |
| Cavity diameter (mm) | 4.6 |
| Cavity height (mm) | 4.0 |
| Electrode height (mm) | 2.0 |
| Electrode gap (mm) | 1.2 |
| Electrode diameter (mm) | 1.0 |

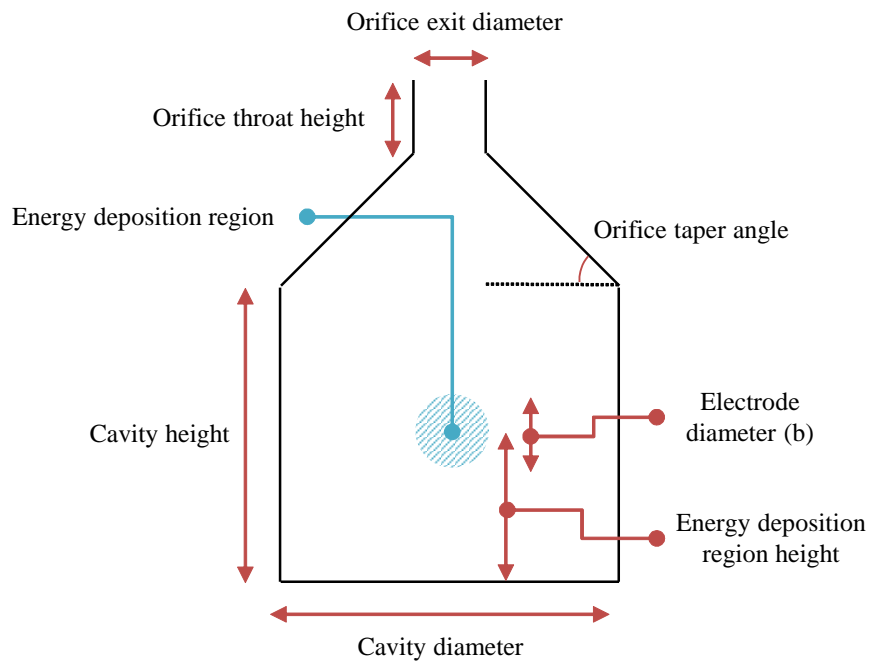
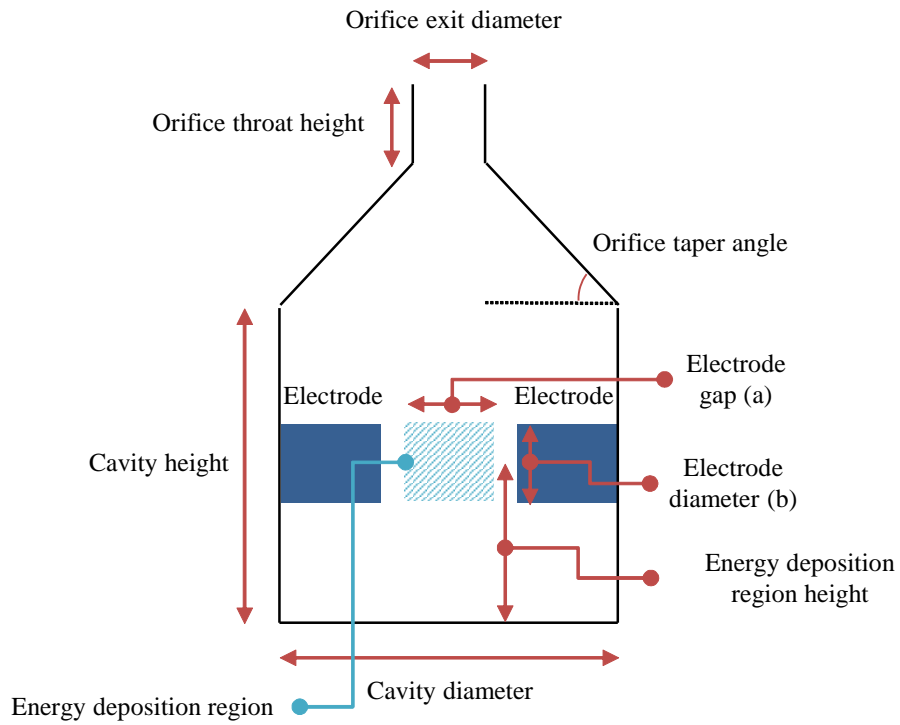


Figure 3.2 Configuration of a SparkJet actuator.

The grid for the computation is generated by using structured grid system as shown in Figure 3.3. The electrodes are omitted since it is very difficult to embody them in the structured grid system. There might be an argue that existence of electrode affects the jet flow. However, it is mentioned in the reference that the formation and the symmetry of the ejected jet is not influenced by the presence of the electrodes.

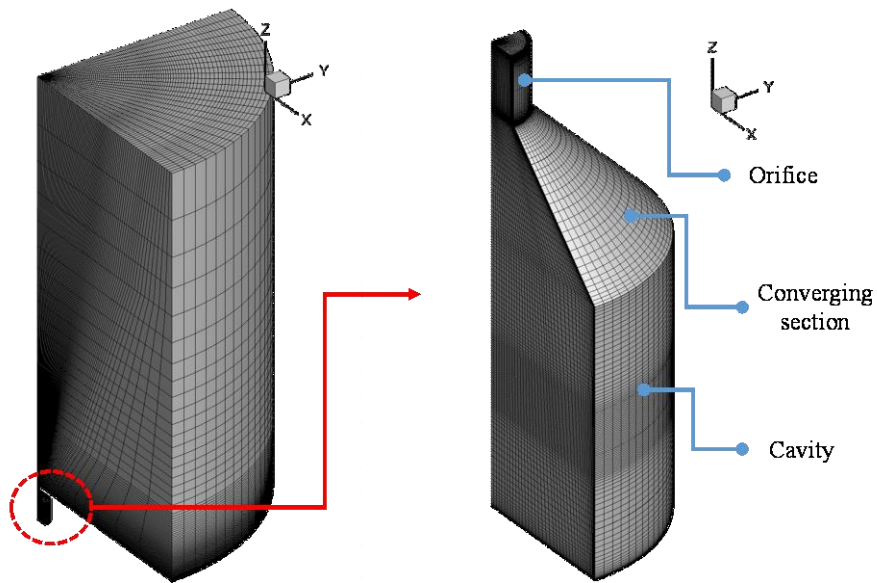


Figure 3.3 Computational domain and the grid system.

This actuator was operated in the quiescent atmospheric pressure and room temperature condition. Voltage across the capacitor and current of the discharge is shown in Figure 3.4 which is provided in the reference [62]. The voltage is not measured for the plasma. It is measured for capacitor so that it is different from the applied voltage to generate plasma. Such applied voltage is not mentioned specifically. Rather, the deposited energy is mentioned as 3 mJ in 10 μ s, which is cross checked by experiment and calculation. Thus, those energy is directly

deposited as shown in Figure 3.5 which is provided in the reference [23]. The related experimental works and calculations are explained in detailed in several references [21-23, 62]. This energy deposition corresponds to 3.5 % of energy transfer efficiency η according to the reference [23]. In the reference, the amount of energy deposition made by plasma was calculated by the third method mentioned in the earlier Sec.2.4. In this study, time history of energy deposition provided in the reference is used as a source term, which is shown in Figure 3.5.

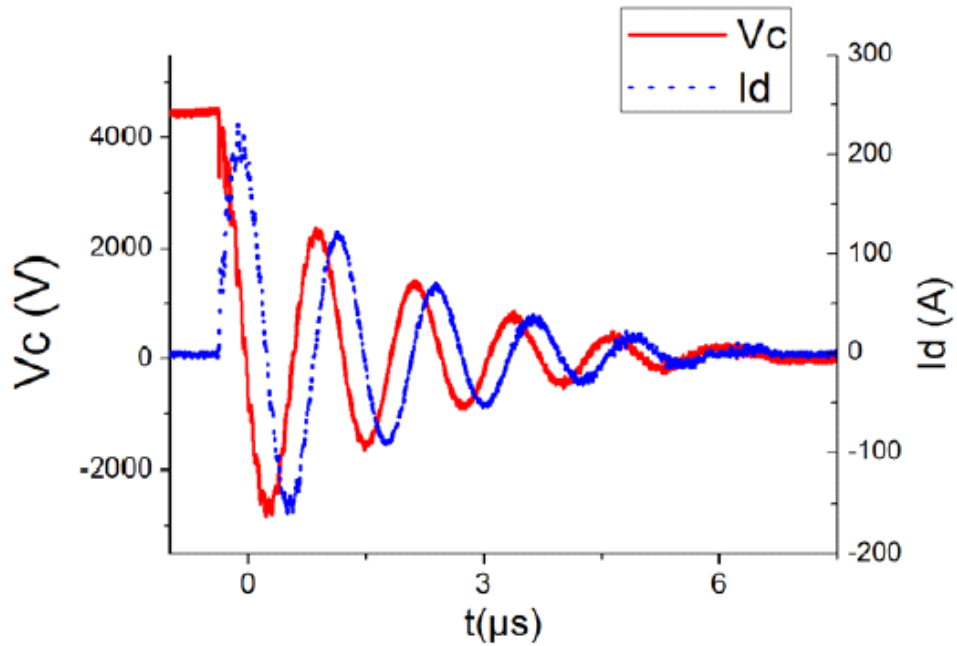


Figure 3.4 Voltage across the capacitor and current of the discharge [62].

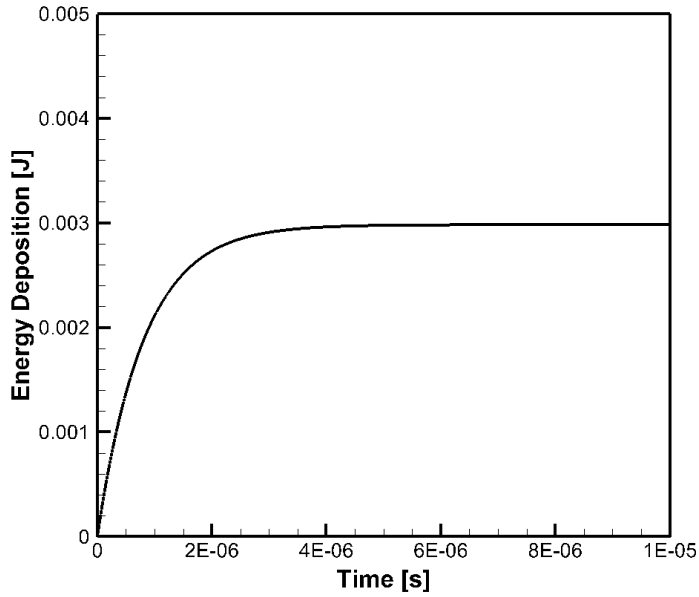


Figure 3.5 Time history of energy deposition applied as a source term. ONERA case.

The calculated results of density and pressure fields are shown in Figure 3.6. In order to check the validity of the equilibrium flow solver used in the current study, jet front positions with respect to time are compared with the data provided in the reference as shown in Figure 3.7. As it can be seen from the figure that the results of the current study are within the error bars from the experiment of the reference. Moreover, the CFD results of the current study is more accurate than those of the reference, especially before $40 \mu\text{s}$. Consequently, it is confirmed that it is reasonable to use the in – house code to analyze the SparkJet actuator.

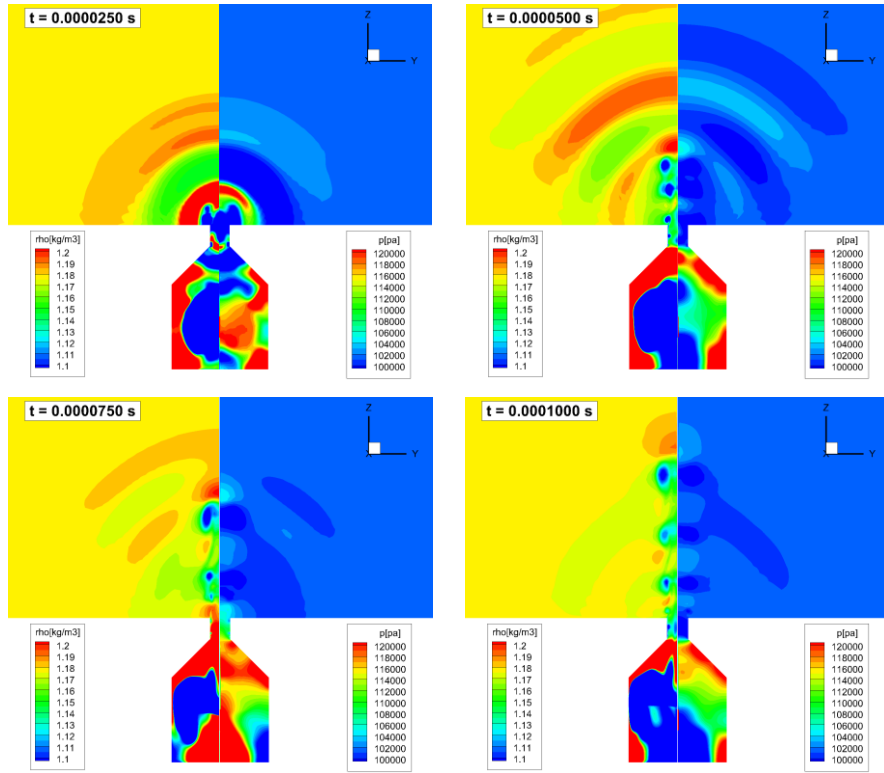


Figure 3.6 Density and pressure fields of SparkJet actuator:

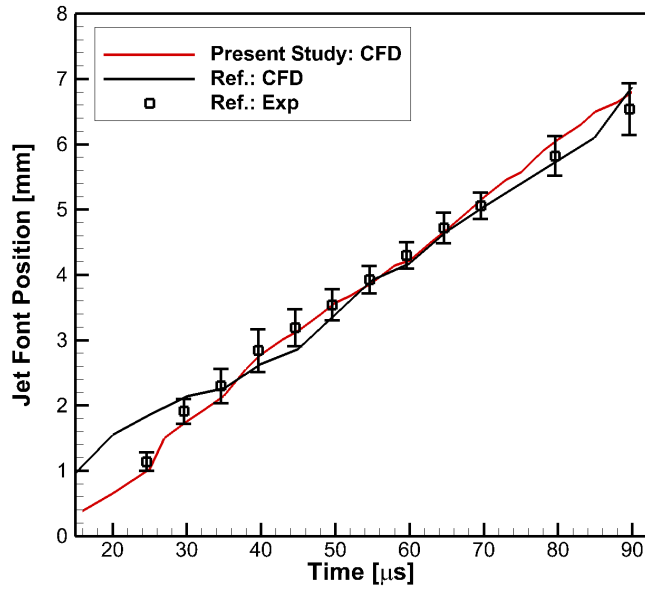


Figure 3.7 Comparison of jet front positions for validation. ONERNA case [22].

3.2.2 Ulsan University Case

The second validation is conducted for the use of the equilibrium flow solver in SparkJet actuator analysis. The second case is the experiment conducted by research team at Ulsan University. Related data and results were personally provided and confirmed by professor Jichul Shin at Ulsan University who lead the team and supervised the corresponding experiments and some others [63, 64]. Basically, the geometry of the SparkJet actuator that they used were similar to that of ONERA's. However, detailed values of design variables are different as shown in Table 3.2. The SparkJet actuator of Ulsan University has smaller cavity volume compared to ONERA's. Also, the electrode pair is much closer to the orifice and its gap are the same as cavity diameter. Since the electrodes are not intruded into the cavity, the grid system regarding the electrodes has no arguments on their emittance. The grid systems and boundary conditions are also constructed alike.

Table 3.2 Design variables of Ulsan University case.

| Design variables | Value |
|----------------------------|-------|
| Orifice exit diameter (mm) | 1.0 |
| Orifice throat length (mm) | 1.0 |
| Orifice taper angle (°) | 45 |
| Cavity diameter (mm) | 3.0 |
| Cavity height (mm) | 3.0 |
| Electrode height (mm) | 2.0 |
| Electrode gap (mm) | 3.0 |
| Electrode diameter (mm) | 2.0 |

This actuator was operated at the quiescent air with room temperature and 0.1 atm pressure condition. The applied voltage is approximately 2.5 kV and the applied current is approximately 2.5 A as shown in Figure 3.8. The Joule heating energy calculated by measured time – varying voltage and current is approximately 53 mJ during 9 μ s as shown in Figure 3.9. This energy was lineally increased from the generation of plasma, and applied as a source term with energy transfer efficiency of 1.9 %. Some trial and error is needed on the estimation of the energy transfer efficiency. Since the cavity volume is smaller than that of ONERA's, it is reasonable that Ulsan University case has lower energy transfer efficiency.

In order to check the validity of the equilibrium flow solver used in the current study, jet front positions with respect to time are compared with the personally provided data. Originally, the data were a set of Schlieren images with 10 μ s intervals. The jet front positions at each interval are extracted from the images. Figure 3.10 shows the time history of jet front positions, and it shows that the experimental data and the CFD results are well matched. Figure 3.11 shows the provided Schlieren images and calculated density field of the flow. As it can be seen from the figure that the jet fronts at each interval are aligned closely. Consequently, it is again confirmed that it is reasonable to use the in – house code to analyze the SparkJet actuator.

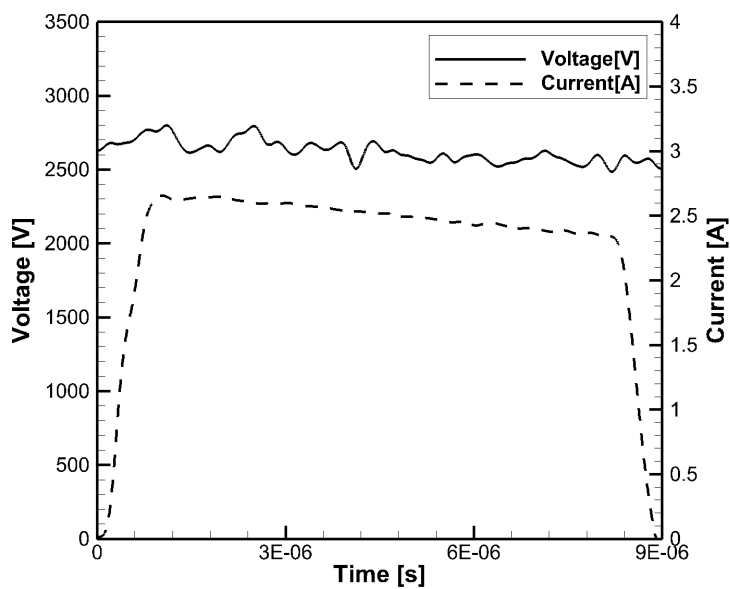


Figure 3.8 Time history of applied voltage and current. Ulsan Univ. case.

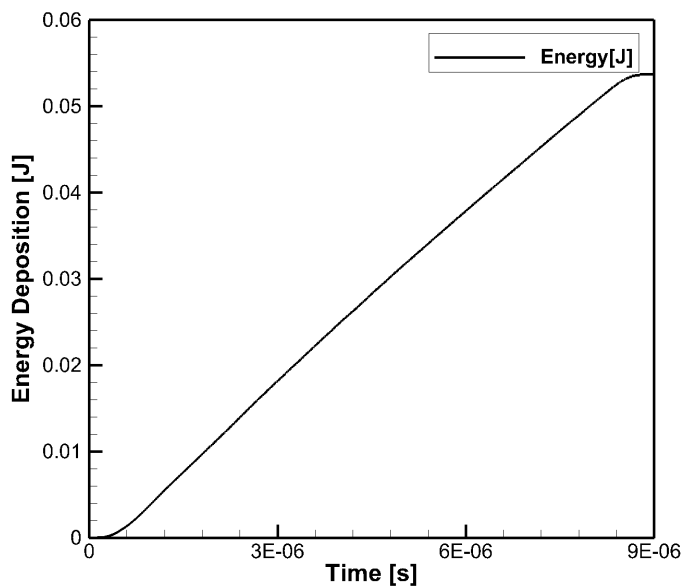


Figure 3.9 Time history of Joule heating energy. Ulsan Univ. case.

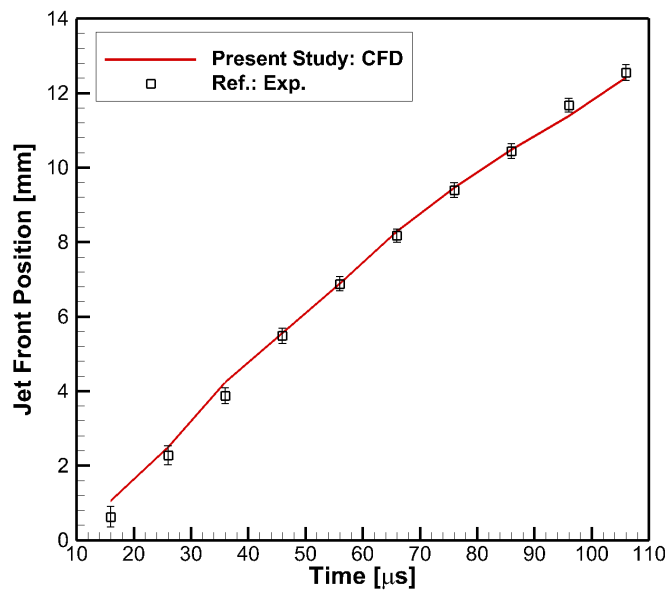


Figure 3.10 Comparison of jet front positions for validation. Ulsan Univ.case.

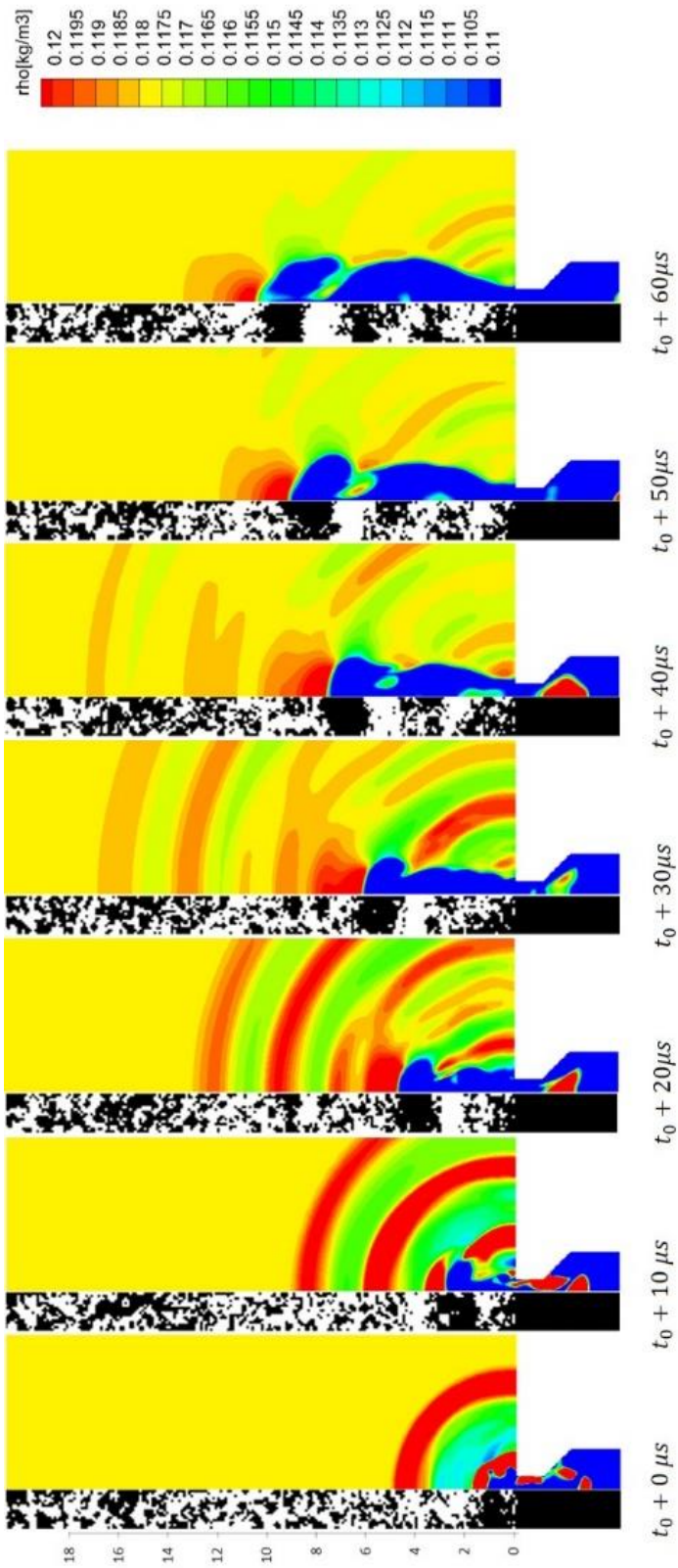


Figure 3.11 Schlieren images from experiment and density flow field from CFD.

3.2.3 Additional Explanations on Energy Dissipations

As it can be seen from the earlier subsections, the applied voltage waveforms, and thus the deposited or dissipated energy waveforms are different for the two validation cases. The effects of waveforms may affect the characteristics and performances of the actuator. Since many kinds of measurements from experiment are needed with the collaboration of the computations for the such investigations, it is beyond the scope of the current study. Instead, based on the literature, some possible different aspects according to waveforms are addressed briefly in this section [21].

The energy deposition waveform of ONERA case has rapid increase rate, meanwhile Ulsan Univ. case has constant gradient. For the rapid increase rate of energy deposition, the energy deposition is made in the shorter time compared to the constant gradient energy deposition. It is reported that the shorter energy deposition duration makes less temperature increase. Also, the dynamic pressure of ejected jet is higher for faster burst out of jet flow. On the other hands, the temperature increase for the constant gradient energy deposition is greater. Thus, more thermal stress may occur.

Even though the two validation cases have different energy deposition waveforms, the results of the analysis solver used in the current study show good accuracy.

Chapter 4. Numerical Analysis of Baseline Model

In this chapter, fundamental characteristics of SparkJet actuator are analyzed numerically. Analyses include jet flow characteristics, performance characteristics, frequency characteristics, and pressure wave behaviors inside the cavity. The target baseline model is the ONERA's SparkJet actuator which is analyzed in the Sec. 3.2.1. This model is selected as a baseline for the rest of the chapters unless otherwise stated. Thus, it is just called baseline to indicate the ONERA model in the current study from now on. The actuated environments and conditions are also the same: the atmospheric pressure and room temperature condition. The plasma source term is 3 mJ in total within 10 μ s as shown in Figure 3.5. The same computational grid system is employed.

In the current study, SparkJet actuator with a single operation is investigated. Thus, no actual operational frequency is considered. Rather, 1 kHz of virtual operational frequency is assumed so that individual pulsing of plasma generation does not affect the other pulsing of plasma generation. A report showed that 5 kHz of pulsing frequency is achieved for stable repetitive actuation [4]. Thus, 1 kHz of operational frequency is appropriate assumption for independent operation of a SparkJet actuator.

4.1 Jet Flow Characteristics

First, the effects of equilibrium properties are investigated. Even though the arc plasma utilized in a SparkJet actuator is assumed as thermochemical equilibrium plasma which is reflected through the thermodynamic properties and transport coefficients in the numerical analysis of this study, there is report that the jet flow produced by a SparkJet actuator shows nonequilibrium characteristics [4]. By comparing the jet front positions of different thermodynamic assumptions, the reported facts are confirmed.

It is best to establish and solve the continuity equations of chemical species and energy equations of plasma to analyze nonequilibrium effects. However, chemical reactions incorporated in the air plasma are very complicated and not entirely known yet. Thus, it is difficult to embedded in the computational solver. Moreover, the computational time cost for nonequilibrium assumption increases enormously compared to the equilibrium and calorically perfect gas assumptions. Instead of conducting a nonequilibrium gas computation, a calorically perfect gas assumption is used, which has specific heat ratio γ of 1.4. Because it can be considered as extreme case of nonequilibrium gas. It definitely and physically make sense that the specific heat ratio γ for nonequilibrium gas exists somewhere between that of a calorically perfect gas and an equilibrium gas at certain pressure and temperature. Thus, it can be said that there is a nonequilibrium effects if an actual jet front positions from experiments lies between the jet front positions calculated by a calorically perfect gas and an equilibrium gas assumption.

The density field from the computation results of equilibrium gas and calorically perfect gas are shown in Figure 4.1. It is clear that the jet front positions

of calorically perfect gas lead the those of equilibrium gas. The jet front positions from the computation results are compared to experimental data from reference as shown in Figure 4.2. It is confirmed from the figure that the experimental data from reference lie between the CFD data of equilibrium gas and calorically perfect gas from current study. To be specific, the results for the calorically perfect gas falls on the upper bound of the error bars in the experiment until about 40 μ s. Meanwhile, the equilibrium gas results fall on the lower bound of the error bars. More pressure and temperature rise than equilibrium gas, and less pressure and temperature rise than calorically perfect gas should be achieved in the earlier phase of energy deposition stage for the jet front positions to be closer to the experimental data in this period. These results lead to the interpretation of existence of nonequilibrium effects. Because the energy transfer from plasma to surrounding air for nonequilibrium gas must be higher than the equilibrium gas and lower than the calorically perfect gas. Beyond 40 μ s, calorically perfect gas results deviate from the experimental results. On the other hands, equilibrium gas results still fall between the error bars. This means that the amount of energy transfer from plasma to surrounding air is reasonable in the later phase.

Thus, it can be concluded that the thermal characteristics of the gas is nonequilibrium in the very earlier phase of energy deposition stage, which would eventually turn into equilibrium shortly. Nevertheless, since the entire results of equilibrium assumption fall into the experimental data, the assumption of equilibrium gas is quite reasonable and acceptable. In addition, equilibrium gas would have much benefit on the computational time cost compared to nonequilibrium and/or calorically perfect gas due to its time step. It is obviously secured to use equilibrium gas assumption.

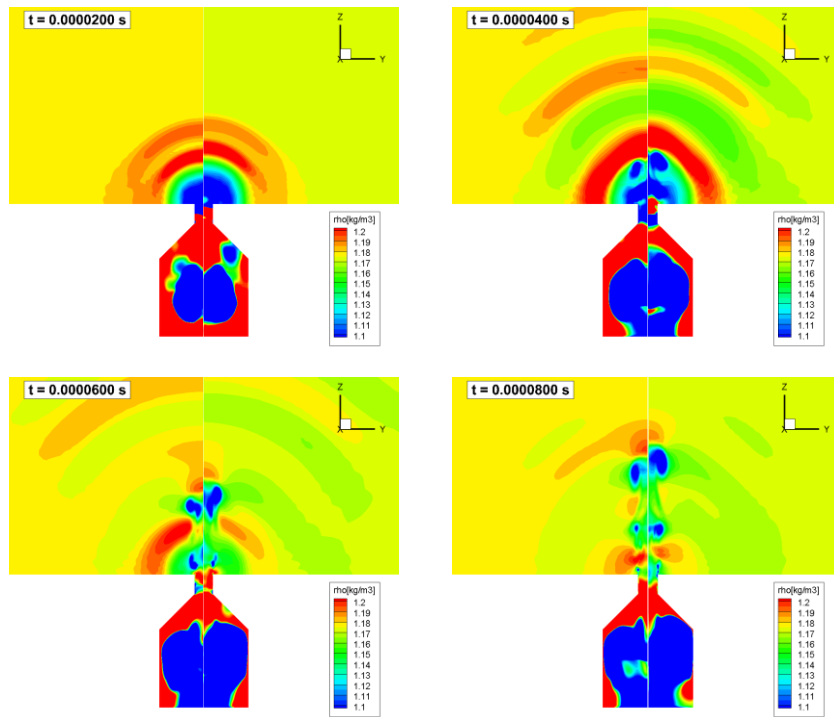


Figure 4.1 Density fields of SparkJet actuator:
Left) Equilibrium gas, right) Calorically perfect gas.

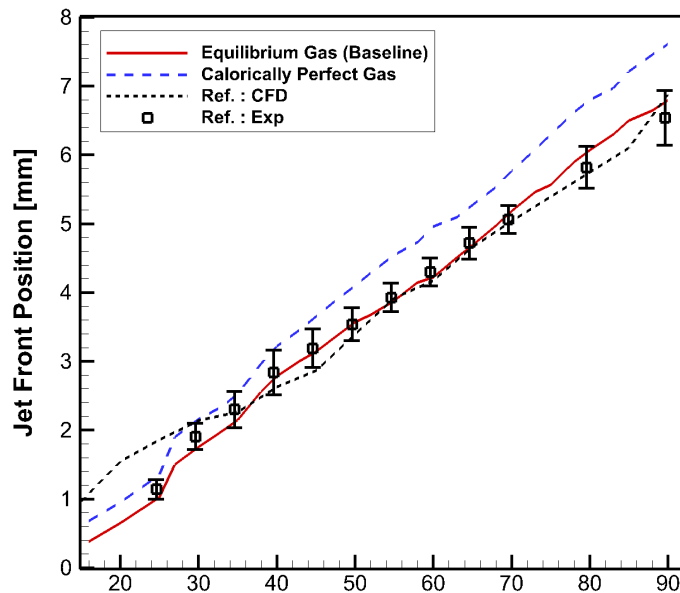


Figure 4.2 Jet front positions comparison of equilibrium gas and calorically perfect gas [22].

The enlarged density contour with streamlines of 60 μs is shown in Figure 4.3. This figure shows the detailed jet flow structure around orifice throat and exit. The jet flow is being exhausted and pressure waves are propagating through the orifice exit to the outer space which are came from inside the cavity. The jet front is indicated by a low density, and large density gradient region. There is tag with blue squared box in the figure. Also there is a vortex in the jet front. A tag with red squared box indicates it in the figure. This is formed when the jet flow bursts out through the orifice. Another vortex is formed right above the orifice exit, which is called the orifice exit vortex in the figure. Both vortices are generated by the expansion of flow at the orifice exit. A train of vortices are being developed in the same way and travel upward along the main body of the jet.

Each one of the intermittently expelled pressure waves from the orifice are distinguishable. The first pressure wave is ongoing farther from the jet front. The second one is going through the jet front and it is overlapped in the figure. The third one is at the entry of orifice exit and about to be expelled soon. The distinguished three pressure waves indicate that pressure waves are being exhausted even during the jet flow is being discharged.

These features of jet flow and pressure waves affect the performance characteristics such as thrust and total impulse of the SparkJet actuator.

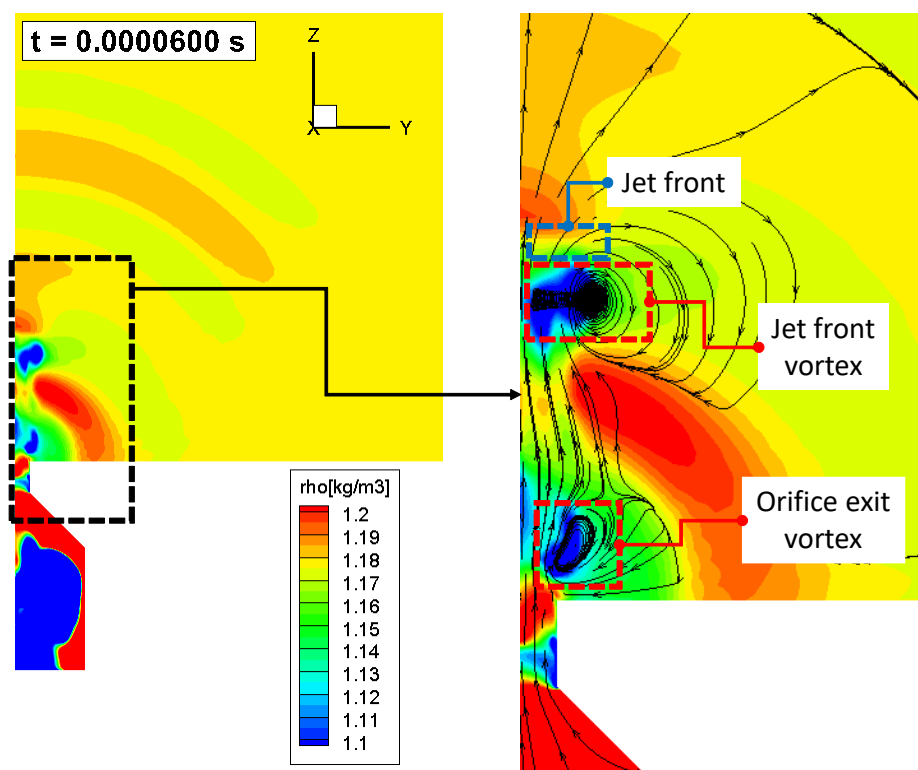


Figure 4.3 Density contour and streamlines at $60 \mu\text{s}$.

4.2 Performance Characteristics

The discharging jet flow and pressure waves of a SparkJet actuator produce thrust and total impulse which may be considered as typical performance factors. Both factors are expressed as follow as.

$$T = \dot{m}_{ori} \overrightarrow{V_{ori,n}} + (p_{ori} - p_{\infty}) A_{ori} \quad (4.1)$$

$$I_{total} = \int_0^{\tau} [\dot{m}_{ori} \overrightarrow{V_{ori,n}} + (p_{ori} - p_{\infty}) A_{ori}] dt \quad (4.2)$$

Here, \dot{m}_{ori} , $\overrightarrow{V_{ori,n}}$, and p_{ori} are mass flow rate, normal component of velocity, and pressure at the orifice exit, respectively. Also, p_{∞} and A_{oir} are ambient pressure and orifice area. Since the direction of the orifice is vertical to the surface of external flow field, the z direction velocity w is used instead of $\overrightarrow{V_{ori,n}}$. It is implied in the Equation (4.1) that thrust is a combination of jet momentum term and pressure term. They are expressed in $\dot{m}_{ori} \overrightarrow{V_{ori,n}}$ and $(p_{ori} - p_{\infty}) A_{ori}$, respectively. The sign of each terms is with respect to outflow direction of the ejected jet flow. The mass flow rate \dot{m}_{ori} is positive when the flow is going out through the orifice exit and negative when the flow is coming in through the orifice exit. The sign of velocity $\overrightarrow{V_{ori,n}}$ is the same as mass flow rate \dot{m}_{ori} . Thus the momentum term is always positive. On the other hands, pressure term becomes positive when the pressure at orifice is greater than the freestream pressure, and becomes negative when it is less than the freestream pressure. The thrust equation indicates that it can be negative when the absolute value of the pressure term is greater than the momentum term. The flow characteristics explained in the Sec. 4.1 also tells the

same trends because pressure waves are expelled intermittently. Thus, total impulse is used as an alternative performance factor which is calculated by Equation (4.2). Total impulse increases nearly monotonically and converges to a certain value when the actuation is terminated. However, in order to avoid the effect of oscillations in total impulse, the following average total impulse is introduced to specify a certain value for a total impulse.

$$I_{ave} = \frac{\int_0^{\tau} I_{total} dt}{t_{cycle}} \quad (4.3)$$

Here, t_{cycle} is an operational period of a SparkJet actuator. In the current study, operational frequency is assumed as 1 kHz so that the operational period becomes 1 ms.

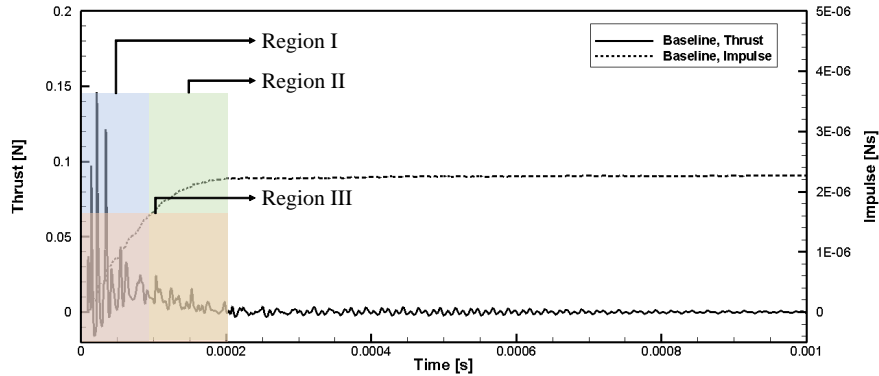


Figure 4.4 Thrust and total impulse of baseline.

In Figure 4.4, thrust and total impulse are shown in function of time. As expected, thrust shows a lot of oscillations and total impulse increases nearly monotonically until approximately 213 μ s. Even negative thrust occurs during the

oscillations, while generating the maximum thrust of 0.146 N. The total impulse is 2.27 μNs and the average total impulse is 2.09 μNs . Three different temporal “regions” are designated and shown in the figure. Each region is divided based on the representative characteristics of thrust and total impulse.

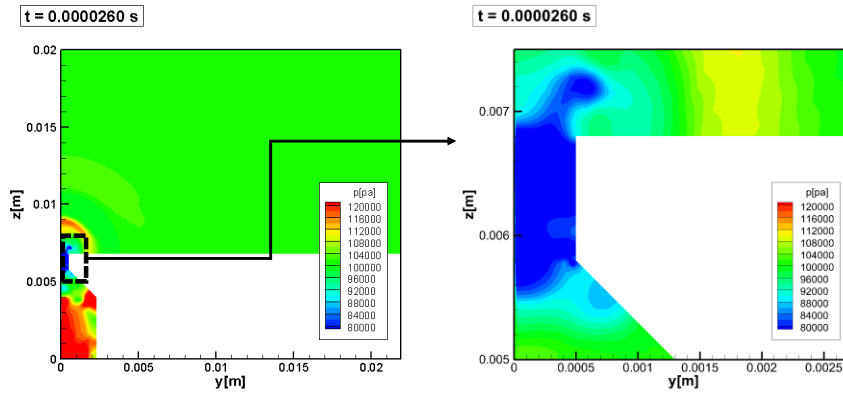
The first 71 μs is designated as region I where pressure waves and jet flow start to eject so that the actuator starts actuation, which means that thrust and total impulse begin to generate. The facts that thrust oscillates a lot and a large portion of total impulse increase occurs indicate that pressure wave behaviors inside the cavity is very active. Showing thrust lost and negative thrust, thrust is extremely oscillating compared to region II and until 1 ms. However, the negative thrust is limited to only local fractions compared to total actuation time, so that it does not mean the refresh stage. During oscillations, most of the primary peaks for thrust occur and the local minimum gradually increases until the end of the region I. Then the local minimum starts to decrease at the end of region I. Meanwhile, a total of 57 % of total impulse is generated in this region. More than half of total impulse is generated in less than one third of the total generation time. These result implies that interactions of pressure waves and/or shock waves inside the cavity in this region is very dynamic and complicated. Therefore, much of the jet flow and pressure wave ejections are concentrated in region I.

The period from 71 μs to 213 μs is designated as region II where the oscillating phenomena of thrust soothes, and the total impulse stops increasing and levels off. The thrust decreases gradually while net positive value is maintained. The mitigation of pressure wave behaviors inside the cavity is inferred. Due to this, the strength of bursting pressure waves through orifice exit is fairly weakened. It can be deduced that the dynamic components of pressure wave are eliminated and only the

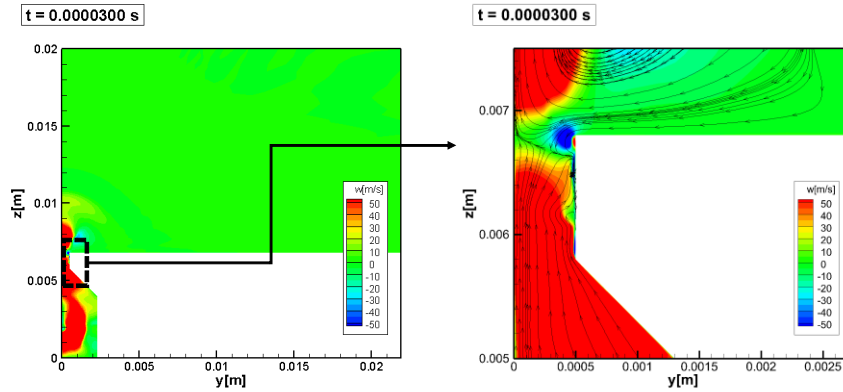
steady state components are maintained. After region II, the thrust oscillates in a small amplitude around zero. The total impulse no longer increases and converges to a certain value. For this baseline case, it is $2.27 \mu\text{Ns}$ as mentioned earlier.

Region III is a combination of region I and region II, which contains the characteristics of entire discharge stage. This region is covered in Sec. 4.3 where the frequency characteristics are addressed.

The reasons for loss of thrust and negative thrust can be explained by Figure 4.5 which shows the flow field near the orifice. Figure 4.5 (a) shows the pressure contour at $26 \mu\text{s}$. It is shown that the pressure wave just exhausted through the orifice, and pressure drop below the ambient pressure is followed. Consequently, instant thrust becomes negative, and it becomes positive again by upcoming pressure waves and jet flow. Figure 4.5 (b) shows z direction velocity and streamlines at $30 \mu\text{s}$. Flow is separated due to adverse pressure in the entire domain of the orifice throat wall. Also, direction of flow in the orifice exit is changed due to the orifice vortex and flow penetrates back into the orifice. These two aspects lead to the thrust loss because the flow directions cannot have kept in one way. Different orifice exit configurations should prevent vortices from re – entering the orifice.



(a) Pressure contour.



(b) Z direction velocity contour and streamlines.

Figure 4.5 Flow fields near orifice: (a) pressure contour, (b) Z direction velocity contour and streamlines.

So far, performance characteristics of baseline SparkJet actuator are analyzed. Thrust showed a lot of oscillations, and sometimes it even gone to minus. The reasons for fluctuations and thrust loss are the pressure drop after a pressure wave burst, flow separation in the orifice throat wall, and re – entering of flow due to orifice vortices. Depending on the thrust oscillation and total impulse increase aspects, jet discharge stage is divided into three regions and analyzed. Region I includes the start of the actuation and inside the cavity is expected to have dynamic

components of pressure waves or shock waves. Region II includes the level off of the actuation and it is expected that state of the inside the cavity becomes stable and only the steady components of pressure waves or shock waves remain. After region II, a SparkJet actuator stops the actuation and get into refresh stage. Region III is the combination of region I and II so that it represents the whole period of the actuation. The oscillating aspects of thrust on each region are analyzed through FFT in the next section.

4.3 Frequency Characteristics

Frequency analysis through the conducting FFT of thrust is done. The oscillations of thrust are highly originated from pressure wave inside the cavity since it is the driving momentum of actuation. Thus, the FFT results of thrust can be considered as frequency characteristics of SparkJet actuator. FFT is conducted on each region mentioned in the Sec. 4.2 as well as the full range of thrust. The time interval between the data points of thrust is 5×10^{-10} s which makes the total sampling frequency of 2×10^9 Hz. 2 GHz sampling frequency makes the FFT results reliable, and Nyquist frequency would not be a problem. A Hanning window functions is applied for the two reasons. First, the signal pattern of thrust is unknown before the analysis. Second, in order to reduce the leakage of thrust signal.

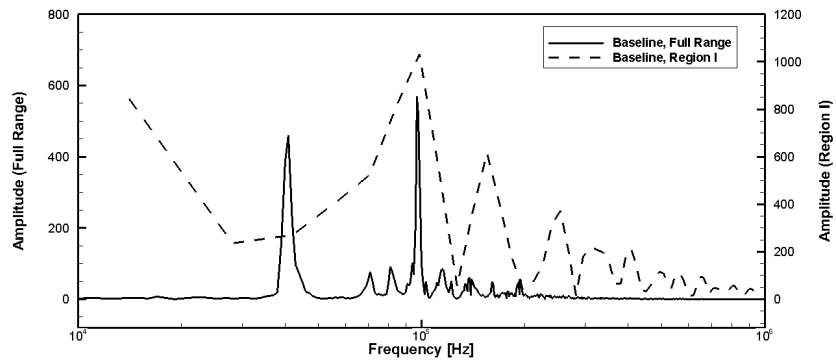
The results of FFT of thrust are shown in Figure 4.6 and each region is compared to full range. In Figure 4.6 (a), full range and region I are compared. Region I has large peaks that are spaced by approximately 50 kHz starting from around 100 kHz. Since the peak near 100 kHz is also appeared in full range, it is expected that pressure wave behavior corresponding to this frequency component is maintained from the start to the end of the SparkJet actuator operation. Other higher frequency components are expected to be fade away. No exceptional peak is visible near 40 kHz for region I, but in full range. It seems that pressure wave behaviors corresponding to frequency near 40 kHz is mixed up in region I so that no exceptional peak is appeared. However, after some of dynamic components are gone, a single remarkable peak is remained as shown in full range. This indicates that pressure wave behaviors resulting from the pressure waves and/or shock waves interactions inside the cavity causing thrust and total impulse generation in region I

are extremely dynamic and cover a wide range of frequency domain. Through the performance analysis in Sec. 4.2, similar conclusion is deduced. However, a large portion of them extinct as time goes. It seems that maintaining the interactions as long as possible is the one way to improve the performance of the SparkJet actuator, because region I is the region in which more than half of total impulse is generated.

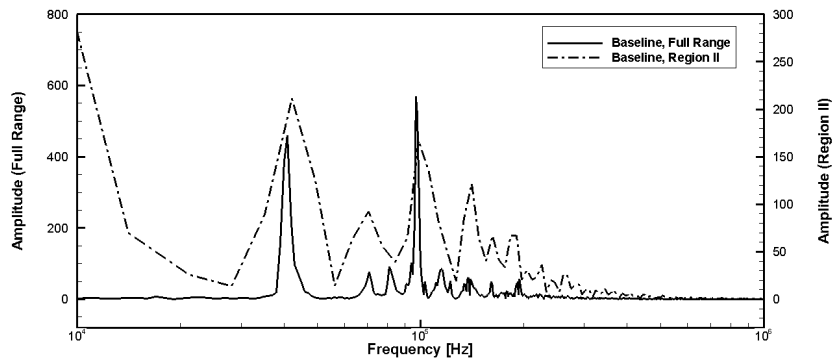
Overall amplitude of peaks in region II is decreased compared to region I. Frequency peak near 100 kHz is appeared in both full range and region II. The most different thing from region I is that frequency peak near 40 kHz is noticeable which is also shown in full range. It can be deduced that some of pressure wave behaviors only corresponding to 40 kHz are remained, while causing the neighboring frequencies are died out. These two peaks can be considered as steady components. Higher frequency peaks, especially higher than 300 kHz are imperceptible in region II. These results infer that significant fractions of dynamic pressure wave behaviors are fairly mitigated. Dynamic components are removed naturally by pressure waves and the jet ejection through the orifice, leaving only steady components. The similar conclusion is reached in Sec. 4.2. Viscous dissipation may also play a role in weakening the pressure wave strength inside the cavity. It seems that maintaining the pressure wave behavior inside the cavity corresponding for steady components strongly is another way to improve the performance of the SparkJet actuator. The survival period of these components is of no concern since they are steady components.

In region III, two major peaks are appeared with some of minor peaks. The major peaks are located near 100 kHz and 40 kHz, which are also appeared in full range. To be precise, they are 96.99 kHz and 40.99 kHz, respectively. Consequently, these two frequencies are the natural frequencies that are related to

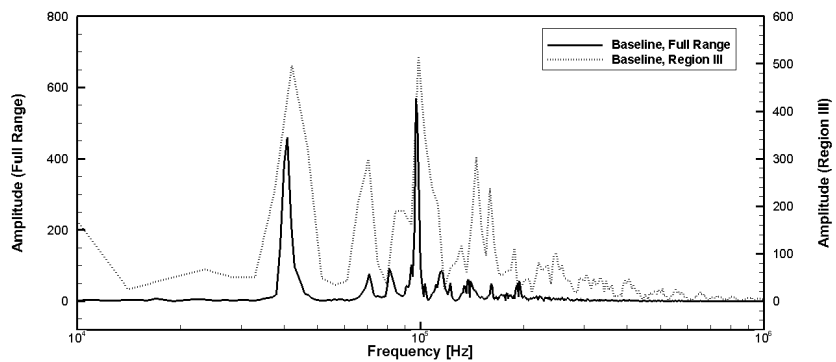
the operation of the SparkJet actuator. Let the higher frequency be the first natural frequency f_1 and the lower frequency be the second natural frequency f_2 . These two frequencies are likely to originate from the pressure wave behaviors inside the cavity as explained so far. Detailed flow pattern analyses inside the cavity are followed in the Sec. 4.4 for the causes of two natural frequencies.



(a) Region I.



(b) Region II.



(c) Region III.

Figure 4.6 Fast Fourier Transform of thrust: (a) full range and region I, (b) full range and region II, (c) full range and region III.

4.4 Pressure Wave Behaviors Inside the Cavity

Pressure waves and momentum jet discharge result from the complicated interactions and behaviors of pressure waves and/or shock waves inside the cavity. Correspondingly, these contribute overall driving pressure of a SparkJet actuator as a reservoir pressure, and affect the oscillations of thrust, thus affecting the performance. In this sense, detailed behaviors of pressure wave inside the cavity is investigated.

As soon as energy deposition is made inside the cavity, pressure and temperature are increased, and shock wave is generated almost at the same time. Then shock wave travels isotropically until it incidents toward the cavity wall, then become pressure waves as it becomes weaker due to dissipation. Thus, just pressure wave is mentioned from now on, but still the shock wave is included. Due to the geometry difference of side and bottom wall of the cavity, the pressure wave reflects in different forms. Since the reflected pressure waves interact and become another source of pressure increase which result in thrust and impulse, understanding the behavior of the reflected pressure waves inside the cavity is important.

According to the geometry of the cavity, two possible conceptual, although not strict, propagation directions for the reflected pressure waves are shown in Figure 4.7. They are namely the $r - axis$ and $z - axis$ directions, respectively. The $r - axis$ direction shown in Figure 4.7 (a) is the direction that pressure wave reflected on the side wall of the cavity on the $xy plane$, which is perpendicular to the $z axis$. The cylindrical geometry of the cavity wall makes the reflected pressure wave circular shape. Thus, the pressure wave propagates in the radial direction and gathers at the center of the cavity. The $z - axis$ direction shown in Figure 4.7 (b)

is the direction that pressure wave reflected from the side and bottom walls on the xz plane, which is the same as the yz plane and parallel to the z axis. Since the side wall reflection is already considered, only the bottom wall reflection is considered. The bottom wall is flat so that the planar reflected pressure wave is formed and travels upward toward the orifice exit. Some fraction of it exits the cavity through the orifice, while another fraction reflects back toward the bottom of the cavity after reflecting from the upper wall of the cavity. These two kinds of reflected pressure waves are expected to interact and merge so that they provide additional driving pressure for the SparkJet actuator. Moreover, the reflection and merging of pressure waves occur continuously.

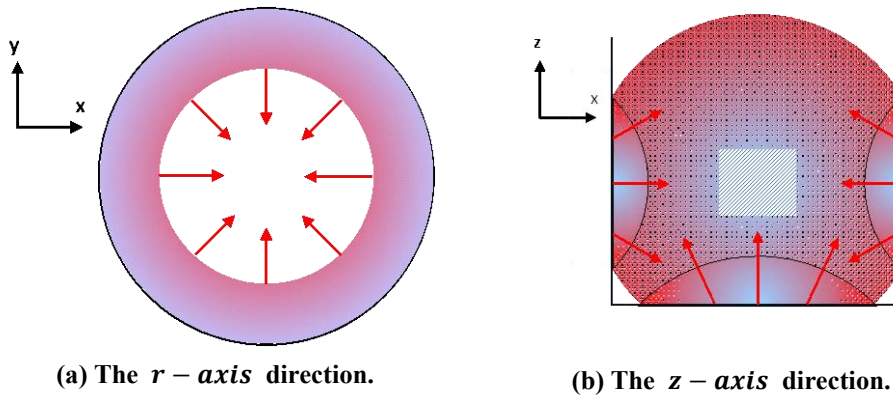


Figure 4.7 Schematic diagram of the reflected pressure wave inside the cavity: (a) The r – axis direction, (b) The z – axis direction..

Those two conceptual patterns of pressure wave propagations and reflections are verified in the pressure contour of the calculated result of baseline. Figure 4.8 shows cross – sectional view of pressure contour of baseline on the xy plane at $z = 0.002$, where the center of the electrodes is located. The energy deposition is made on this plane and pressure wave is generated and propagates. The pressure

wave propagates in concentric circle as shown at 1 μs and incidents on to the cavity side wall at 3 μs , then reflects. After that, the pressure wave is reflected and propagates in the $r - axis$ direction at 5 μs and merges at the center of the cavity at 7 μs . The reflection and merge of the pressure wave results in additional pressure increase beside from the very first energy deposition. Figure 4.9 shows cross – sectional view of pressure contour of baseline on the yz plane. The pressure wave propagates in concentric circles like the one on the xy plane at the first. At 3 μs , pressure wave incidents and reflects on to the bottom wall. Since it propagates isotropically, some portion of reflected pressure wave goes toward the orifice exit along the $z - axis$ direction, and other portion goes in the $r - axis$ direction. For the reflected pressure wave propagating in the $z - axis$ direction, it merges with the pressure wave reflected on the side wall propagating in the $r - axis$ direction at the center of cavity as shown at 7 μs . The reflected pressure wave in the $r - axis$ and $z - axis$ directions are confirmed as the primary reflected pressure wave components inside the cavity.

Since it is the reflected pressure waves that generate the natural frequencies, those would be changed when the amount of energy deposition is changed. When the amount of energy deposition is increased, the temperature is increased more so that the speed of sound and pressure wave are increased, and vice versa. Subsequently, the natural frequencies would be increased as the energy deposition is increased. The natural frequencies for different energy depositions are listed in Table 4.1 shown in Figure 4.10. Although not much differences due to a little change in the energy deposition, natural frequencies are shifted a little bit higher according to energy deposition.

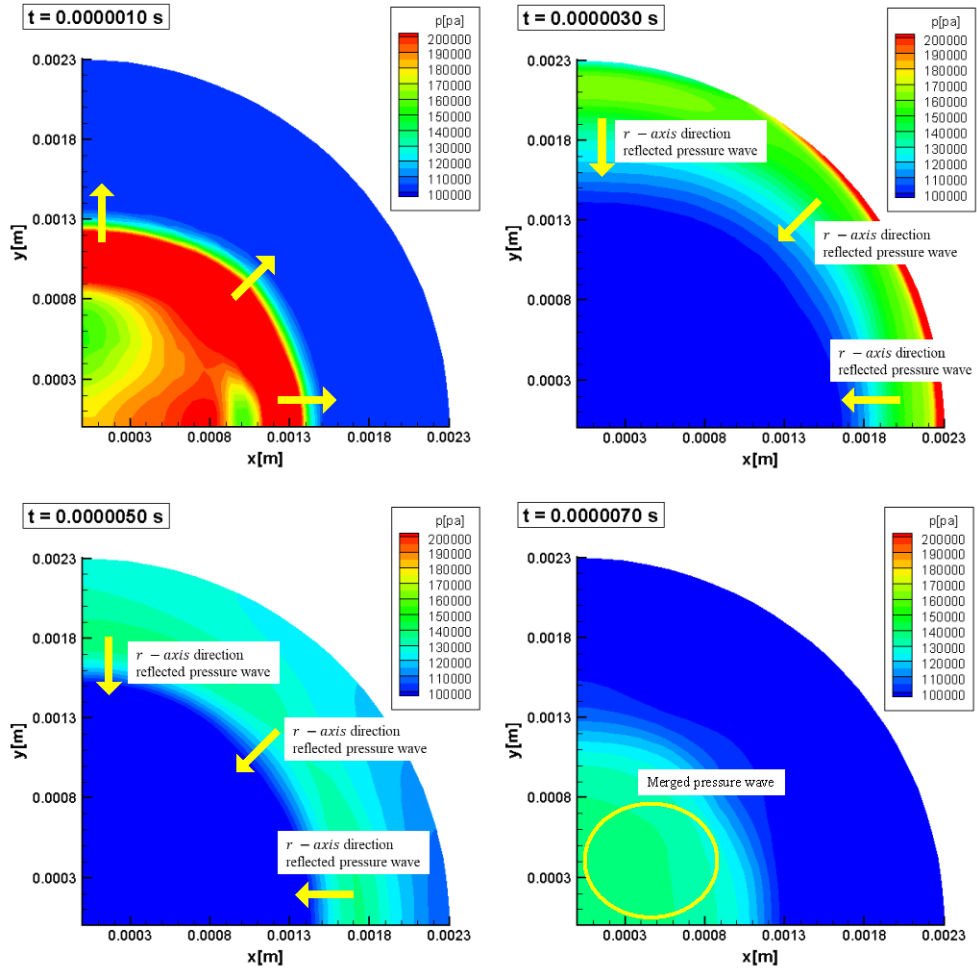


Figure 4.8 Pressure contour of baseline at $z = 0.002$.

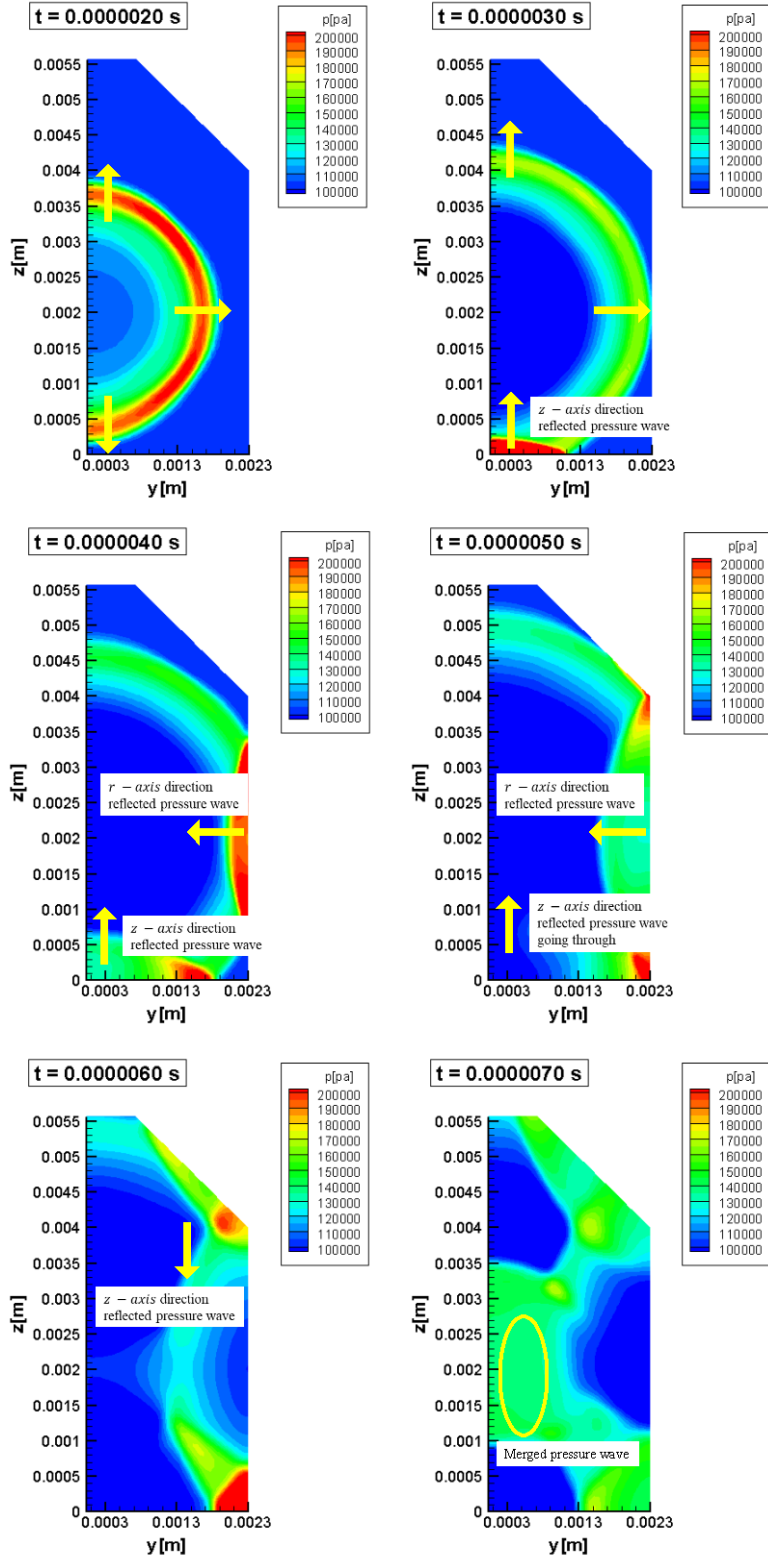


Figure 4.9 Pressure contour of baseline at $x = 0$.

Table 4.1 Comparison of the natural frequencies for energy depositions.

| Cases | f_1 (kHz) | Δf_1 (%) | f_2 (kHz) | Δf_2 (%) |
|-----------|-------------|------------------|-------------|------------------|
| 3 mJ Case | 96.99 | ... | 40.99 | ... |
| 5 mJ Case | 97.99 | 1.03 | 41.99 | 2.44 |
| 7 mJ Case | 98.99 | 2.06 | 41.99 | 2.44 |

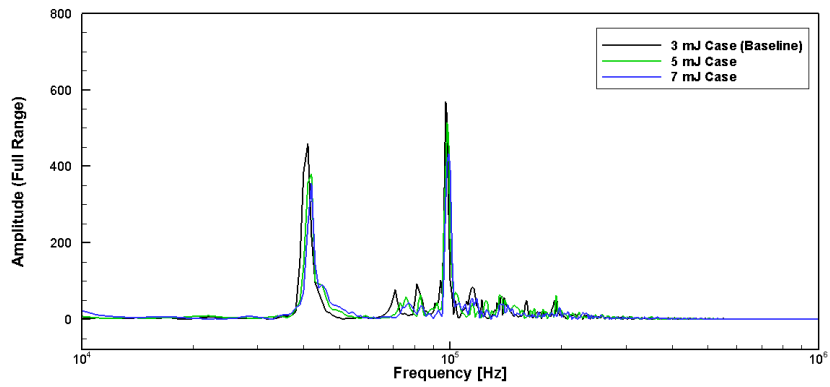


Figure 4.10 Fast Fourier transform of thrust for different energy depositions.

Chapter 5. Numerical Analysis of Frequency Characteristics

In the previous chapter, various characteristics of baseline SparkJet actuator are analyzed. Among them, frequency characteristics are originally introduced by this study and not fully understood for their causes and effects. The origins of the two natural frequencies are not verified yet.

In this chapter, the causes and effects of natural frequencies are investigated in accordance with pressure wave behaviors. The oscillations produced by reflected pressure waves are correlated to the natural frequencies through some of parameter changes. Six different configurations listed in Table 5.1 are analyzed and compared with baseline. Cases A, B, and C are designed to verify the effects of oscillations in the $r - axis$ direction inside the cavity. The electrode gap and diameter are varied while constant energy deposition volume is maintained. Meanwhile, cases D – G are designed to verify the effects of oscillations in the $z - axis$ direction inside the cavity. They have the same cavity height but different taper angles. Although there might be an argument for the changes in the total volume including the cavity and converging section, only a limited opportunity exists in changing the vertical element of cavity while maintaining the cavity height. Because all of the geometry factors are coupled together and cannot be changed independently. Therefore, the taper angle modification is the only option to vary the vertical element of the cavity to change the effective distance in the $z - axis$ direction.

Table 5.1 Designe variables for Frequency Characteristics Analysis.

| Design variables | Values | | | | | | | |
|----------------------------|----------|--------|--------|--------|--------|--------|--------|--------|
| | Baseline | Case A | Case B | Case C | Case D | Case E | Case F | Case G |
| Orifice exit diameter (mm) | 1.0 | 1.0 | 1.0 | 1.0 | 1.0 | 1.0 | 1.0 | 1.0 |
| Orifice throat length (mm) | 1.0 | 1.0 | 1.0 | 1.0 | 1.0 | 1.0 | 1.0 | 1.0 |
| Orifice taper angle (°) | 45 | 45 | 45 | 45 | 0 | 15 | 30 | 60 |
| Cavity diameter (mm) | 4.6 | 4.6 | 4.6 | 4.6 | 4.6 | 4.6 | 4.6 | 4.6 |
| Cavity height (mm) | 4.0 | 4.0 | 4.0 | 4.0 | 4.0 | 4.0 | 4.0 | 4.0 |
| Electrode height (mm) | 2.0 | 2.0 | 2.0 | 2.0 | 2.0 | 2.0 | 2.0 | 2.0 |
| Electrode gap (mm) | 1.2 | 0.54 | 1.8 | 4.0 | 1.2 | 1.2 | 1.2 | 1.2 |
| Electrode diameter (mm) | 1.0 | 1.5 | 0.82 | 0.548 | 1.0 | 1.0 | 1.0 | 1.0 |

5.1 Oscillations in the $r - axis$ direction: Electrode Shape

As mentioned in the introduction of the chapter, four cases including baseline are compared to investigate the oscillation in the $r - axis$ direction inside the cavity. Basically, their electrode shapes changed, and thus the aspect ratio of energy deposition. For baseline, its ratio of electrode diameter to cavity diameter is 0.22 and the ratio of electrode gap to cavity diameter is 0.26. For case A, the ratio of electrode diameter to cavity diameter is 0.33, and the ratio of electrode gap to cavity diameter is 0.11. For case B, the ratio of electrode diameter to cavity diameter is 0.18, and the ratio of electrode gap to cavity diameter is 0.39. For case C, the ratio of electrode diameter to cavity diameter is 0.12, and the ratio of electrode gap to cavity diameter is 0.87. The aspect ratios of each cases are 1.2, 0.36, 2.2, and 7.3, respectively. Figure 5.1 shows the energy deposition configurations of each cases which is varied according to the electrode shape. It is more intuitive to distinguish the differences in visual. The four cases have the same amount of energy deposition within the same volume of energy deposition. Thus, the results would depend on the electrode shape only.

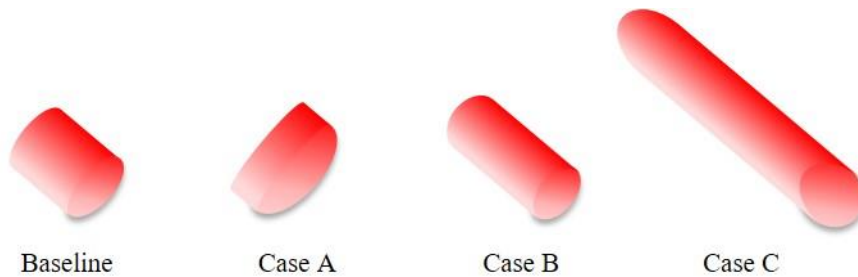


Figure 5.1 The configurations of energy deposition for different electrode shape.

The natural frequencies for different electrode shapes are listed in Table 5.2 and the results of FFT of thrust for full range and each regions are shown in Figure 5.2 and Figure 5.3. The first natural frequency f_1 for baseline, case A, and B have no differences while that of case C is decreased by 3.09 %. The second natural frequency f_2 for baseline, case C, and D have no differences while that of case B is decreased by 2.44 %. The reasons for the differences can be confirmed by the FFT of each region for four cases.

In region I as shown in Figure 5.3 (a), case A, B, and C have numerous peaks at various frequencies just as baseline, including the peak near the first natural frequency f_1 . The amplitudes of the peaks close to the first natural frequency f_1 are nearly the same except for case C. It is reduced a little compared to other three cases. Meanwhile, similar behavior is shown close to the second natural frequency f_2 for all the compared cases. These indicate that pressure wave reflections responsible for the first natural frequency f_1 in case C is decreased a little compared to other cases, but those responsible for the second natural frequency f_2 is similar for all four cases.

In region II as shown in Figure 5.3 (b), frequency trends show discrepancy near the first natural frequency f_1 . Overall peaks in case B and C are smeared compared to the other two cases. However, peaks in the second natural frequency f_2 are still very similar. These imply that, in case B and C, pressure wave reflections responsible for the first natural frequency f_1 are mitigated, whereas those responsible for the second natural frequency f_2 is still maintained. However, the trend is different in region III as shown in Figure 5.3 (c). Only case C has reduced first natural frequency f_1 . It means that the reflected pressure wave generating the first natural frequency

f_1 for case B in region I is fairly strong enough even though it is mitigated a little in region II. Consequently, still the first natural frequency f_1 is generated for case B in the operating phase of the SparkJet actuator. On the other hands, the first natural frequency f_1 for case C is not strong enough in region I and it is not maintained in region II. Thus, it is not able to affect the whole operating phase of the SparkJet actuator.

Table 5.2 Comparison of the natural frequencies for different electrode shape.

| Cases (Aspect Ratio) | f_1 (kHz) | Δf_1 (%) | f_2 (kHz) | Δf_2 (%) |
|-------------------------|-------------|------------------|-------------|------------------|
| Baseline (1.2) | 96.99 | ... | 40.99 | ... |
| Case A (0.36) | 96.99 | ... | 40.99 | ... |
| Case B (2.2) | 96.99 | ... | 39.99 | -2.44 |
| Case C (7.3) | 93.99 | -3.09 | 40.99 | ... |

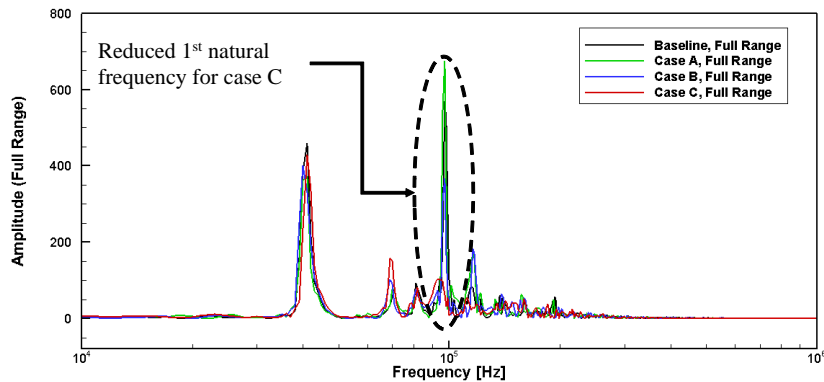
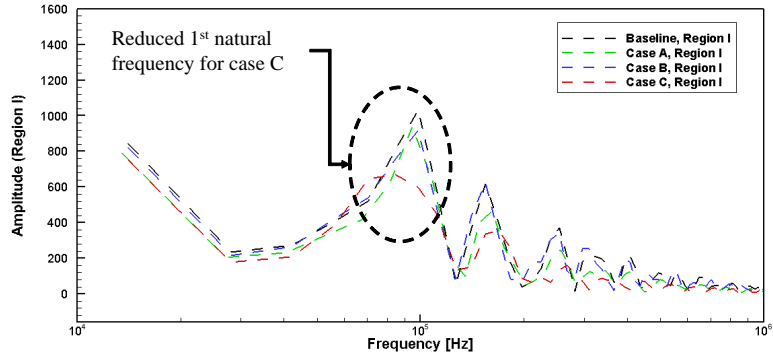
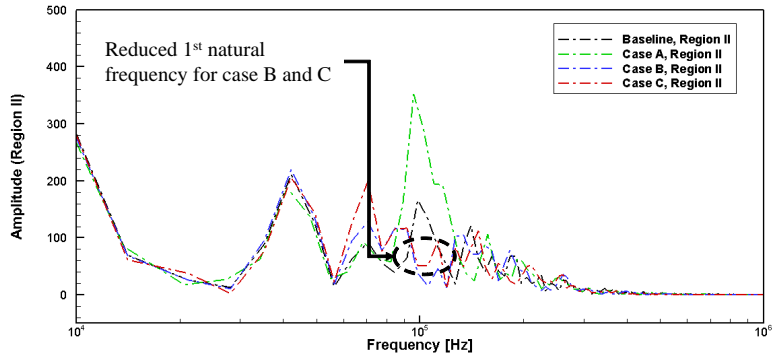


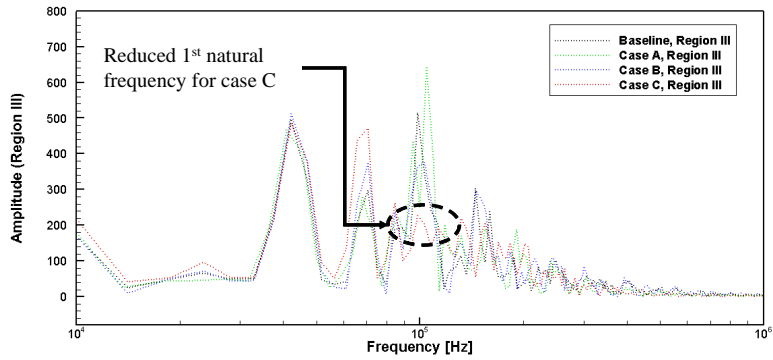
Figure 5.2 Full range Fast Fourier transform of thrust for different electrode shape.



(a) Region I.



(b) Region II.



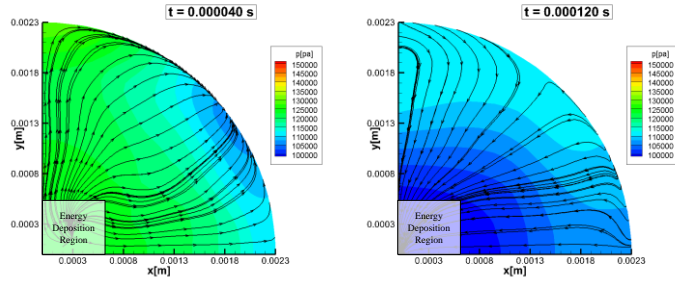
(c) Region III.

Figure 5.3 Fast Fourier transform of thrust for different electrode shape: (a) region I, (b) region II, (c) region III.

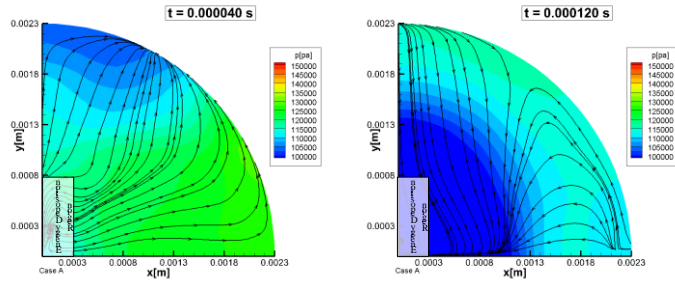
According to these frequency trends, case C is the only case that the first natural frequency f_1 is reduced in the operating phase, which is maintained in the other three cases in the overall jet discharge stage. In the full range, case C also has a peak near the first natural frequency which is 93.99 kHz. However, this peak is more than 80 % less than that of the baseline as shown in Figure 5.2. The effect of the first natural frequency f_1 is greatly reduced in case C. Consequently, the first natural frequency f_1 presents only at the very beginning of the SparkJet actuator operation and then fades away in a short time for case C. Physically, the pressure wave reflections which cause the first natural frequency f_1 are not long lived. As an evident to this, pressure contour and streamline at $z = 0.002$ m, as shown in Figure 5.4, where the center of the electrode lies, prove the different flow patterns for each cases. Continuous pressure wave behaviors in the $r - axis$ direction are generated as a result of reflections on the side wall for the baseline, case A, and B. For case C, on the other hand, this pressure wave behavior is disappeared at 120 μ s and the flow direction is changed into rotating around in the θ direction. The case C does not have the first natural frequency f_1 and reflected pressure wave continuously propagating in the $r - axis$ direction, whereas the other three cases have the natural frequency and the pressure wave behavior. Since the electrode shape is the only design variable between these four cases, the different flow structure must be caused from the electrode shape. These results indicate that the oscillating pressure wave behavior reflected in the $r - axis$ direction is the one that generates the first natural frequency f_1 .

It is concluded from these results that the pressure waves reflected in the $r - axis$ direction is the cause of the first the natural frequency f_1 . It is observed that

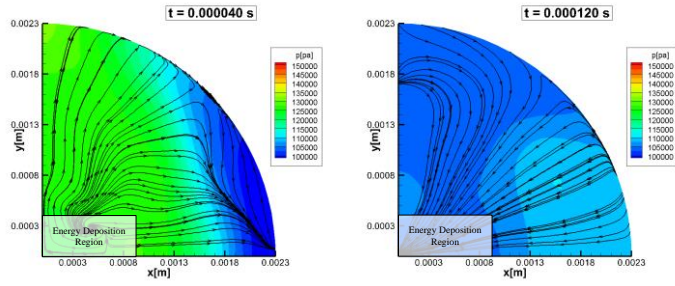
the first natural frequency f_1 disappeared when the reflected pressure wave in the $r - axis$ direction is disappeared and while the second natural frequency f_2 is remained. In addition, the values of the second natural frequency f_2 are rarely changed even the design parameter is changed. Thus, it may infer that the two natural frequencies are independent to each other. This needs further investigations regarding the second natural frequency f_2 so that confirmative conclusion is postponed for a while.



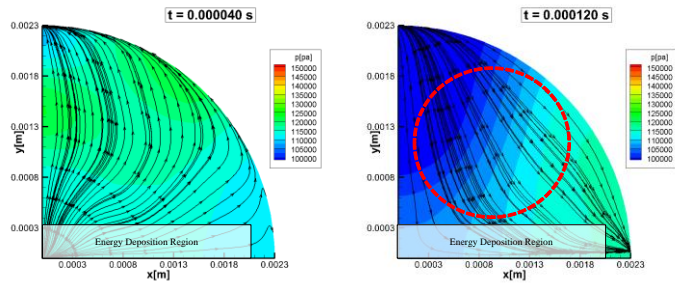
(a) Baseline



(b) Case A



(c) Case B



(d) Case C

Figure 5.4 Pressure contour and streamline for different electrode shape:

(a) baseline, (b) case A, (c) case B, (d) case C

5.2 Oscillations in the $z - axis$ direction: Taper Angle

As mentioned in the introduction of the chapter, five cases including baseline are compared to investigate the oscillation in the $z - axis$ direction inside the cavity. Basically, their taper angle is changed, and thus the effective distance in the $z - axis$ direction. For baseline, its distance from the bottom of cavity to orifice entrance is approximately 5.8 mm. For case D, E, F, and G, it is approximately 4 mm, 4.48 mm, 5.04 mm, and 7.12 mm, respectively. The amount of increases of the distance is inclined approximately from -31.03% to 22.76% based on the baseline. The Figure 5.5 shows the cavity configurations for different taper angle.

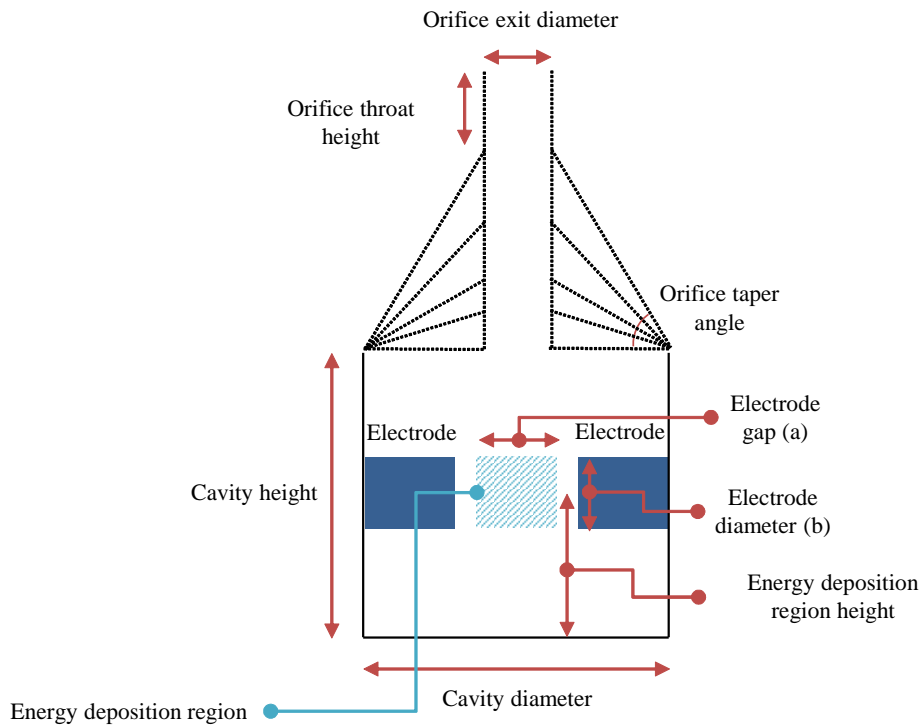


Figure 5.5 The configurations of cavity for different taper angle.

The natural frequencies for different taper angles are listed in Table 5.3 and the results of FFT of thrust for full range and each regions are shown in Figure 5.6 and Figure 5.7. The first natural frequency f_1 for all the five compared cases are within 2 % differences approximately. This is because some portion of the pressure wave reflected on the bottom and top wall of the cavity propagate in the $r - axis$ direction as explained in Sec. 4.4. Thus, this is not a large difference compared to that of the second natural frequency f_2 . The second natural frequency shows difference of about 22 % at its maximum. The reasons for the differences can be confirmed by the FFT of each region for four cases.

Table 5.3 Comparison of the natural frequencies for different taper angle.

| Cases (Taper Angle) | f_1 (kHz) | Δf_1 (%) | f_2 (kHz) | Δf_2 (%) |
|---------------------|-------------|------------------|-------------|------------------|
| Baseline (45°) | 96.99 | ... | 40.99 | ... |
| Case D (0°) | 98.99 | +2.06 | 49.99 | +21.95 |
| Case E (15°) | 98.99 | +2.06 | 44.99 | +9.76 |
| Case F (30°) | 95.99 | -1.03 | 41.99 | +2.44 |
| Case G (60°) | 98.99 | +2.06 | 34.99 | -14.63 |

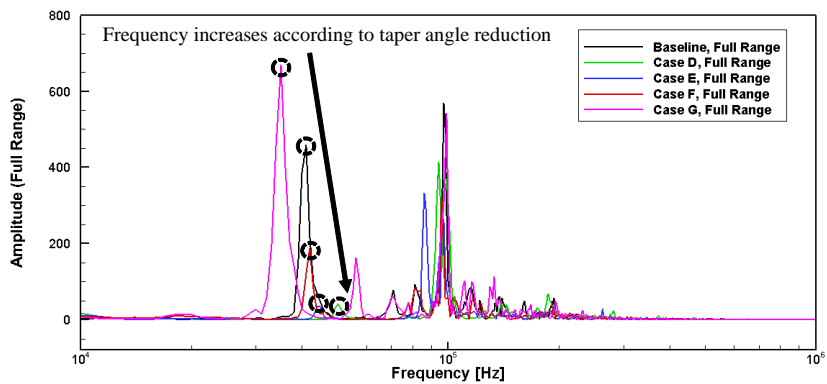


Figure 5.6 Full range Fast Fourier transform of thrust for different taper angle.

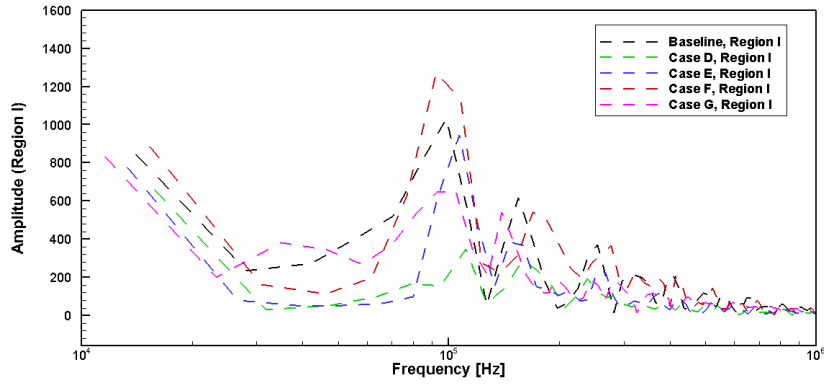
In region I as shown in Figure 5.7 (a), the five compared cases have numerous peaks at various frequencies. The amplitudes of the peaks close to the first natural frequency f_1 are nearly the same. Also, similar behavior is shown close to the second natural frequency f_2 for all the compared cases. These indicate that pressure wave reflection trends in region I for the first natural frequency f_1 and the second natural frequency f_2 are very similar between the compared cases.

However, discrepancy is occurred in the second natural frequency f_2 in region II as shown in Figure 5.7 (b). Even though overall amplitudes are different near the first natural frequency f_1 , related phenomena is not discussed since its tendency in full range for each case is very similar as mentioned earlier in this section. The peaks near the second natural frequency f_2 are different by each cases. They are shifted as the taper angle is changed. This phenomenon is related to the distance propagated by the pressure wave in the $z - axis$ direction. This is the effective height in the $z - axis$ direction that pressure wave propagate from the bottom wall of the cavity to the top wall of the cavity. The effective height in the $z - axis$ direction depends on the taper angle. The smaller taper angle allows the reflected pressure wave to travel a shorter distance in the $z - axis$ direction, meanwhile the larger taper angle allows a longer distance. The second natural frequency f_2 in region III also shows similar trend. It is decreased as the taper angle increased.

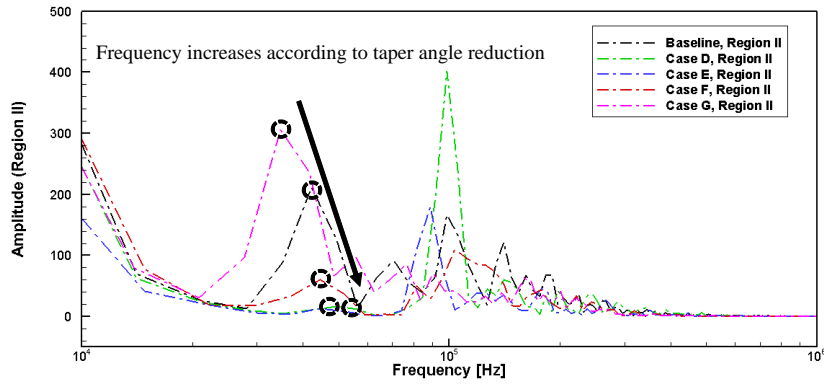
Since the same amount of energy is deposited under the same initial conditions, the speed of the pressure wave inside the cavity must be very close to each other for the compared five cases. Because the speed of sound for the compared cases only differs within 10 % calculated by peak average temperature. This means that the speed of the pressure wave for the compared cases is also not different so much.

Unfortunately, the speed for the pressure wave cannot easily be specified due to the very complicated flow interactions inside the cavity. However, it can be inferred that the pressure wave propagating shorter distance with the similar speed has shorter travel time, and thus has higher frequency. Accordingly, since the effective distance in the $z - axis$ direction is reduced depending on the taper angle decrease, the frequency increase related the $z - axis$ direction is observed.

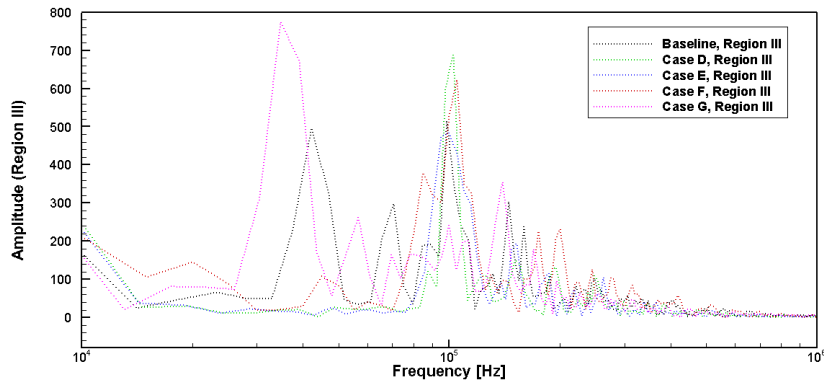
From these results, it is concluded that the second natural frequency f_2 depends on the pressure wave reflected in the $z - axis$ direction because it is increased as the taper angle is decreased. It is inferred in the section 5.1 that pressure wave components for the first natural frequency f_1 and the second natural frequency f_2 are independent from each other. As a result of the current section, it is confirmed that the two components are independent. Because the second natural frequency f_2 for the compared cases is different while the first natural frequency f_1 is similar to each other. Accordingly, the reflected pressure wave in the $r - axis$ direction and the $z - axis$ direction can be dealt independently. Let this aspect be named direction separable property.



(a) Region I.



(b) Region II.



(c) Region III.

Figure 5.7 Fast Fourier transform of thrust for different taper angle: (a) region I, (b) region II, (c) region III.

5.3 Effects of Oscillations on the Performance

It is investigated so far that the natural frequencies of SparkJet actuator are originated from pressure wave reflections inside the cavity. The natural frequencies are observed in the thrust, which is one of the major performance factor. Thus, it is expected that considering the oscillations of a SparkJet actuator is very important in predicting and/or estimating the performance of the actuator. Consequently, quantitative effects of oscillations on the SparkJet actuator performance are analyzed by smoothing the thrust of the baseline case.

It is revealed that baseline has two natural frequencies: 96.99 kHz and 40.99 kHz. These two frequencies are used as cutoff frequency for the smoothing of thrust. Results are shown in Table 5.4 and Figure 5.8. Smoothed by the first natural frequency f_1 as a cutoff frequency is smoothing A. For this case, the effect of the first natural frequency f_1 is eliminated. Smoothed by the second natural frequency f_2 as a cutoff frequency is smoothing B. Most of the oscillating effects of natural frequencies and others are removed for smoothing B. For smoothing A, the maximum peak thrust is decreased from 0.146 N to 0.025 N, which is -83.11% , and average total impulse is decreased from 2.09 μNs to 1.84 μNs , which is -11.65% . For smoothing B, the maximum peak thrust is decreased from 0.146 N to 0.020 N, which is -86.35% , and average total impulse is decreased from 2.09 μNs to 1.77 μNs , which is -15.35% . Thrust decreases dramatically and total impulse also decreases fairly when oscillation is removed.

Table 5.4 Effect of oscillations on the performance

| Cases | T_{max} (N) | ΔT_{max} (%) | I_{ave} (μ Ns) | ΔI_{ave} (%) |
|-------------|---------------|----------------------|-----------------------|----------------------|
| Baseline | 0.146 | ... | 2.09 | ... |
| Smoothing A | 0.025 | −83.11 | 1.84 | −11.65 |
| Smoothing B | 0.020 | −86.35 | 1.77 | −15.35 |

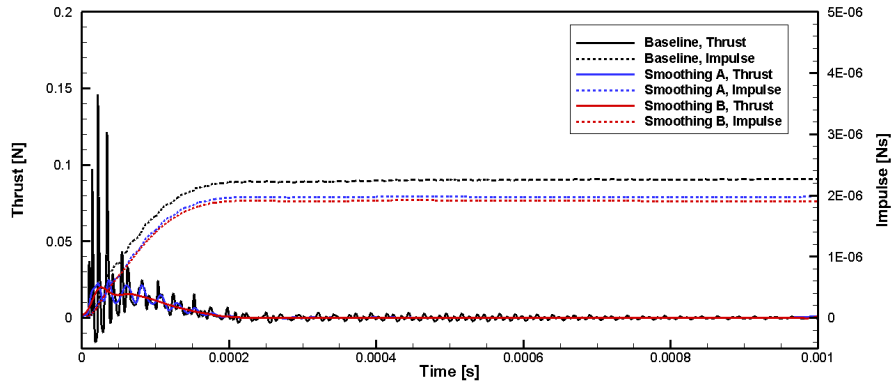


Figure 5.8 Thrust and total impulse of baseline and their smoothing results.

The quantitative effects of the reflected pressure wave are induced from the smoothing results. First, since the first natural frequency f_1 is used as cutoff frequency in smoothing A, the reflected pressure wave in the $r - axis$ directions is eliminated. As it is shown in the Figure 5.8, the extreme oscillations at the earlier phase in the thrust are removed, and those at the after around $50 \mu s$ is still exist. The elimination of the first natural frequency f_1 is confirmed, whereas the second natural frequency f_2 is remained. Consequently, the pressure wave reflected in the $r - axis$ directions affect approximately 11 % on the total impulse. Second, both of the reflected pressure waves in the $r - axis$ and $z - axis$ directions are eliminated since the second natural frequency f_2 is used as cutoff frequency in smoothing B. As shown in the Figure 5.8, nearly all of the oscillations are removed

in the thrust of smoothing B. Accordingly, approximately 15 % of the total impulse is affected by the reflected pressure waves including the $r - axis$ and $z - axis$ directions.

It is concluded that the oscillations produced by pressure wave reflections of SparkJet actuator influence 15 % of its total impulse performance at its maximum, and even much more for thrust performance. Thus, it is essential to consider oscillations into account when predicting the SparkJet actuator performance.

5.4 Summary

In this chapter, the origins of oscillations and the two natural frequencies are investigated in accordance with pressure wave behaviors inside the cavity.

First, the origin of the first natural frequency f_1 is confirmed by changing the electrode shape. It is the pressure wave reflected in the $r - axis$ direction that produces the first natural frequency, which is 96.99 kHz for baseline. When electrode shape is changed, so that the energy deposition region becomes very long, the amplitude of the first natural frequency is decreased more than 80 % compared to other cases. Moreover, pressure wave that reflects and propagates in the $r - axis$ direction is gone a few moments later in the operation.

Second, the taper angle of converging section is changed to confirm the origin of the second natural frequency f_2 . Pressure wave reflected in the $z - axis$ direction is responsible for the generation of the second natural frequency f_2 , which is 40.99 kHz for baseline. When the effective height in the $z - axis$ direction is changed according to the taper angle, the natural frequency is also changed in accordance. The second natural frequency f_2 is increased as the taper angle is decreased.

From these results, it is concluded that the oscillations produced by the reflected pressure waves in two directions inside the cavity are the causes of the natural frequencies: the $r - axis$ direction and the $z - axis$ direction. Also, these two reflected pressure waves are independent from each other.

The effects of oscillations are investigated by comparing the thrust and total impulse of baseline with their smoothed results. The reflected pressure wave in the $r - axis$ direction affects approximately 11 % on the total impulse. In overall, all

the oscillations produced by the $r - axis$ and $z - axis$ directions, and some other small ones affect approximately 15 % on the total impulse. As a result, it is essential to take the oscillations produced by the reflected pressure wave into account for the prediction and/or estimation of the performance of the SparkJet actuator. In addition, the natural frequencies of the SparkJet actuator must be considered in designing and manufacturing the actuator so as not to affect the frequency characteristics of the entire system where the actuator be installed.

Chapter 6. Numerical Analysis of Performance Characteristics

In Chapter 5, frequency characteristics of SparkJet actuator are analyzed through changes in some of design variables. During the design variable changes, there are change in thrust and total impulse performance which are not investigated in the previous chapter.

In this chapter, numerical analyses on the performances of SparkJet actuator such as thrust and total impulse are conducted. In addition, average flow variables inside the cavity of SparkJet actuator are examined. All of these are conducted through parametric studies as a preliminary study for the designs of the actuator. The performance factors are related to the flow variable states inside the cavity. However, both of them are difficult to measure and correlate each other experimentally. The small size of the actuator makes it mechanically difficult to manufacture considering many design variables. Various measurement techniques are not easily applicable on to this small device. In addition, plasma makes the cavity much harsher environment for physical measurements. It may electrically and/or physically damage the equipment. For these reasons, numerical parametric study is conducted in the current study.

Based on the baseline model used in the earlier chapters, four kinds of design variables are selected for the parametric studies, two of which are used in Chapter 5. Some of design variables are connected to others so that those are not able to separate perfectly from each other. The four parameters are 1. Electrode shape, 2. Taper angle, 3. Electrode height, and 4. Orifice diameter. Value changes for each parameter are introduced in each subsections of the current chapter.

6.1 Electrode Shape

The first parameter for numerical analysis of performance characteristics is the electrode shape. Analyzed cases are the same as those used in the Sec. 5.1: baseline, case A, case B, and case C as listed in the Table 5.1.

The thrust at the orifice exit and average total impulse are listed in Table 6.1, and graphically shown in Figure 6.1. As it can be seen from the table, thrust is decreased up to approximately 20 % for case B at its maximum. Thrust of case C and case D are also decreased, but no regular trend is found. As mentioned in the earlier chapters, thrust oscillates a lot and thus cannot represent the performance of the actuator. Meanwhile, the total impulse is converged to a certain value and may represents the performance of the actuator. The average total impulse is decreased 1.54 % for case B and to 3.21 % for case C. As shown in the Figure 6.2, the cavity average pressure for the four compared cases has almost no differences. Thus, there is no close correlation in the performance and the cavity average pressure.

Since the driving pressure of each cases are rarely different, total impulse decrease depends solely on the behaviors of pressure waves inside the cavity which is the reduction of the reflected pressure waves in the $r - axis$ direction. It is concluded that the reflected pressure waves in the $r - axis$ direction affects approximately 11 % on the total impulse as shown in smoothing A in Chapter 5. This result is from the smoothed result so that it is the ideal case that most of the reflected pressure wave in the $r - axis$ direction is removed. Moreover, all of the frequencies near the first natural frequency f_1 and higher are removed completely. In contrast, although the reflected pressure waves for case C eventually disappears, there exists the reflected pressure waves at the beginning of the actuator operation

as shown in Sec. 5.1. In addition, neighboring and higher frequencies are not completely removed. As seen in Sec. 5.1, the reflected pressure waves in the $r - axis$ direction is generated in region I. Also, neighboring frequencies are observed in the full range of the FFT analysis. Thus, it can be considered that the smoothing A shows the ideal effects of the disappearance of the reflected pressure waves in the $r - axis$ direction, while, case C shows the practical effects of it. Therefore, it is approximately 3 % of total impulse in actual that the reflected pressure waves in the $r - axis$ direction influence.

Table 6.1 Thrust and average total impulse for different electrode shape.

| Cases (Aspect Ratio) | T_{max} (N) | ΔT_{max} (%) | I_{ave} (μ Ns) | ΔI_{ave} (%) |
|-------------------------|---------------|----------------------|-----------------------|----------------------|
| Baseline (1.2) | 0.146 | ... | 2.09 | ... |
| Case A (0.36) | 0.116 | -20.54 | 2.09 | ... |
| Case B (2.2) | 0.140 | -4.43 | 2.06 | -1.54 |
| Case C (7.3) | 0.101 | -3.09 | 2.02 | -3.21 |

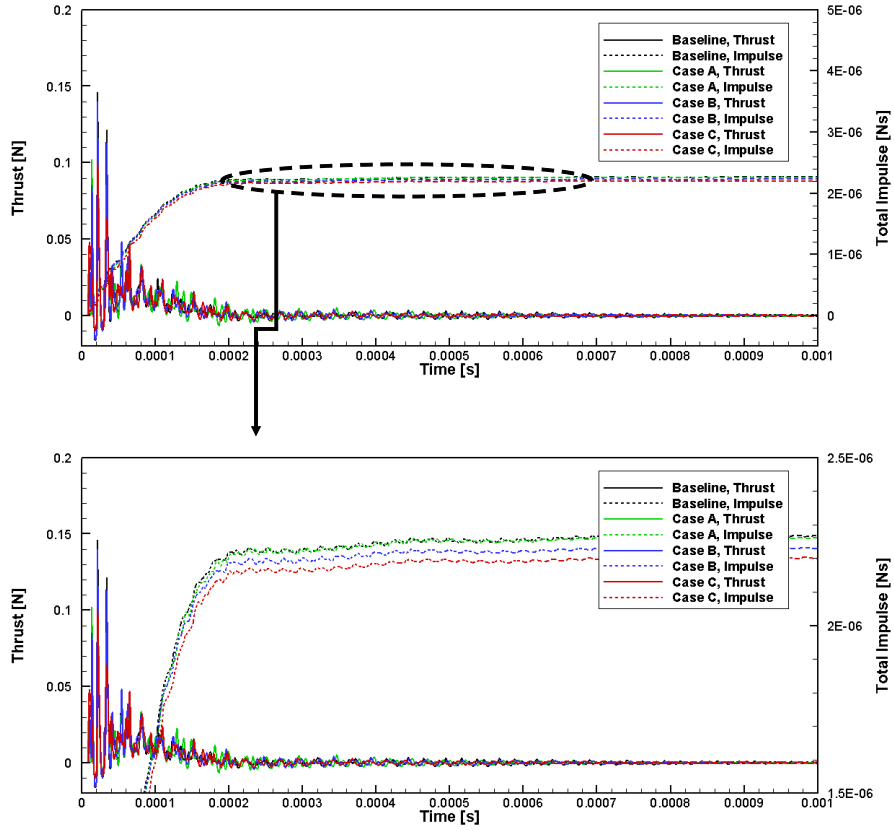


Figure 6.1 Thrust and total impulse for different electrode shape.

It also stated in the Sec. 5.1 that the flow direction of reflected pressure waves in the $r - axis$ direction is changed into the θ direction for case C. This phenomenon led a little bit of cavity average pressure drop qualitatively. Cavity average pressure for compared cases are shown in Figure 6.2. The cases with the reflected pressure waves in the $r - axis$ direction alive have almost similar trends in the flat top region, approximately from $5 \mu s$ to $30 \mu s$. However, the case C which has disappeared reflected pressure waves in the $r - axis$ direction show a little bit of drops approximately $20 \mu s$ to $30 \mu s$. This is the effect of the disappeared reflected pressure wave and the immediate cause of loss of performance.

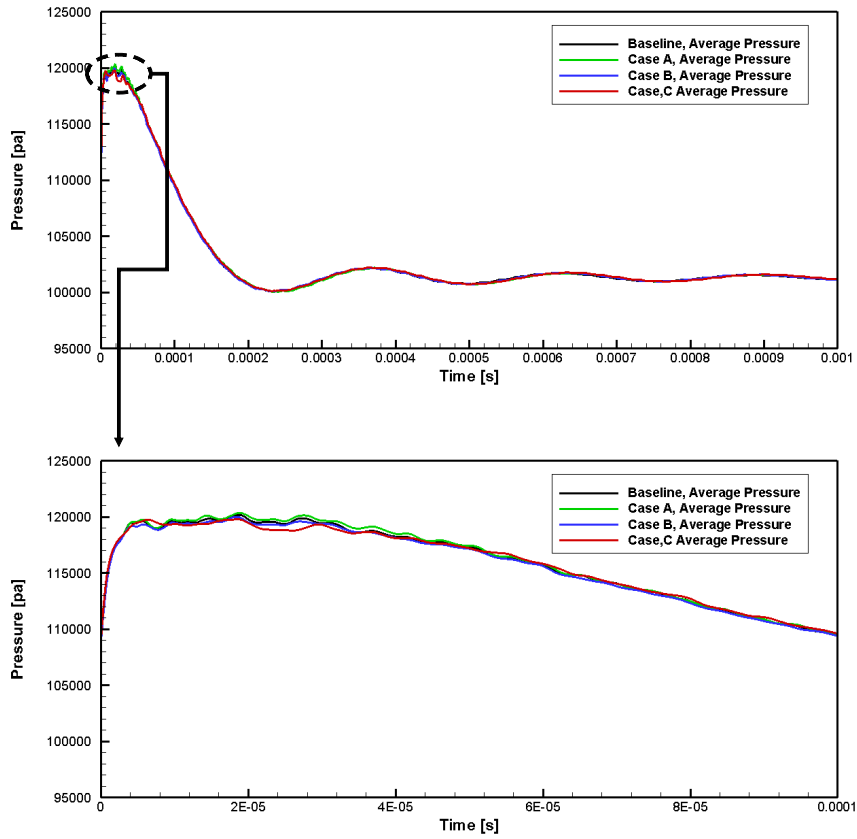


Figure 6.2 Cavity average pressure for different electrode shape.

Through these results, it is essential to consider and put effort on determining the electrode shape when designing a SparkJet actuator. This includes the electrode diameter and electrode gap. Those design variables, together with the cavity diameter, determine the energy deposition aspect ratio. This is the key factor that affects the behaviors of reflected pressure waves in the $r - axis$ direction, and thus the performance of a SparkJet actuator. Specifically, the total impulse is at its greatest when the energy deposition ratio is close the unity. The greatest average total impulse listed in the Table 6.1 is $2.09 \mu\text{Ns}$ for baseline and case A. The aspect ratio of baseline is 1.2 and that of case A is 0.36. However, baseline has 0.22 % greater

total impulse than case A at the end of the actuation cycle as shown in Figure 6.3, which is hard to identify in Figure 6.1. The total impulse for case B is decreased by 1.66 %, which has aspect ratio of 2.20. The total impulse for case C, whose aspect ratio is as large as 7.30, is decreased by 2.95 %. Accordingly, it is shown that the aspect ratio of energy deposition region close to the unity has the greatest total impulse.

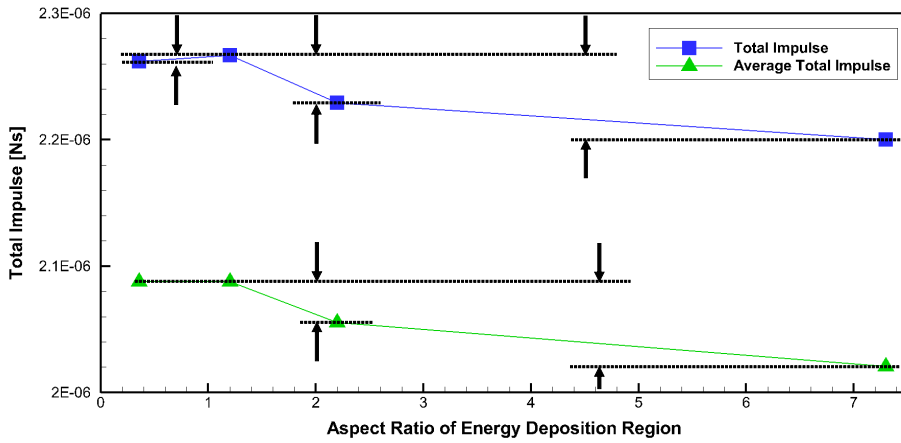


Figure 6.3 Total impulse and average total impulse comparison for different electrode shape.

In conclusion, it is important design the electrode diameter, electrode gap, and cavity diameter to keep the aspect ratio of energy deposition region close to unity to maximize the total impulse. However, physical electrode gap must not be too large in order for the generation of plasma considering the operating pressure. Because the possible electrode gap for the proper generation of plasma is influenced by the surrounding pressure.

6.2 Taper Angle

The second parameter for numerical analysis of performance characteristics is the taper. The analyzed cases are the same as those used in the Sec. 5.2: baseline, case D, case E, case F, and case G as listed in the Table 5.1. Reasonably, effects of dissipations due to total height changes and differences of total cavity volume are questionable. Total control of parameters regarding those effects are very limited for the changes in taper angle. Variables such as effective height which is determined by changes in both taper angle and cavity height should be considered. However, those are beyond the scope of the current study since change of more than one parameters are related. Thus, only the effects of taper angel are considered.

The thrust at the orifice exit and average total impulse are listed in Table 6.2, and graphically shown in Figure 6.4. Thrust is decreased by 10.18 % for case D, 60.06 % for case E, 37.96 % for case G, and 9.67 % for case F. Highly oscillating phenomena of thrust does not show a consistent trend. The average total impulse is decreased up to 16.75 % for case E, and increased up to 0.54 % for case F. In other words, average total impulse of SparkJet actuator may differ as much as approximately 17 % depending on the taper angle. The average pressure inside the cavity, as shown in Figure 6.5, does not directly explain the reasons for the total impulse differences according to taper angle. The average pressure inside the cavity is increased as the taper angle is decreased. It is because the total volume of the cavity is decreased as the taper angle is decreased with the same operating condition.

The trend of the total impulse, or average total impulse, is not the same as that of cavity average pressure. These trends are shown in Figure 6.6. The average total impulse increase in the order of taper angle 15°, 0°, 30°, 45°, and 60°.

Meanwhile, the maximum average pressure inside the cavity increases in the order of taper angle 60° , 45° , 30° , 15° , and 0° . The reason for the cavity average pressure trend is that the total cavity volume reduces as taper angle decreases as mentioned earlier. These indicate that simply maximizing the driving pressure of SparkJet actuator is not an answer for design of a better performing actuator.

Table 6.2 Thrust and average total impulse for different taper angle.

| Cases (Taper Angle) | T_{max} (N) | ΔT_{max} (%) | I_{ave} (μNs) | ΔI_{ave} (%) |
|-------------------------|---------------|----------------------|------------------------------|----------------------|
| Baseline (45°) | 0.146 | ... | 2.09 | ... |
| Case D (0°) | 0.131 | -10.18 | 1.91 | -8.49 |
| Case E (15°) | 0.124 | -15.14 | 1.73 | -17.30 |
| Case F (30°) | 0.149 | 1.90 | 1.97 | -5.64 |
| Case G (60°) | 0.132 | -9.67 | 2.10 | 0.54 |

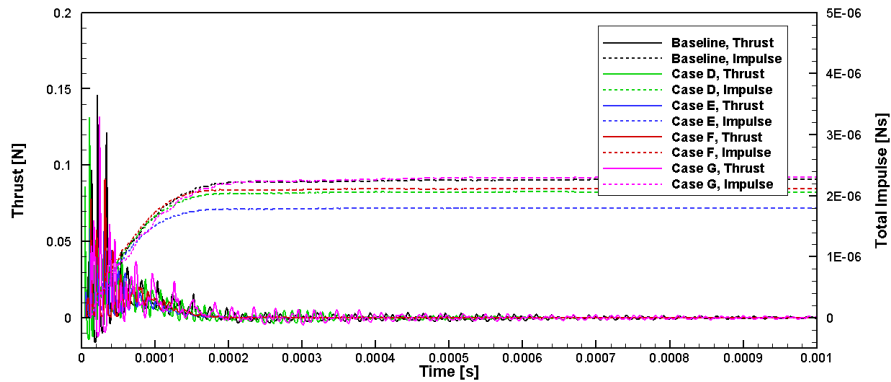


Figure 6.4 Thrust and total impulse for different taper angle.

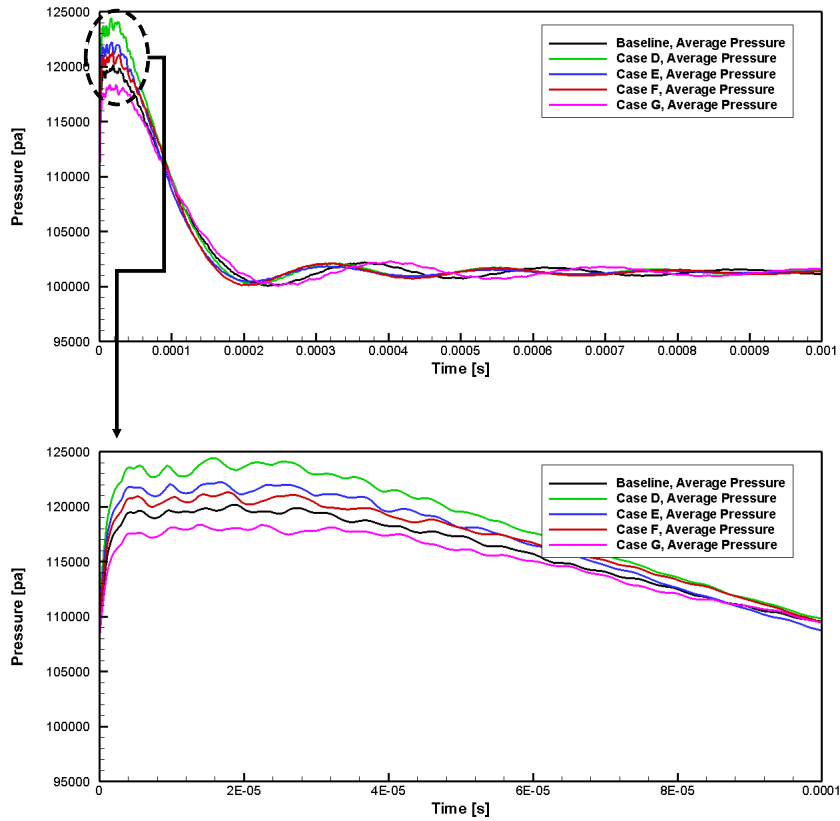


Figure 6.5 Cavity average pressure for different different taper angle.

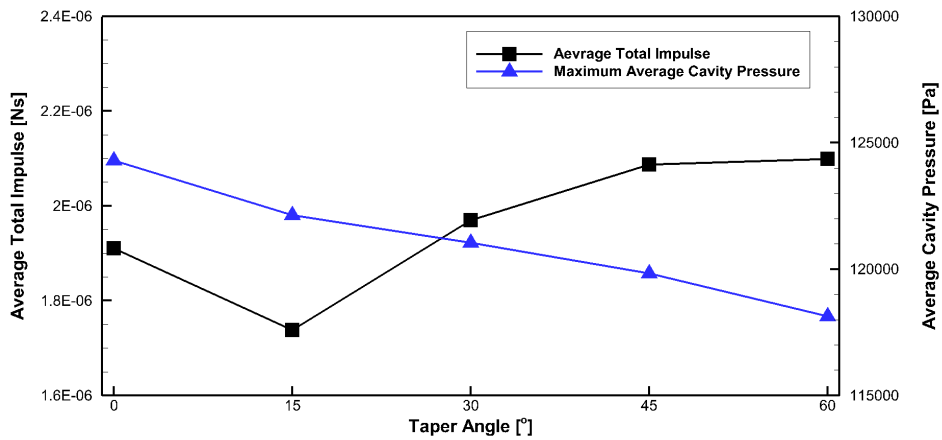
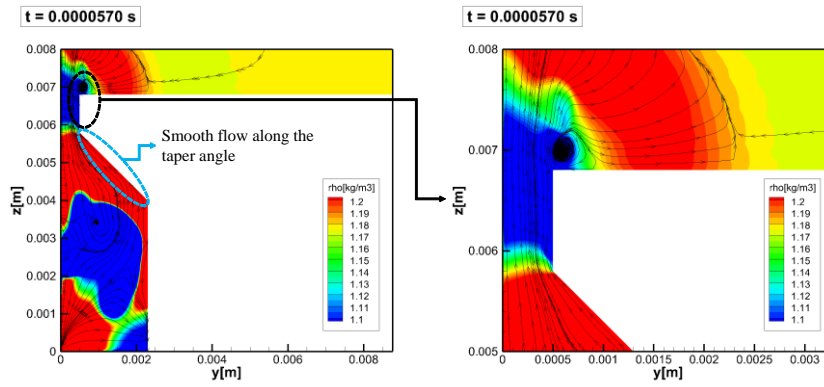


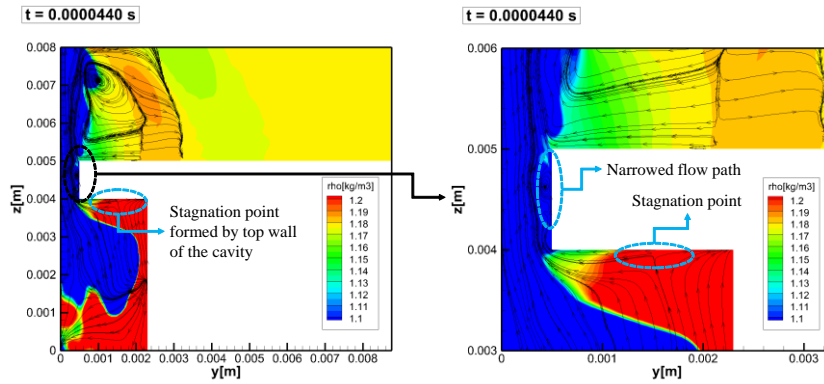
Figure 6.6 Total impulse, average total impulse, and max average pressure comparison for different electrode shape.

Taper angle affects structure of outgoing flow near the orifice entrance as shown in Figure 6.7. Due to the taper angle, flow smoothly directs toward the orifice along the upper cavity wall for the baseline as shown in Figure 6.7 (a). In addition, flow turns smoothly between upper cavity wall and the orifice throat entrance so that no flow expansion is occurred. As a result, flow path area is nearly maintained as its original orifice area. The same is true for case F and case G, whose taper angles are 30° and 60° , respectively. These two cases produce similar flow structure with baseline so that related contour figures are not introduced.

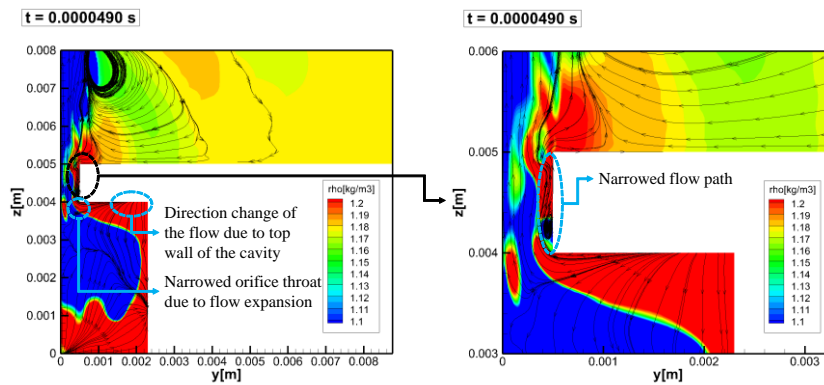
However, a totally different flow structure is formed in case D with no taper angle and case E with little taper angle as shown in Figure 6.7 (b) and (c). In Figure 6.7 (b), a portion of flow heading upward is blocked by upper cavity wall. Thus, stagnation point is formed, then the direction of the flow is changed. Not only that, flow expands when flow is turning around from upper cavity wall to orifice throat entrance. Consequently, flow path in the orifice throat is narrowed due to the expansion. Moreover, flow path is narrowed down additionally due to flow separation occurred in the orifice throat, which is also a result of flow expansion. This is shown in Figure 6.7 (c). The narrowed flow path decreases effective orifice throat area, which cause reduction in the thrust, and thus total impulse. These are the reasons for the decrease of total impulse of SparkJet actuator which has small and/or no taper angle configuration. However, the average total impulse differences between the relatively low taper angles are not explained by these reasons. Had it been only these reasons, average total impulse for 0° taper angle should be the lowest, but it is the 30° taper angle case.



(b) Smooth flow in the baseline.



(a) The stagnation point in case D.



(c) The flow expansion, stagnation point, and narrowed flow path in case D.

Figure 6.7 Effect of the taper angle on flow structure: (a) Smooth flow in the baseline, (b) the stagnation point in case D, and (c) the flow expansion, stagnation point, and narrowed flow path in case D

There is another reason for degradation in total impulse. It is the high temperature leakage throughout the orifice as shown from Figure 6.8 to Figure 6.11. They show temperature contour and streamlines for the selected cases in the order of taper angle. The high temperature flow is being expelled from cavity to orifice exit for case D with no taper angle and case E with 15° of taper angle. However, case F with 30° of taper angle and baseline with 45° of taper angle have no high temperature outflow. Even case F with 30° of taper angle also shows high temperature outflow a little bit later than the two mentioned cases. The high temperature flow is ejected approximately after $80\ \mu\text{s}$ for Case F. It belongs to region II when the primary jet generation period region I is already over. Thus the enormous portion of total impulse is already generated so that the effects of high temperature flow is relatively low for case F.

Basically, cases with relatively small taper angle such as case D and case E have small effective distance in $z - \text{axis}$ direction so that they have more chance of high temperature flow ejection. Since the high temperature flow is ejected, energy inside the cavity is not able to be trapped and maintained so that driving force for jet generation is not preserved. This can be deduced from cavity average temperature shown in Figure 6.12. Rather than comparing the absolute values due to differences in total volume of cavity, decrease rates are compared. The cavity average temperature of case E with 15° of taper angle decreases faster than case D with 0° of taper angle. It states that the high temperature for case E is ejected more, which leads to less total impulse due to the energy loss.

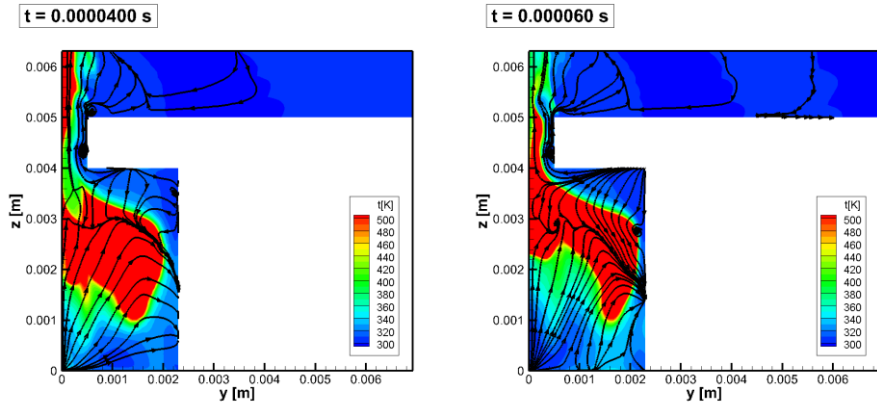


Figure 6.8 Temperature contour and streamlines of case D at 40 μ s and 60 μ s.

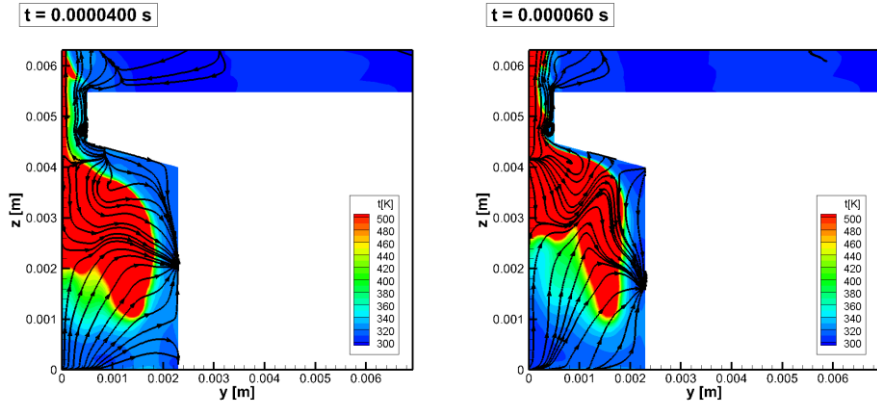


Figure 6.9 Temperature contour and streamlines of case E at 40 μ s and 60 μ s.

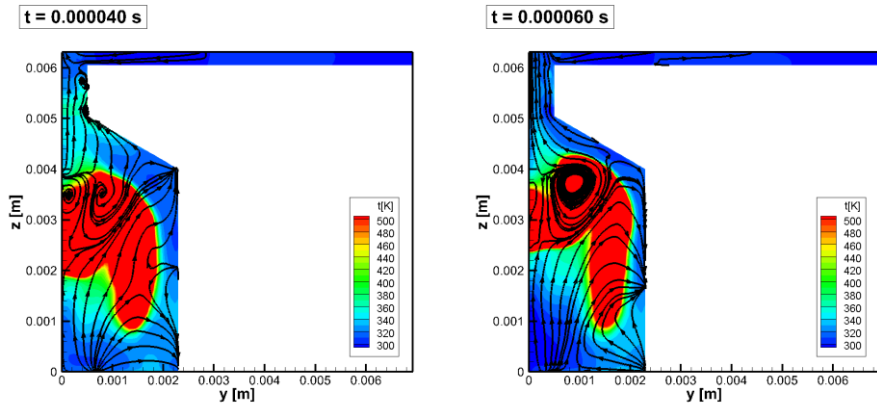


Figure 6.10 Temperature contour and streamlines of case F at 40 μ s and 60 μ s.

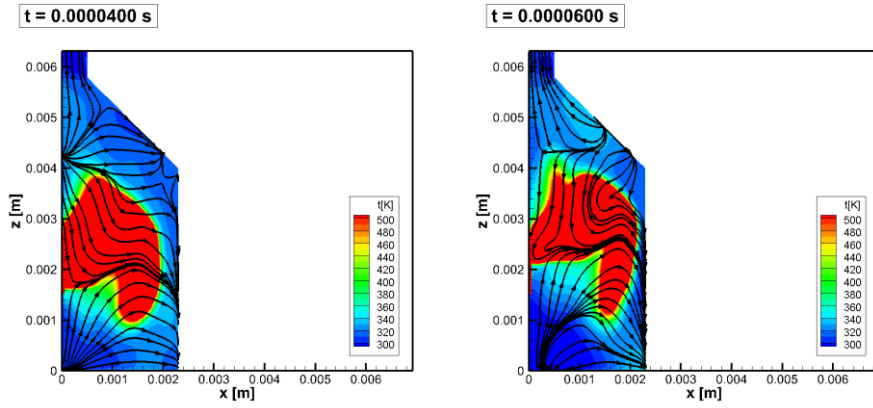


Figure 6.11 Temperature contour and streamlines of baseline at 40 μ s and 60 μ s.

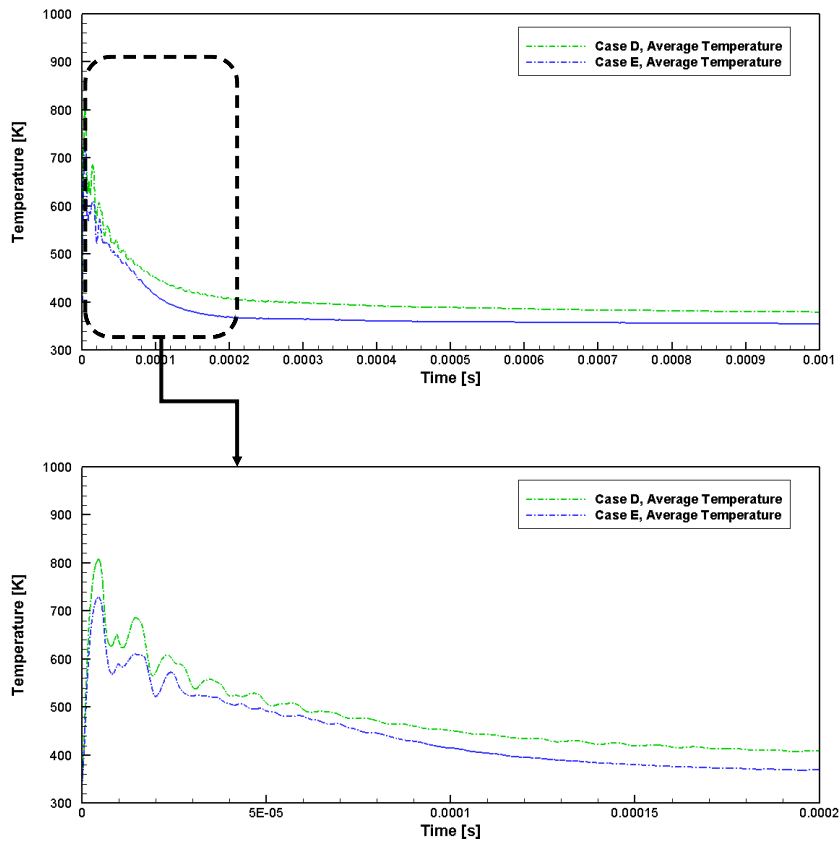


Figure 6.12 Cavity average temperature for case D and E.

The movement and ejection of high temperature flow is influenced by overall flow behavior inside the cavity, which is related to the natural frequencies of SparkJet actuator. It can be explained by considering the natural frequencies and geometry configurations together. Let the ratio of the first natural frequency f_1 to the second natural frequency f_2 (f_1/f_2) be the frequency ratio, and the ratio of length from the cavity bottom to the orifice entrance to the cavity radius (z/r) be the length ratio. These two ratios and their differences are compared. The frequency ratio indicates the ratio of propagated distance of the reflected pressure waves in the $z - axis$ direction to that of $r - axis$ direction. As this frequency ratio is close to the length ratio, the reflected pressure waves in the $z - axis$ direction propagates from the bottom of the cavity to orifice entrance when the reflected pressure waves in the $z - axis$ direction propagates from the center to the side wall of the cavity. As a result, a kind of resonance occurs between the reflected pressure waves. Then there would be two kinds of effects. The first one is very simple that the generation of pressure wave is promoted. The second one is related to the behavior of the high temperature flow. If the two reflected pressure waves are in phase, the high temperature bulk flow is able to be trapped inside the cavity for a longer time, and thus producing driving force. However, just like in case E, if they are out of phase, the movement of high temperature bulk flow is promoted. Subsequently, global convective flow towards the orifice exit is promoted at the same time since it is the only way that flow can go. Consequently, the high temperature bulk flow generated by plasma moves upward gradually.

The frequency ratios, the length ratios, and their differences for each case are listed in the Table 6.3 and graphically shown in Figure 6.13. The ratio difference of case E is less than that of case D so that the resonance is more dominate in case E,

so thus the trapping effects or the ejection effects of high temperature flow. For case E, it is the ejection effects as shown from Figure 6.14 to Figure 6.17. Each figures show velocity contour in y and z direction at the same time. The velocity in y direction heads for center of cavity. At the same time, it is the outward direction from the center of cavity for the velocity in z direction. Theses indicate that the reflected pressure wave in the $r - axis$ direction is heading inward to cavity center, meanwhile that of $z - axis$ direction is heading outward from cavity center. The two reflected pressure waves are in opposite direction with respect to cavity center so that the high temperature bulk flow is pushed upward and expelled. Again, it can be confirmed from the high temperature flow for case E is close to the upper wall of cavity compared to case D as shown in Figure 6.9 and Figure 6.8. For the quantitative analysis, additional cases are needed to be solved. The required cases should have different effective height of cavity and cavity diameter as parameters. By changing the such parameters, phase difference of reflected pressure waves inside the cavity could be achieved and quantitative data could be obtained.

Table 6.3 Frequency ratios, length ratios, and their differences.

| Cases (Taper Angle) | f_1/f_2 | z/r | $(f_1f_2)(z/r)$ (%) |
|---------------------|-----------|-------|---------------------|
| Baseline (45°) | 2.366 | 2.522 | 6.18 |
| Case D (0°) | 1.980 | 1.739 | 13.85 |
| Case E (15°) | 2.200 | 1.949 | 12.89 |
| Case F (30°) | 2.286 | 2.191 | 4.32 |
| Case G (60°) | 2.829 | 3.095 | 8.60 |

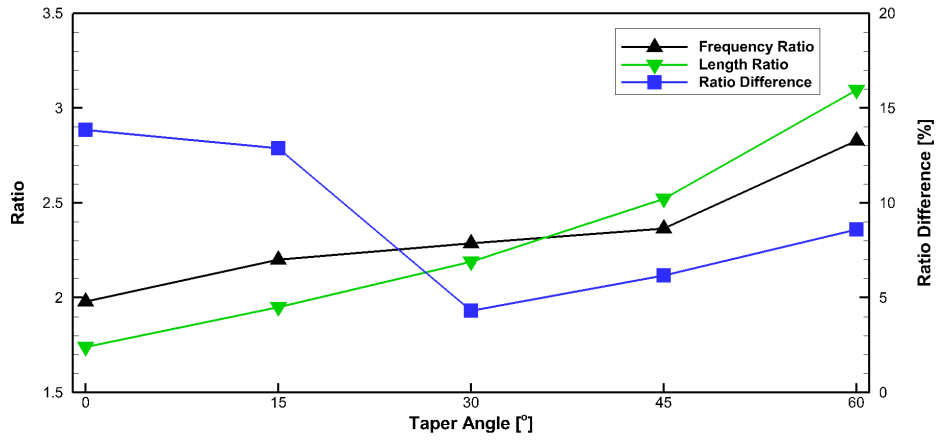


Figure 6.13 Natural frequency and lengh ratios and their differences.

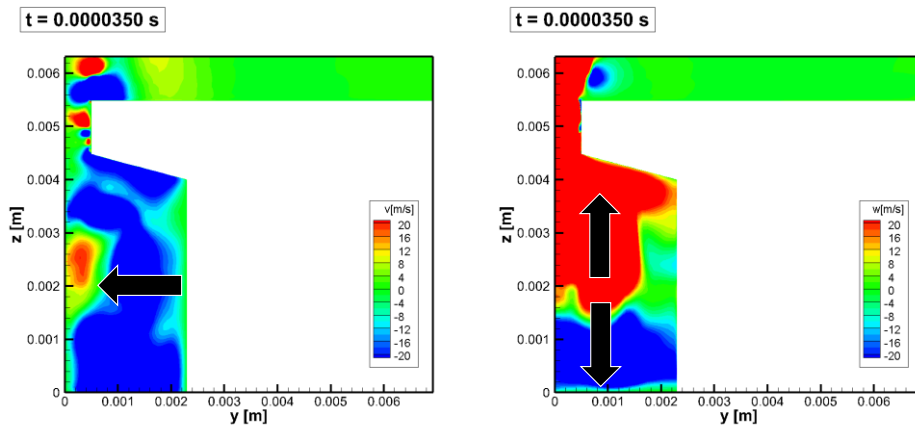


Figure 6.14 Velocity contour in y and z direction for case E at 35 μ s.

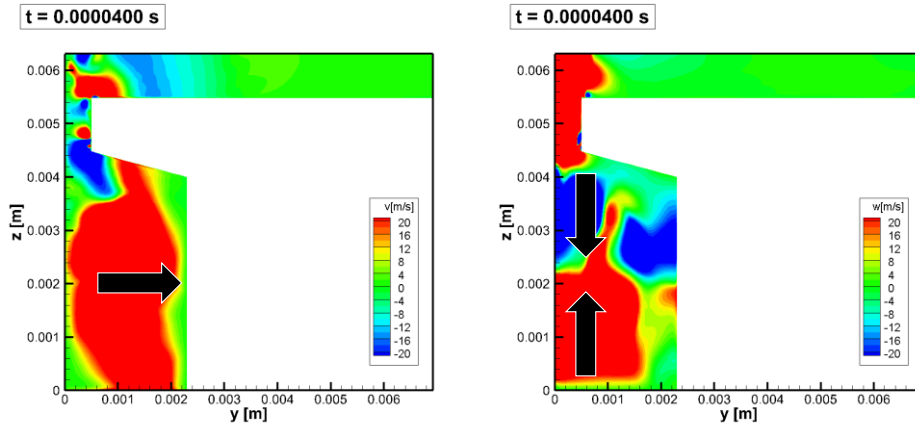


Figure 6.15 Velocity contour in y and z direction for case E at $40 \mu\text{s}$.

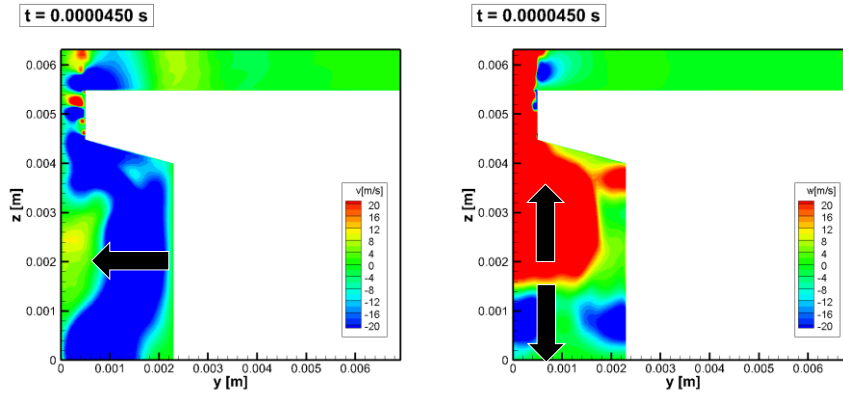


Figure 6.16 Velocity contour in y and z direction for case E at $45 \mu\text{s}$.

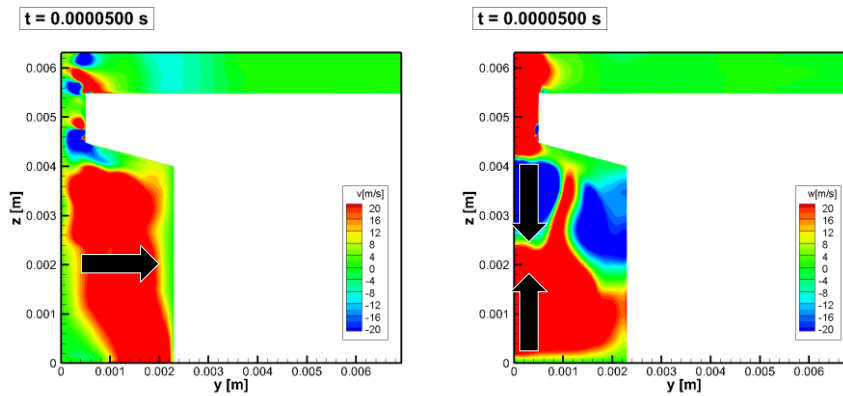


Figure 6.17 Velocity contour in y and z direction for case E at $40 \mu\text{s}$.

It is mentioned that the pressure wave generation is promoted when the resonance is occurred. It can be confirmed by comparing the pressure total impulse component and the differences of ratio as shown in Figure 6.18. The pressure total impulse is increased as the taper angle is increased from 0° to 30° and decreased as taper angle is increased from 30° to 60° . It shows maximum value at 30° of taper angle which is case F. Meanwhile, the differences of ratio is decreased as taper angle is increased from 0° to 30° , then increased as taper angle is increased from 30° to 60° . The minimum value occurred at 30° of taper angle which is case F. The lower the differences of ratio, the more resonance is occurred. Thus, the resonance is occurred liveliest in case F. As a results, additional pressure wave generation for case F is the greatest.

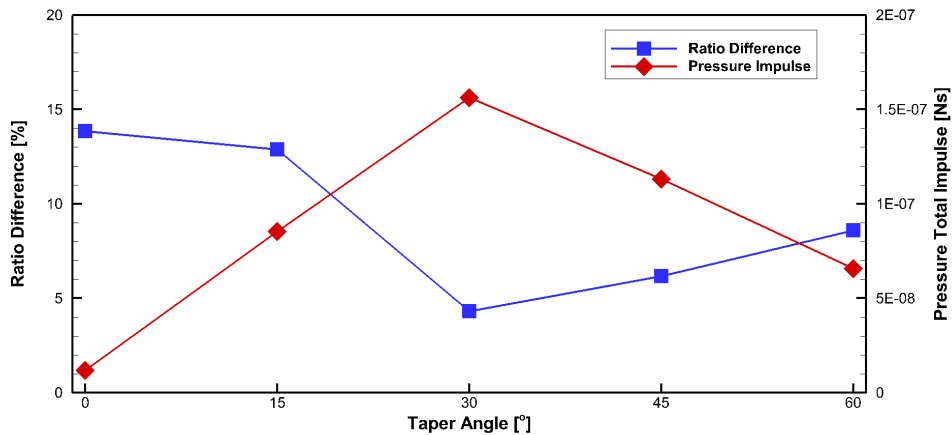


Figure 6.18 The pressure total impulse component and the differences of ratio.

Interest thing between baseline with 45° of taper angle and case G with 60° of taper angle is that, total impulse is turned over after the discharge phase as shown in Figure 6.19. Specifically, the total impulse of baseline is greater than case G before

approximately 220 μs . But after that, even though it is a very little, the total impulse is turned over and that of case G becomes greater than baseline. The thrust is terminated and oscillates around zero for both cases in the vicinity of approximately 220 μs . Meanwhile, the amplitude of the thrust oscillating around zero is larger for case G. This leads to gradual increase of the total impulse for case G, and eventually becomes larger than baseline. This is the situation that only case G shows. By comparing these two cases, the amplitude of oscillating residual thrust gets greater as the taper angle increases. As a result, total impulse slightly increases even after the thrust termination. It indicates that the difference in total impulse between the baseline and case G is not significant when only the jet generation phase is considered.

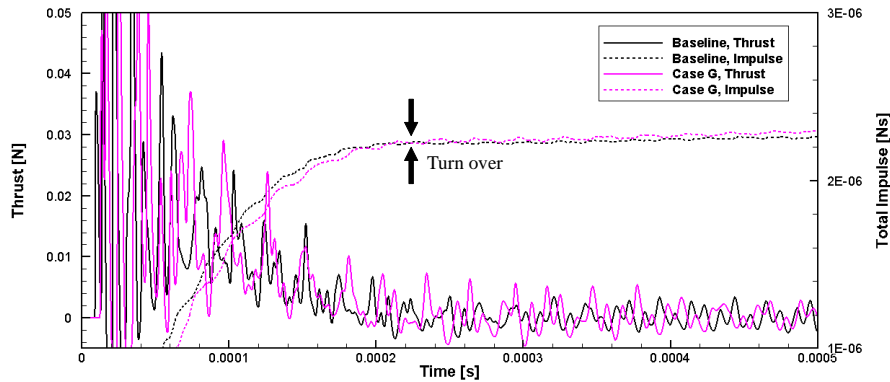


Figure 6.19 Enlarged thrust and total impulse of baseline and G.

In conclusion, taper angle affects flow structure in a variety of ways that no regular trend is found. So that every details regarding the flow structure should be considered when designing the taper angle. Some general aspects are as follows.

First, too small taper angle causes flow expansion at the entrance of the orifice

and flow separation at the wall of orifice throat. Those are the reasons for the total impulse loss. A certain degree of taper angle is required for the flow to smoothly move along the upper wall of cavity and avoid the flow expansion and separation.

Second, too small taper angle leads to small effective distance in the $z - axis$ direction so that there is chance for high temperature flow to be expelled through the orifice. Due to this phenomenon, average cavity temperature decreases faster. This is one reason for energy loss inside the cavity that leads to reduction of driving force for jet generation. The leakage of high temperature flow is influenced by the overall flow behavior inside the cavity, which is related to the frequency ratio and length ratio of the actuator. If the differences of such ratios are close to unity, there occurs resonance of reflected pressure waves inside the cavity. For the in phase resonance, the high temperature flow is trapped inside the cavity for a longer time and provide driving force. On the other hands, the out of phase resonance promotes the ejection of high temperature flow so that the performance of the actuator is degraded. Since the effective distance in the $z - axis$ direction and ratio differences are affected by combination of cavity height, taper angle, electrode shapes, and cavity diameters, many parameters should be considered regarding the high temperature outflow. Thus, the taper angle should carefully be determined with the consideration of many other design variables. Unfortunately, controlling the difference in natural frequency ratio and length ratio, especially, in advance is very complicated and difficult since the natural frequencies are function of many design variables, operational environment, and conditions.

Finally, too large taper angle leads leakage flow through the orifice which may causes net positive thrust and total impulse even after the discharge of the jet and pressure wave. This is the reason for malfunctioning beyond the design point.

6.3 Electrode Height

The third parameter for numerical analysis of performance characteristics is the electrode height. The analyzed cases are listed in Table 6.4. The electrode height is changed by 1 mm lower for case H and higher for case I compared to baseline. Their thrust and average total impulse are listed in Table 6.5, and thrust and total impulse are shown graphically in Figure 6.20. The thrust for both cases is decreased by approximately 10 %. As mentioned earlier, thrust is not an appropriate factor to compare directly due to its highly oscillating phenomena. The average total impulse for case H increased by 9.33 % and case I decreased by 9.38 %. Based on these results, the total impulse of the SparkJet actuator is reversely proportional to the electrode height up to approximately 20 %. In other words, the total impulse increases as the electrode height decreases.

Table 6.4 Design variables for performance characteristics analysis for electrode height.

| Design variables | Values | | |
|----------------------------|----------|--------|--------|
| | Baseline | Case H | Case I |
| Orifice exit diameter (mm) | 1.0 | 1.0 | 1.0 |
| Orifice throat length (mm) | 1.0 | 1.0 | 1.0 |
| Orifice taper angle (°) | 45 | 45 | 45 |
| Cavity diameter (mm) | 4.6 | 4.6 | 4.6 |
| Cavity height (mm) | 4.0 | 4.0 | 4.0 |
| Electrode height (mm) | 2.0 | 1.0 | 3.0 |
| Electrode gap (mm) | 1.2 | 1.2 | 1.2 |
| Electrode diameter (mm) | 1.0 | 1.0 | 1.0 |

Table 6.5 Thrust and average total impulse for different electrode height.

| Cases | T_{max} (N) | ΔT_{max} (%) | I_{ave} (μ Ns) | ΔI_{ave} (%) |
|----------|---------------|----------------------|-----------------------|----------------------|
| Baseline | 0.146 | ... | 2.09 | ... |
| Case H | 0.133 | −9.03 | 2.28 | 9.33 |
| Case I | 0.130 | −10.89 | 1.88 | −9.83 |

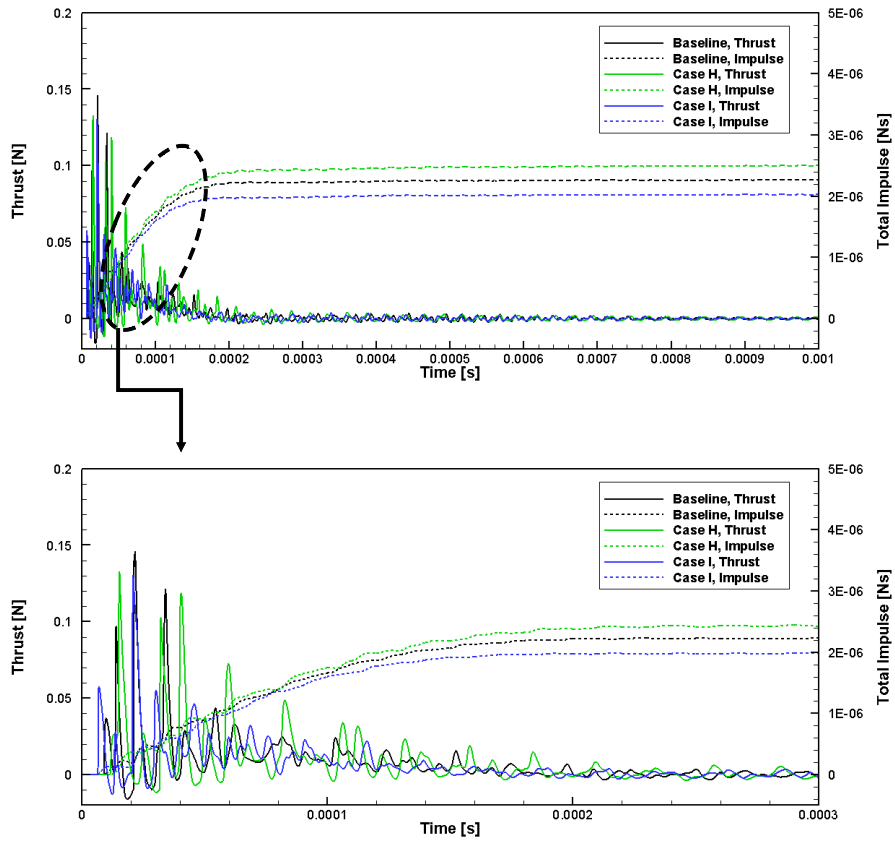


Figure 6.20 Thrust and total impulse for different electrode height.

The average pressure inside the cavity shown in Figure 6.21 shows consistent trend with total impulse. The period of nearly flat top up to approximately 30 μ s where the maximum value appears is similar between the three compared cases.

After the flat top period, the average pressure inside the cavity starts to decrease until approximately 200 μ s. This is the time when the discharge stage is finished. After the discharge stage, the cavity average pressure oscillates around atmospheric pressure, and the thrust and total impulse also show no actuations. In the decrease period of cavity average pressure, the three compared cases have different decrease rate. The magnitude of decrease rate is in the order of electrode height increase. The cavity average pressure of case I with electrode height of 3 mm decreases fastest, whose electrode is the highest among the compared cases. Baseline with electrode height of 2 mm and case H with 1 mm follow in the order.

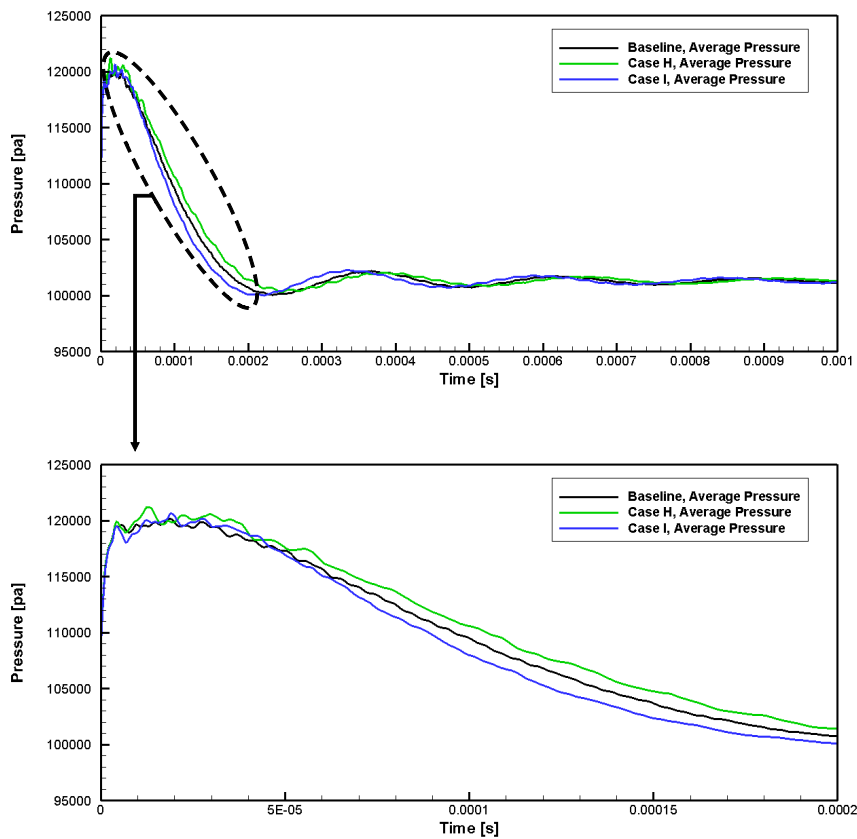


Figure 6.21 Cavity average pressure for different different electrode height.

The different flow structures inside the cavity influenced by the electrode height are able to explain the reasons for the total impulse and cavity average pressure trends. As shown in Figure 6.22 through Figure 6.24, high temperature region is remained where the electrode is positioned. Since the high temperature region of case I is located in the upper side of cavity, which is close to orifice, the high temperature flow is leaked through orifice. On the other hands, the high temperature region of case H is located in the lower side of cavity so that the energy is relatively conserved for a longer time. The cavity average pressure is remained a little bit greater due to the conserved energy. The energy is then turned into pressure.

Moreover, the high temperature flow located in the lower side of the cavity is suitable for pushing as much mass flow as possible from the bottom up. As electrode height becomes higher, the outflow of mass flow gets reduced. The momentum term component of total impulse shown in Figure 6.25 supports this. The momentum term component of total impulse for all three compared cases are at least 93 % of entire total impulse. The momentum term component of total impulse for case H is approximately 8.21 % greater, and case I is approximately 10.21 % less than that of baseline. These values are close to the differences of entire total impulse, which are 9.33 % for case H and 9.83 % for case I, respectively. Thus, it is confirmed quantitatively that the outflow of mass flow is reversely proportional to the electrode height.

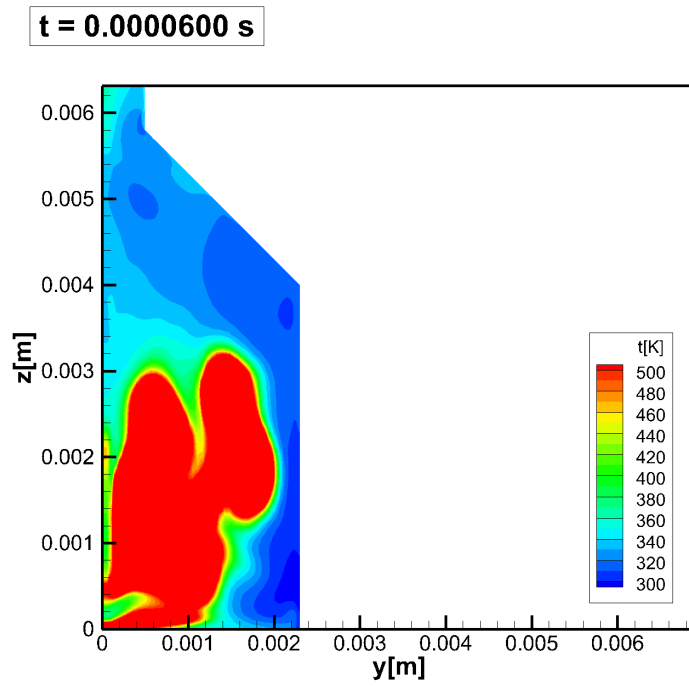


Figure 6.22 Temperature contour of case H at 60 μ s.

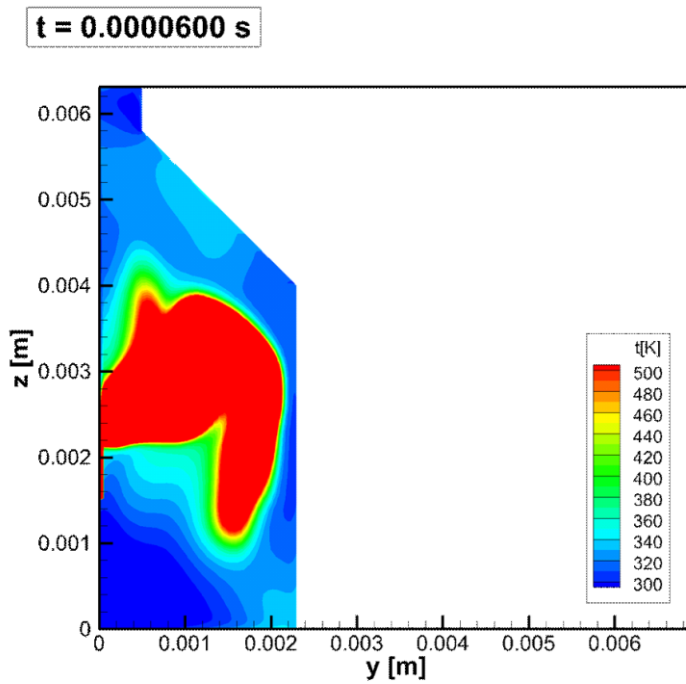


Figure 6.23 Temperature contour of baseline at 60 μ s.

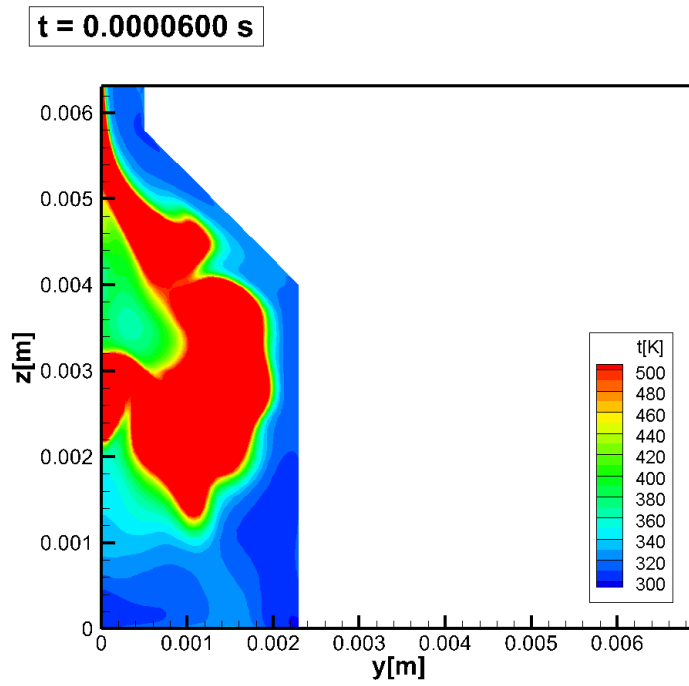


Figure 6.24 Temperature contour of case I at 60 μ s

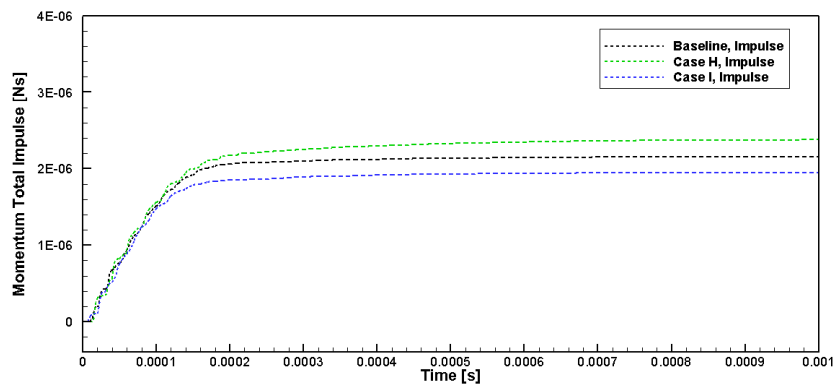


Figure 6.25 Momentum total impulse for different electrode height.

The frequency characteristics of compared cases also support the trend of mass flow outflow and present additional flow physics regarding the electrode height. The positions of the high temperature region affect the propagating directions of the reflected pressure waves. Figure 6.26 shows the Fast Fourier transform of full range thrust for the compare three cases. Baseline and case I have similar trend but not case H. The first natural frequency f_1 for case H is not developed much, rather the second natural frequency f_2 developed enormously. The FFT result of case H seems physically similar to that of case C whose reflected pressure waves in the $r - axis$ direction is disappeared during the jet discharge stage.

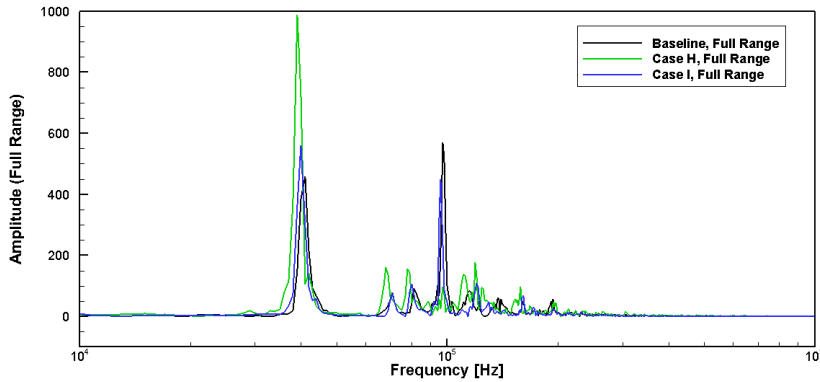


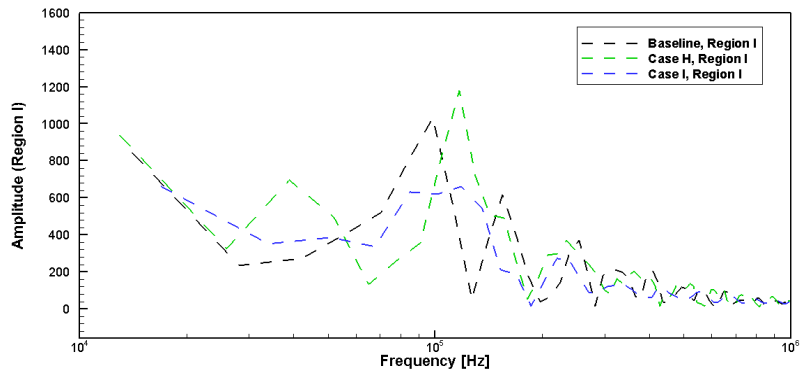
Figure 6.26 Full range Fast Fourier transform of thrust for different eletrode height.

To investigate the behavior of the reflected pressure waves in the $r - axis$ direction of case H in detail, FFT for each region is conducted and is shown in Figure 6.27. In region I, overall frequency components are arisen as usual including case H. Interest thing is that the frequency component near the second natural frequency f_2 is also distinguishable in case H, which is not able in the other cases. It states that the reflected pressure wave in the $z - axis$ direction is exceptional from the start

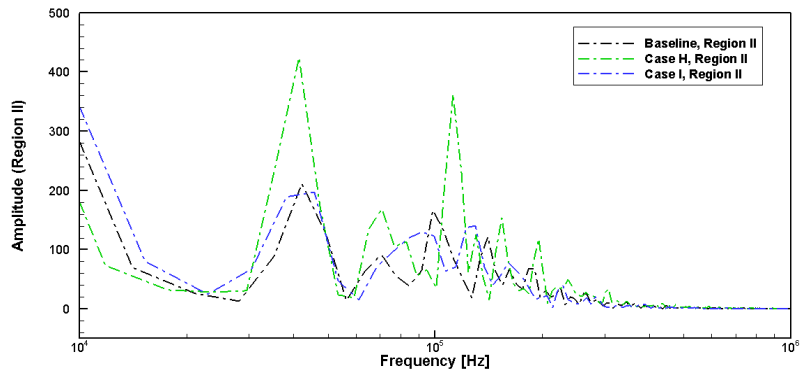
of the actuation. In region II, the peak for the first natural frequency f_1 of case H is even greater than other two cases unlike in the full range. The peak for the second natural frequency f_2 of case H is also greater than the other two just like in the full range. Case H is different from the case C whose first natural frequency f_1 is reduced in region II. It can be inferred from FFT results of region I and II that the pressure wave reflected in the $r - axis$ direction is kept generating for case H. Also in region III of case H, which is the combination of region I and II so that it represents the whole jet discharge stage, the first natural frequency f_1 is remained and the second the first natural frequency f_2 is stronger compared to the other two cases. Thus, it is confirmed that the reflected pressure waves responsible for the first natural frequency f_1 of case H is properly generated. In addition, the reflected pressure waves responsible for the second natural frequency f_2 is distinguishable from the beginning of the jet generation phase as shown in the FFT result of region I and even remained stronger than other two cases. Consequently, in combination with the full range FFT result for case H, it can be interpreted that the reflected pressure waves in the $z - axis$ direction are generated stronger compared to the other two cases, and the reflected pressure waves in the $r - axis$ direction are generated in the first place and fairly reduced. Eventual conversion of the reflected pressure wave in the $r - axis$ direction into the $z - axis$ direction is the possible so that it gets stronger. In connection with the electrode position of case H, both of the reflected pressure waves in the $r - axis$ and $z - axis$ directions are generated in the energy deposition and discharge stage. However, most of the reflected pressure waves in the $r - axis$ direction is converted into the $z - axis$ direction because the electrodes are close to the bottom wall of the cavity. The cavity average pressure remained

higher for case H as shown in Figure 6.21 supports this conversion of reflected pressure wave direction. When reflected pressure wave in the $r - axis$ direction is gathered in the center of the cavity, it should propagate outward again. For case H, however, the gathered reflected pressure wave has no option to propagate through the negative $z - axis$ direction due to the cavity wall. So that the bottom cavity wall act to increase the average pressure inside the cavity. Also the pressure wave incident on the lower wall of the cavity propagates along the $z - axis$ direction. Here, a portion of reflected pressure waves in the $r - axis$ direction that have been gather at the center of cavity and changed their direction are included. So that the overall pressure is remained higher for case H as mentioned earlier in this section. Therefore, the convective flow is concentrated to the direction toward the orifice so that the momentum loss is reduced and the total impulse is increased.

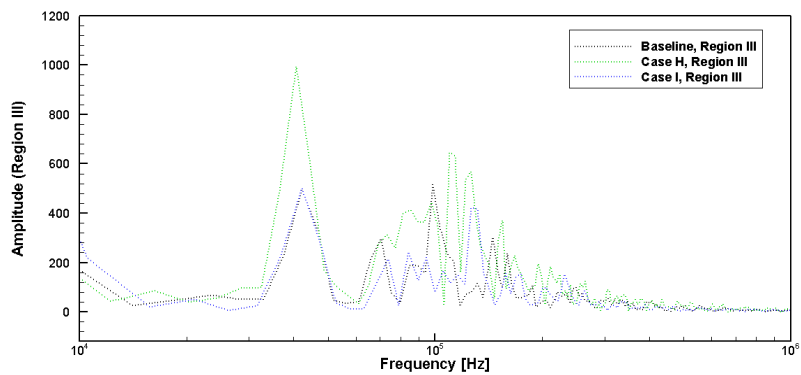
In conclusion, the electrode height affects the performance of a SparkJet actuator in two ways. First, lower electrode height forms the high temperature region lower, and thus the low density region is formed lower. This makes suitable for pushing as much mass flow as possible from the bottom up and leads to higher total impulse. Second, the reflected pressure waves in the $z - axis$ direction is promoted by the lower electrode position. In addition, the reflected pressure waves in the $r - axis$ direction is transformed into the $z - axis$ direction so that it becomes stronger to make greater total impulse.



(b) Region I.



(a) Region II.



(c) Region III.

Figure 6.27 Fast Fourier transform of thrust for different electrode height: (a) region I, (b) region II, (c) region III.

6.4 Orifice Diameter

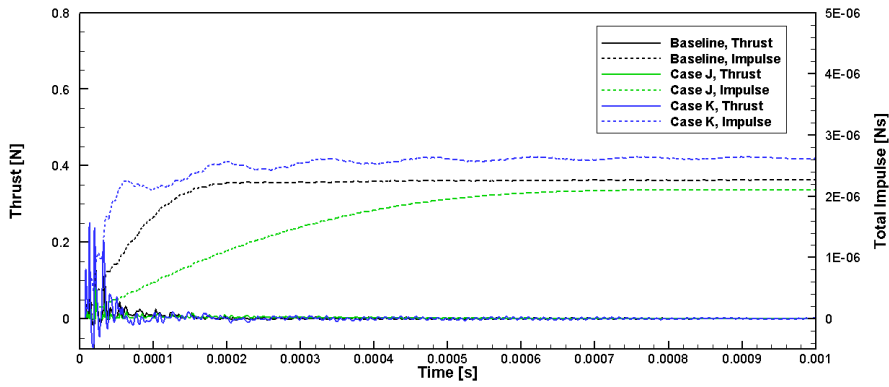
The fourth parameter for numerical analysis of performance characteristics is the orifice diameter. The analyzed cases are listed in Table 6.6. The orifice diameter is changed by twice smaller for case J and larger for case K compared to baseline. The thrust and average total impulse are listed in Table 6.7, and thrust and total impulse are shown in Figure 6.28. The thrust changed much more than other cases compared so far. The thrust for case J decreased by 43.37 % and case K increased 71.59 %. Orifice diameter of SparkJet actuator affects thrust much more than any other parameters, and therefore, the oscillation range of thrust varies the largest among other parameters. The average total impulse for case J decreased by 23.77 % and case K increased by 17.90 %. The average total impulse approximately increases 20 % when the orifice diameter doubles.

Table 6.6 Design variables for performance characteristics analysis for orifice diameter.

| Design variables | Values | | |
|----------------------------|----------|--------|--------|
| | Baseline | Case J | Case K |
| Orifice exit diameter (mm) | 1.0 | 0.5 | 2.0 |
| Orifice throat length (mm) | 1.0 | 1.0 | 1.0 |
| Orifice taper angle (°) | 45 | 45 | 45 |
| Cavity diameter (mm) | 4.6 | 4.6 | 4.6 |
| Cavity height (mm) | 4.0 | 4.0 | 4.0 |
| Electrode height (mm) | 2.0 | 2.0 | 2.0 |
| Electrode gap (mm) | 1.2 | 1.2 | 1.2 |
| Electrode diameter (mm) | 1.0 | 1.0 | 1.0 |

Table 6.7 Thrust and average total impulse for different orifice diameter.

| Cases | T_{max} (N) | ΔT_{max} (%) | I_{ave} (μ Ns) | ΔI_{ave} (%) |
|----------|---------------|----------------------|-----------------------|----------------------|
| Baseline | 0.146 | ... | 2.09 | ... |
| Case J | 0.083 | -43.37 | 1.59 | -23.77 |
| Case K | 0.251 | 71.59 | 2.46 | 17.90 |

**Figure 6.28 Thrust and total impulse for different orifice diameter.**

Most of the compared cases so far in the earlier sections have similar duration for discharge stage including baseline. It ended around 200 μ s. Detail shape of total impulse of case K is a bit different from baseline but similar in overall. The discharge stage of case K also ends around 200 μ s. However, case J has fairly long jet discharge time. The total impulse of case J reaches its maximum nearly after 700 μ s which is quite late compare to about 200 μ s for all the other cases. Because of the small orifice diameter, the area of the orifice throat is also small, so not much of the mass flow is expelled. The fact that exceptionally small increase rate of momentum term component of total impulse shown in Figure 6.29 supports the low mass flow ejection.

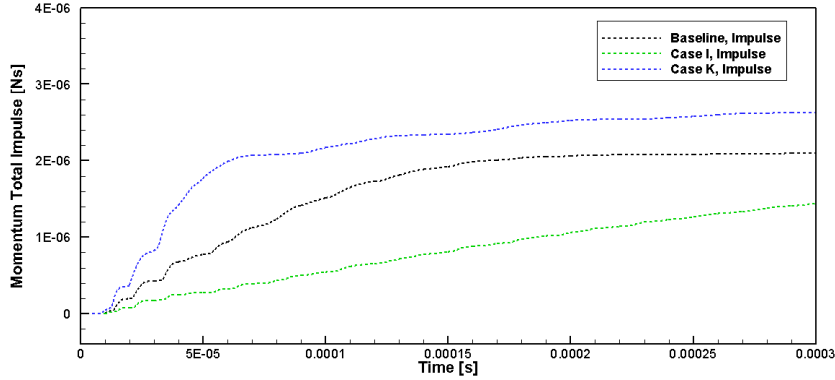


Figure 6.29 Momentum total impulse for different orifice diameter.

The average pressure inside the cavity shown in Figure 6.30 does not match with the trend of the total impulse. Case J shows greater cavity average pressure but smaller total impulse. This is because the orifice throat area is so small that mass flow of the actuator is not able to be expelled, and thus the pressure is higher and the time for pressure increase is remained longer. Unfortunately, it is not high enough to be a sonic nozzle so that the jet expelled by the actuator is remained subsonic. Meanwhile, the increase amount of cavity average pressure for the other two cases are close to each other. For baseline, the capacity for additional pressure rise and mass flow ejection seems to be similar to each other so that there exists some flat top period. Case J, which has wider orifice throat, is favorable for mass flow ejection so that the cavity average pressure drops immediately. The inflow and outflow through the orifice in the refresh stage by natural pressure differences of cavity and outside is also favorable due to its wide orifice throat area. Thus the amplitude of oscillations in cavity average pressure in the refresh stage is very large. In addition, cavity average density shown in Figure 6.31 confirms the less ejection of mass flow for case J since it decreases slower and kept higher than the other two cases.

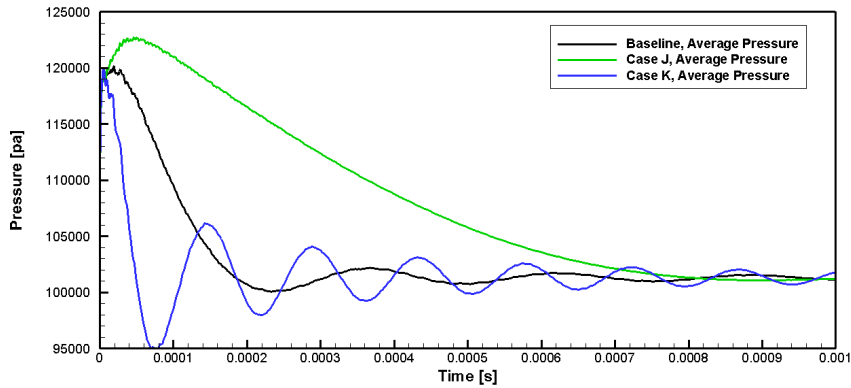


Figure 6.30 Cavity average pressure for different orifice diameter.

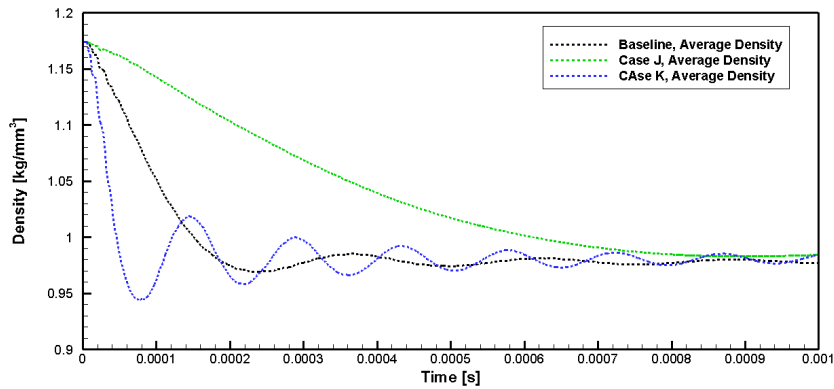


Figure 6.31 Cavity average density for different orifice diameter.

The total impulse of Case K shows a decrease in a certain period, such period as approximately from 60 μ s to 130 μ s, and from 200 μ s to 320 μ s. This is caused by relatively large pressure drop due to the pressure term component of thrust. Figure 6.32 and Figure 6.33 show thrust and total impulse of the pressure term component, respectively. Case K has large amplitude that goes negative for the thrust compared to other two cases. In the period of approximately from 60 μ s to

120 μs , negative thrust is dominant. The same is happened approximately from 200 μs to 250 μs . The pressure term component of the total impulse shows similar trend. It shows decreasing trend in the period of approximately from 60 μs to 120 μs , and from 200 μs to 260 μs . Moreover, it is net negative in the period of approximately from 90 μs and beyond. This is the reason for the decrease in the total impulse which is the reasons for the degradation of the performance.

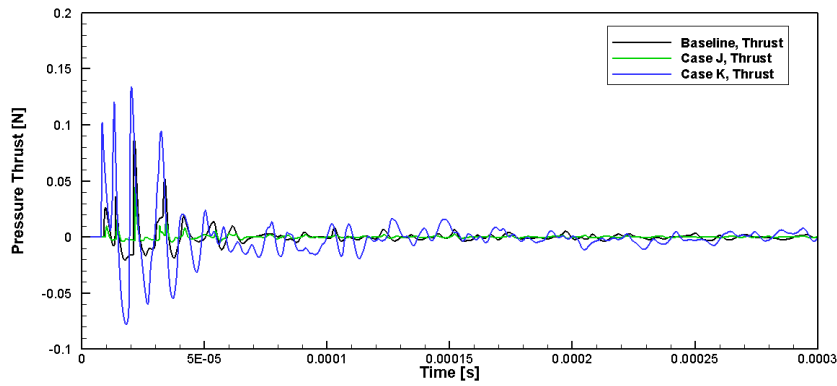


Figure 6.32 Pressure thrust for different orifice diameter.

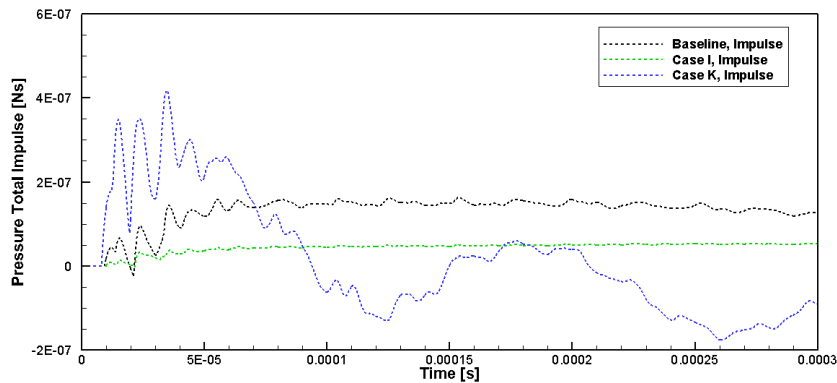


Figure 6.33 Pressure total impulse for different orifice diameter.

In conclusion, the performance of a SparkJet actuator is proportional to the orifice diameter in general. Under the same actuating environments and conditions, the total impulse performance of the actuator increases approximately 20 % by widening the orifice diameter by double due to the increase of the mass flow ejection through the orifice throat. However, widening the orifice diameter also causes more fluctuations in the pressure so that net negative thrust occurs, and thus the total impulse is degraded in some period. Meanwhile, cavity average pressure may increase by reducing the orifice diameter. However, the criteria pressure for supersonic flow is not achieved in the analyzed cases.

6.5 Summary

In this chapter, the performance of a SparkJet actuator is analyzed numerically through parametric studies as a preliminary study of the actuator design. The cavity average flow variables are examined if needed for the explanation. Basically, four parameters are selected: 1. Electrode shape, 2. Taper angle, 3. Electrode height, and 4. Orifice diameter. The parameters are selected as independent as possible between each other. Nevertheless, they are not completely independent so that only a limited selection and variation of the parameters are available. As a results, effects of each parameter on the performance of a SparkJet actuator is obtained. Based on the results, the directions on the design of a SparkJet actuator considering total impulse performance is suggested. Detailed summaries on the effects of each parameter are:

1) Electrode shape of a SparkJet actuator affects the elimination and maintenance of the reflected pressure waves in the $r - axis$ direction inside the cavity. Electrode shape changes the energy deposition region. It is the aspect ratio of energy deposition region that affects the such phenomena so that parameters such as electrode diameter, electrode gap, and cavity diameter are all related. According to the aspect ratio of energy deposition region, the reflected pressure waves in the $r - axis$ direction is generated in the first place, but it is eliminated a while after. This would reduce the total impulse performance up to approximately 3 %. The aspect ratio of energy deposition region close to unity, although not strict, is favorable for maximizing the total impulse performance. In Section 5.3, the effect of reflected pressure waves in the $r - axis$ direction is approximately 11 % of total impulse, which is quite different from 3 % in the current chapter. Effect of 3 % is the practical case, while 11 % is the ideal case. Because the 3 % of change in the

total impulse is caused by design variable change. On the other hand, the 11 % is made by the complete elimination of the oscillation by the smoothing of thrust.

2) Taper angle in the converging section of a SparkJet actuator affects the structure of outgoing flow so that the performance of the actuator is influenced. There exists three ways of effects by taper angle. First, too small taper angle causes flow expansion when the flow is going around from the upper cavity wall to orifice throat. Not only that, flow separations on orifice wall occur. These two phenomena reduce the outgoing mass flow through the orifice throat by reducing the effective orifice throat. Thus, a certain amount of taper angle is necessary to avoid the flow expansion and separation around the orifice throat. Second, too small taper angle leads to the reduction in effective height of the actuator so that it provides chance of the high temperature leakage. Such outflow degenerates the actuator performance by energy loss for driving force of the actuator. The movements of high temperature bulk flow are affected by overall flow behaviors inside the cavity. Such behaviors are enhanced by the differences of the natural frequency ratio and length ratio. If this value is close to unity, resonance of the pressure waves is occurred. The in phase resonance is suitable for trapping the high temperature flow so that the driving force is maintained. Meanwhile, the out of phase resonance pushes the high temperature flow upward and makes it to be expelled, resulting the degrades in the actuator performance. The resonance effects would be determined by the taper angle, cavity height, electrode shape, and cavity diameter. The overall influence of the flow expansion and separation, and high temperature outflow in the reduction of the average total impulse approximately 17 %. Third, too large taper angle causes leakage of mass flow even after the main discharge stage of the jet. Thus, undesirable thrust and total impulse may be generated. Consequently, an appropriate taper angle

should be found, and it is 45° based on the results of the current study.

3) Electrode height of a SparkJet actuator determines the initial location of high temperature bulk flow. This affects the directions of main convective flow. Thus, the electrode position as close as possible to the bottom cavity wall is favorable in making the upward convective flow as the sole direction, which leads to the increase in total impulse by approximately 20 %. The lowered electrode is also advantageous for converting the reflected pressure waves in the $r - axis$ direction to $z - axis$ direction. This helps upward flow direction. The electrode height as low as possible, even close to the lower cavity wall if possible, is favorable for maximizing the total impulse performance.

4) Orifice diameter of a SparkJet actuator affects the orifice throat area so that the mass flow ejection is influenced. By lengthening the orifice diameter by double, so that the orifice throat area is widened by square, total impulse is increased by approximately 20 %. However, large pressure drop by out bursting pressure wave is accompanied so that amplitude of thrust oscillation gets grown, and thus total impulse is difficult to keep constant level even after the jet discharge stage.

So far, effects of certain design parameters on the performance of SparkJet actuator are addressed and summarized. In addition, it is certain that the effects of reflected pressure wave in the $z - axis$ direction is greater than that of $r - axis$ direction. Because the reflected pressure wave in the $z - axis$ direction emphasized by the changes in the electrode height affects approximately 20 % of total impulse, while that of $r - axis$ direction, which is disappeared by the electrode shape change, affects 3 % of total impulse.

Among the analyzed parameters, orifice diameter affected the most and electrode shape affected the least for the average total impulse. Unfortunately, the

experimental points regarding the design variables are not selected by means of design of experiment (DOE) and the number of samples are too few, only twelve of those. Not only that, when one of the design variables are changes, others are fixed. Consequently, it is very limited to conduct an analysis of variance (ANOVA) to find out interactions between the variable. The reliability of surrogate model would be questionable. Instead, average total impulse of SparkJet actuator for all of the experimental points are organized in graph as shown from Figure 6.34 to Figure 6.37.

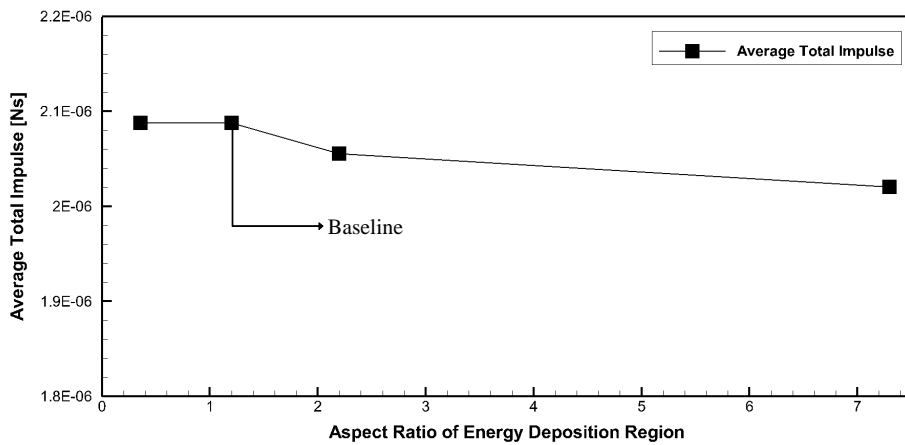


Figure 6.34 Average total impulse with respect to electrode shape.

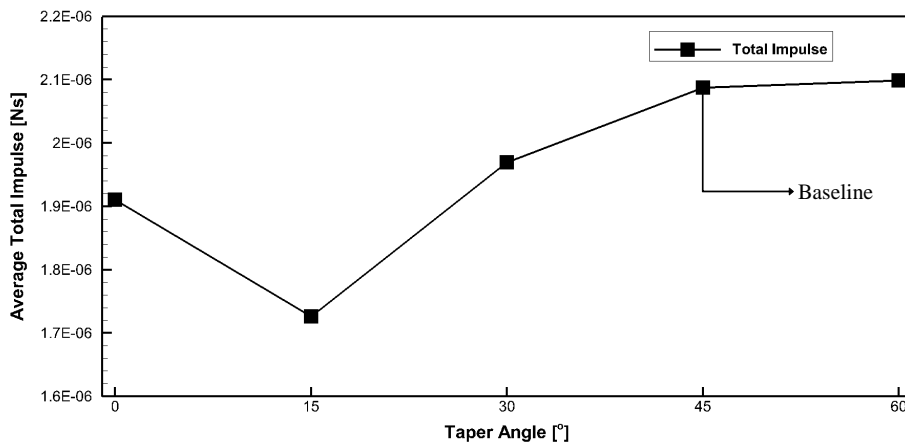


Figure 6.35 Average total impulse with respect to taper angle.

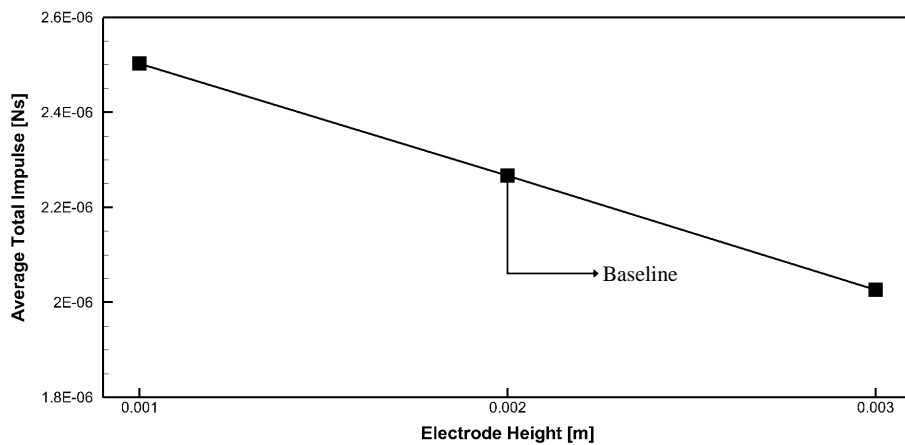


Figure 6.36 Average total impulse with respect to electrode height.

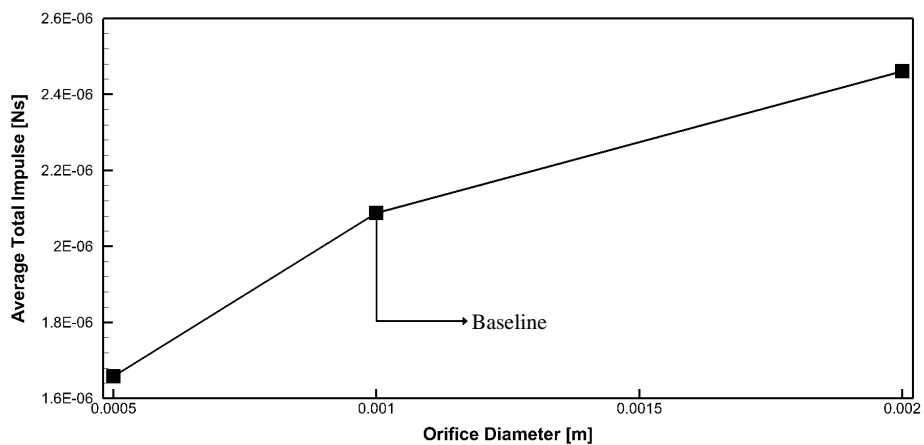


Figure 6.37 Average total impulse with respect to orifice diameter.

Chapter 7. Conclusions

7.1 Summary

SparkJet actuator is a promising active flow control device that has great potential to be used in a variety of flow regimes including high speed flow. It has been the subject of much interest for researchers in last few decades, but detailed physical phenomena of the actuator is not yet fully understood yet, and there have been no quantitative investigations for practical design.

Thus, the present study conducted numerical investigation on not only qualitative but also quantitative characterization of SparkJet actuator with the aims of understanding the physical aspects and practical design of the device. In performing numerical analyses, three dimensional unsteady Navier – Stokes solver is used. The equilibrium gas dynamics are applied in the solver to analyze SparkJet actuator which utilizes the arc plasma. In order to obtain the validity of the analysis solver, experimental results provided by ONERA and Ulsan University are used. Time history of jet front positions from the calculated results are compared with the Schlieren images from those experiments. The calculated results are in good agreement so that the validity of the solver is secured. By setting the ONERA case as a baseline model, analyses for the fundamental characteristics of SparkJet actuator are conducted. The following conclusions regarding the jet flow characteristics, performance characteristics, frequency characteristics, and pressure wave behaviors inside the cavity are drawn.

- 1) Although the flow of SparkJet actuator has some nonequilibrium effects in

the energy deposition stage, sufficient accuracy is secured by using equilibrium gas dynamics with reduced computational time consumption.

2) Pressure waves keep burst out intermittently even during the jet being ejected. These pressure waves cause oscillations in the thrust, and even negative thrust in some period. Nevertheless, the total impulse increases monotonically in overall, and converge to a certain value when thrust oscillates around zero, which can be considered as the termination of the discharge stage and actuation.

3) The discharge stage is divided into three regions based on the degree of oscillations of thrust and increase of the total impulse. The FFT results of each regions and full range of thrust revealed that the SparkJet actuator has two natural frequencies: 96.99 kHz and 40.99 kHz for baseline. The former one is named as the first natural frequency f_1 and the latter one is named as the second natural frequency f_2 .

4) The pressure wave behaviors inside the cavity confirms that the reflected pressure waves in the $r - axis$ and $z - axis$ direction are the origins of the two natural frequencies.

The following detailed conclusions are reached regarding the frequency characteristics of SparkJet actuator.

1) The first natural frequency f_1 is originated from the reflected pressure waves in the $r - axis$ direction. Meanwhile, the second natural frequency f_2 is caused by the reflected pressure waves in the $z - axis$ direction. In addition, these two natural frequencies are independent from each other, which is called the direction separable property.

2) The total impulse calculated by the thrust smoothed by each natural frequency revealed that the oscillations due to the first natural frequency f_1 affects

approximately 11 % on the average total impulse, and the overall oscillations affects approximately 15 %, ideally. Thus, it is essential to consider the oscillations of thrust to predict / estimate the performance of a SparkJet actuator.

The following conclusions are obtained regarding the performance characteristics of SparkJet actuator.

1) Electrode shape affects the average total impulse up to approximately 3 % by changing the aspect ratio of energy deposition region. Taper angle influences the average total impulse due to the flow expansion and separation around the orifice throat. Additional influences occur due to the high temperature outflow. This is occurred regarding the effective distance in $z - axis$ direction, and the differences between ratio of natural frequencies and ratio of cavity diameter to height. The overall reduction in average total impulse due to flow expansion and separation, and high temperature outflow is approximately 17 %. Electrode height acts on the average total impulse up to approximately 20 % The changes are caused by the location of high temperature bulk flow and the convert of reflected pressure wave from the $r - axis$ directions to $z - axis$ direction. Orifice diameter affects average total impulse up to approximately 40 % by varying the orifice throat area so that the outflow of mass flow is changed.

2) The effects on the total impulse of SparkJet actuator is greater for the reflected pressure wave in the $z - axis$ direction compared to that of $r - axis$ direction. Practically, the reflected pressure wave in the $z - axis$ direction affects up to approximately 20 % of total impulse, while the reflected pressure wave in the $r - axis$ direction affects up to approximately 3 %.

3) Based on the SparkJet actuator of the current baseline model used in this

study, the followings are major ways to increase performance, focused on the total impulse. First, determine the electrode diameter, electrode gap, and cavity diameter which make the aspect ratio of the energy deposition region close to unity. Second, 45° of taper angle is appropriate to minimize the performance loss caused by the flow structure changes near the upper cavity wall and orifice entrance. Also, high temperature outflow would not be occurred which is another reason of degrade of performance. Third, it is best for the electrode height to be as low as possible so that it is very close to the cavity bottom wall. Fourth, orifice diameter should be somewhere between the 1 mm and 2 mm, in order not to have oscillations in the total impulse and maximize it at the same time.

These conclusions help understanding the physical phenomena of a SparkJet actuator and provide practical considerations on the design of it.

7.2 Contribution

In the last section, the results of current study are summarized. They are contributed to the investigations of SparkJet actuator regarding the flow characteristics and natural frequencies, and actual design parameters to maximize the performance quantitatively. Especially, investigations regarding the flow characteristics and natural frequencies greatly contributed to the development of analyzing model for SparkJet actuator.

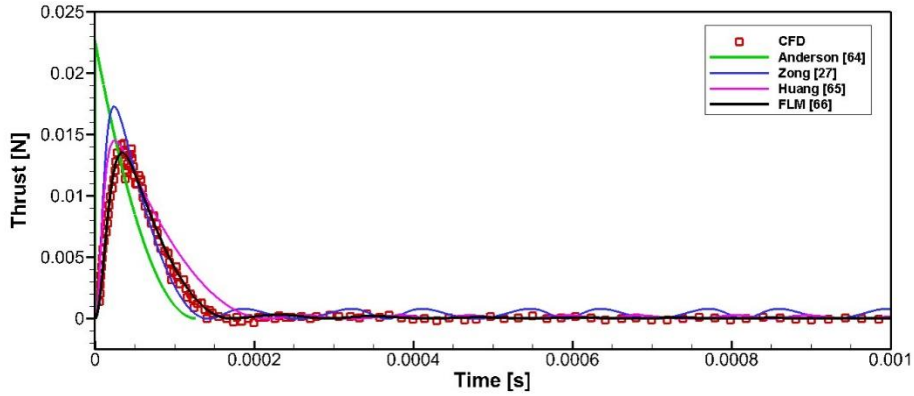
It is essential to develop accurate model for SparkJet actuator for the further investigations for two reasons. First, for the rapid and accurate predictions and/or estimation of the flow characteristics and performances of SparkJet actuator, such as velocity, thrust, and impulse of ejecting jet flow. Particularly, total impulse is a key quantitative performance factor to estimate the influence of the actuator to the external flow field. In this sense, an analytic model significantly reduces expense, time costs, and man power for the draft design and manufacturing of SparkJet actuator. Second, for the extraction of the physical boundary condition at the orifice of the actuator. It is going to be applied as the Dirichlet boundary condition in the CFD analysis. This coupling of model and CFD greatly reduces the computational cost and estimate overall performance and influence of SparkJet actuator when applied on a practical aircraft

In fact, there already are a couple of reports regarding the analyzing models as mentioned in the Sec 1.2. To list some; Popkin's model [18, 19], Anderson's model [65], Zong's model [27], and Huang's model [66]. The names of the models are denoted after the author of related paper. They all used the three – stage operation mechanism to model the actuator. The actuator is spatially averaged so that the

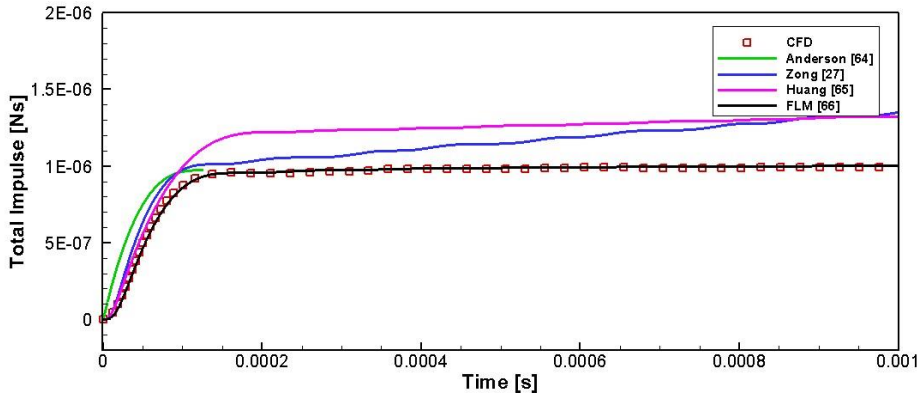
governing equation is assumed to be ODE as a function of time, which leads to zero dimensional model. Each model was developed to compensate the weaknesses of the previous models. Conclusively, however, all the models cannot overcome the three major limitations. First, failed to accurately predict the discharge time, and thus the start of the refresh stage. Second, failed to guarantee the universality to be applied to various of geometry. Third, failed to capture the oscillations caused by the reflects of pressure wave inside the cavity. Especially, the third one is the biggest and the most important cause of all the weaknesses and limitations and of the existing model. In this study, the consideration of reflected pressure waves inside the cavity is revealed to be essential for SparkJet actuator. It is the weaknesses and limitations that arisen from missing this fact.

As a result of the current study, the importance of oscillations of pressure waves and direction separable property greatly contributed to the development of an analytic model for SparkJet actuator that fairly overcome the limitations of other models, and it is still ongoing. The developing model consists of two models; the filtered line model (FLM) [67] and the oscillation model (OM). The FLM is already developed. It considers the pressure wave propagating in the $z - axis$ direction. The numerical fluxes between the cavity and orifice, and orifice and external field are defined to consider upwind concepts and wave interactions. Detailed derivations and descriptions are beyond the scope of the current study so that they are omitted. The thrust and total impulse calculated by CFD, the previous models, and the FLM are compared in the Figure 7.1. In order to possibly eliminate the reflected pressure waves in the $r - axis$ direction, the energy is deposited in the entire area of the cavity evenly. The results of the FLM is in good agreement with those of CFD, and are more accurate than other models. Consequently, the prediction and / or estimation

of the actuator performance, and design of the actuator is greatly improved by the FLM.



(a) Thrust comparison between SparkJet actuator analysis models and CFD.



(b) Total impulse comparison between SparkJet actuator analysis models and CFD.

Figure 7.1 Comparison of performance between the models and CFD.

To couple the analysis model and flow analysis, velocity at orifice exit is needed and it is shown in Figure 7.2. The result of FLM is in good agreement with CFD results compared to other model. Using the FLM results as boundary condition of CFD, the accuracy of analysis for the flow control authority of the actuator would be

greatly improved. However, extensions and progresses are required.

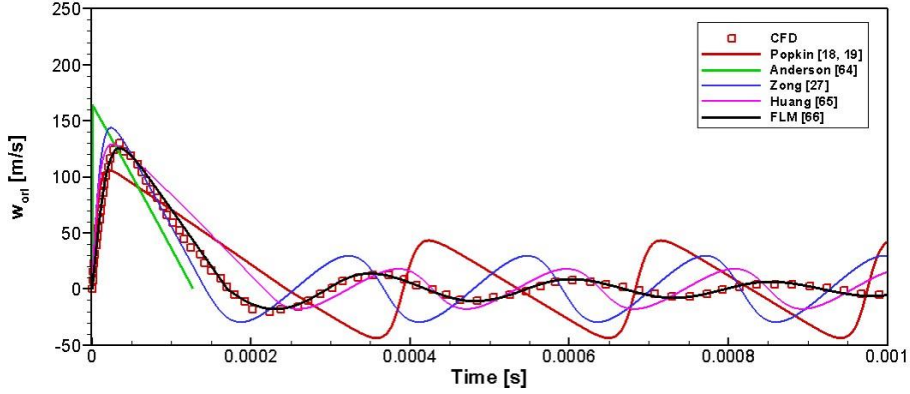


Figure 7.2 Comparison of velocity at orifice exit between the models and CFD.

The OM which considers the pressure wave propagating in the $r - axis$ direction is now under development. With the combination of the FLM and OM, it will become a full analytic model for SparkJet actuator. The combined model will provide the accurate physical values at the orifice exit that can be used as a boundary condition for CFD analysis. Such boundary condition and CFD analysis will contribute to the research on practical application of the actuator on the flow control, including supersonic regime.

Considering the reflected pressure waves into account of model development is a great contribution of the current paper. The importance of reflected pressure waves in the view of performance of SparkJet actuator is firstly presented by the current paper. Moreover, considering the reflected pressure waves separately, named direction separable property, based on their directions, $r - axis$ and $z - axis$ direction, is another great contribution of the current paper. The two separate models complete the analytic model as a one.

7.3 Future Works

In this study, fundamental physical phenomena of a SparkJet actuator is investigated numerically. Also, its frequency and performance characteristics are analyzed both quantitatively and qualitatively. Practical ways to improve the performance of the actuator are suggested thereafter. For detailed and further investigations of SparkJet actuator, some additional works are required.

First, for more detailed and extremely accurate analysis of the actuator, plasma chemical reactions, radiation energy transfer, and heat transfer through the cavity wall should be considered. These are the things that are related to the energy gain and loss that affect the temperature inside the cavity. Plasma chemical reactions and radiation energy transfer are needed for the consideration of nonequilibrium property arisen from plasma which affect the energy used in increasing the temperature of flow. With these aspects included, more detailed investigations on the energy deposition stage is possible without using the energy transfer efficiency η . This factor contains some uncertainties, and thus difficult to be determined. Sometimes it requires trial and error for the determinations of the factor. In addition, wrong estimation of the factor would lead to the over or under prediction of the performance of a SparkJet actuator. With the implementation of nonequilibrium plasma physics into the numerical solver, these kinds of uncertainties would be removed and more physically detail and accurate analysis is possible. Heat transfer through the cavity wall, including the electrodes, is needed for the accurate calculation of temperature inside the cavity especially for the repetitive operation of the actuator. The cavity flow with increased temperature might loss driving force of the actuator through heat transfer to cavity wall so that the jet momentum might be weakened. A single

operation might be excused, but not repetitive operation. There also might be an error when the high temperature region is closed to wall. From the second actuation, there certainly is chance that the temperature inside the cavity is higher than the very first actuation so that accurate calculation of temperature is required. Thus, calculation with constant surface temperature is going to be conducted as a future work.

Second, additional parameters which are not examined in the current study should be considered on their effects on the actuator performance for the better understanding of design points. Such parameters are cavity height, cavity diameter, orifice throat height, and so on. Also, effects of ratio parameters and complex parameters mentioned in the current study should be confirmed by actual calculations. Such as electrode gap to cavity diameter, electrode diameter to cavity diameter, and effective height determined by cavity height and taper angle belong them. Some of these parameters change electrode shape, ratio difference, and the sizes and total volume of cavity. They might affect the flow structures and behaviors inside the cavity. Some of them affects resonance effects, while some others affect the dissipation, so that performance of the actuator is influenced. These would help understanding the effects of parameters. For the detailed study, however, obtaining many more additional experimental points through DOE is needed. In this way, parametric interaction effects are able to be confirmed throughout ANOVA. Furthermore, optimal design through construction of surrogate model can be conducted. Also, generalized equation for SparkJet actuator performance described by normalized parameters can be expected. During the analyses according to such parameter changes, especially for the effective cavity height and cavity diameter, quantitative data could be obtained which might clarify the in phase / out of phase behavior of reflected pressure wave inside the cavity. Moreover, studies regarding

the waveforms of plasma generating power source are needed for the additional and detailed studies on the performance and optimization of SparkJet actuator. To this end, experimental studies are also needed with the combination of computational studies.

Lastly, which also mentioned in Sec. 7.2. since a huge amount of computational time is required due to three dimensional unsteady calculations, a simplified analyzing model of SparkJet actuator should be developed. There already exists some of works regarding it by other researchers [18, 19, 27, 65, 66]. Also, related works are done as a contribution of the current work with some progression over other research [67, 68]. Additional development is being done at present. The novel model is expected to reflect as many design variable as possible with the proper consideration of detailed physics of the actuator so that oscillating phenomena is well simulated. Thus, the prediction and estimation of characteristics of a SparkJet actuator including the natural frequencies, thrust, and total impulse are possible. The model to be developed can be used in designing the actuator, and analyzing the actual flow control authority of the actuator by deriving flow variables at the orifice exit then applying them as boundary conditions for CFD analyses.

Reference

- [1] Gad-el-Hak, M. Flow control: passive, active, and reactive flow management: Cambridge university press, 2007.
- [2] Reitz, J. R., Milford, F. J., and Christy, R. W. Foundations of Electromagnetic Theory: Addison-Wesley Publishing Company, 1993.
- [3] Cheng, D. K. Field and Wave Electromagnetics: Addison-Wesley, 1989.
- [4] Narayanaswamy, V., Raja, L. L., and Clemens, N. T. "Characterization of a High-Frequency Pulsed-Plasma Jet Actuator for Supersonic Flow Control," Aiaa Journal Vol. 48, No. 2, 2010, pp. 297-305.
- [5] Falempin, F., Firsov, A. A., Yarantsev, D. A., Goldfeld, M. A., Timofeev, K., and Leonov, S. B. "Plasma control of shock wave configuration in off-design mode of $M=2$ inlet," Experiments in Fluids Vol. 56, No. 3, 2015, p. 54.
- [6] Nishihara, M., Takashima, K., Rich, J., and Adamovich, I. "Mach 5 bow shock control by a nanosecond pulse surface dielectric barrier discharge," Physics of Fluids Vol. 23, No. 6, 2011, p. 066101.
- [7] Greene, B. R., Clemens, N. T., Magari, P., and Micka, D. "Control of mean separation in shock boundary layer interaction using pulsed plasma jets," Shock Waves Vol. 25, No. 5, 2015, pp. 495-505.
- [8] Roth, J. R. "Aerodynamic flow acceleration using paraelectric and peristaltic electrohydrodynamic effects of a one atmosphere uniform glow discharge plasma," Physics of plasmas Vol. 10, No. 5, 2003, pp. 2117-2126.
- [9] Saddoughi, S., Bennett, G., Boespflug, M., Puterbaugh, S., and Wadia, A. "Experimental investigation of tip clearance flow in a transonic compressor with and without plasma actuators," Journal of Turbomachinery Vol. 137, No. 4, 2015.
- [10] Narayanaswamy, V., Raja, L. L., and Clemens, N. T. "Control of a Shock/Boundary-Layer Interaction by Using a Pulsed-Plasma Jet Actuator," Aiaa Journal Vol. 50, No. 1, 2012, pp. 246-249.
- [11] Wang, L., Xia, Z.-x., Luo, Z.-b., and Chen, J. "Three-electrode plasma synthetic jet actuator for high-speed flow control," AIAA journal Vol. 52, No. 4, 2014, pp. 879-882.
- [12] Zong, H., and Kotsonis, M. "Characterisation of plasma synthetic jet actuators in quiescent flow," Journal of Physics D: Applied Physics Vol. 49, No. 33, 2016.

- [13] Zhang, Y.-c., Tan, H.-j., Huang, H.-x., Sun, S., He, X.-m., Cheng, L., and Zhuang, Y. "Transient Flow Patterns of Multiple Plasma Synthetic Jets Under Different Ambient Pressures," *Flow, Turbulence and Combustion*, 2018, pp. 741–757.
- [14] Emerick, T., Ali, M. Y., Foster, C., Alvi, F. S., and Popkin, S. "SparkJet characterizations in quiescent and supersonic flowfields," *Experiments in Fluids* Vol. 55, No. 12, 2014, pp. 1-21.
- [15] Grossman, K. R., Cybyk, B. Z., and VanWie, D. M. "Sparkjet actuators for flow control," 41st Aerospace Sciences Meeting and Exhibit. 2003.
- [16] Grossman, K., Cybyk, B., and VanWie, D. "Sparkjet actuator." Google Patents, 2004.
- [17] Ko, H. S., Haack, S. J., Land, H. B., Cybyk, B., Katz, J., and Kim, H. J. "Analysis of flow distribution from high-speed flow actuator using particle image velocimetry and digital speckle tomography," *Flow Measurement and Instrumentation* Vol. 21, No. 4, 2010, pp. 443-453.
- [18] Haack, S., Taylor, T., Emhoff, J., and Cybyk, B. "Development of an analytical sparkjet model," 5th Flow Control Conference. 2010, p. 4979.
- [19] Popkin, S. H. "One-dimensional analytical model development of a plasma-based actuator." Vol. Doctor of Philosophy, University of Maryland, 2014.
- [20] Caruana, D., Barricau, P., and Hardy, P. "The" Plasma Synthetic Jet" Actuator. Aero-thermodynamic Characterization and First Flow Control Applications," 47th AIAA aerospace sciences meeting including the new horizons forum and aerospace exposition. 2009, p. 1307.
- [21] Belinger, A., Hardy, P., Barricau, P., Cambronne, J. P., and Caruana, D. "Influence of the energy dissipation rate in the discharge of a plasma synthetic jet actuator," *Journal of Physics D: Applied Physics* Vol. 44, No. 36, 2011, p. 365201.
- [22] Dufour, G., Hardy, P., Quint, G., and Rogier, F. "Physics and models for plasma synthetic jets," *International Journal of Aerodynamics* Vol. 3, No. 1-2-3, 2013, pp. 47-70.
- [23] Laurendeau, F., Chedevergne, F., and Casalis, G. "Transient ejection phase modeling of a Plasma Synthetic Jet actuator," *Physics of Fluids* Vol. 26, No. 12, 2014, p. 125101.
- [24] Narayanaswamy, V., Raja, L. L., and Clemens, N. T. "Control of unsteadiness

- of a shock wave/turbulent boundary layer interaction by using a pulsed-plasma-jet actuator," *Physics of Fluids* Vol. 24, No. 7, 2012, p. 076101.
- [25] Zong, H.-h., Cui, W., Wu, Y., Zhang, Z.-b., Liang, H., Jia, M., and Li, Y.-h. "Influence of capacitor energy on performance of a three-electrode plasma synthetic jet actuator," *Sensors and Actuators A: Physical* Vol. 222, 2015, pp. 114-121.
- [26] Zong, H.-h., Wu, Y., Jia, M., Song, H.-m., Liang, H., Li, Y.-h., and Zhang, Z.-b. "Influence of geometrical parameters on performance of plasma synthetic jet actuator," *Journal of Physics D: Applied Physics* Vol. 49, No. 2, 2015, p. 025504.
- [27] Zong, H.-h., Wu, Y., Li, Y.-h., Song, H.-m., Zhang, Z.-b., and Jia, M. "Analytic model and frequency characteristics of plasma synthetic jet actuator," *Physics of fluids* Vol. 27, No. 2, 2015, p. 027105.
- [28] Zong, H., and Kotsonis, M. "Interaction between plasma synthetic jet and subsonic turbulent boundary layer," *Physics of Fluids* Vol. 29, No. 4, 2017, p. 045104.
- [29] Zong, H., and Kotsonis, M. "Formation, evolution and scaling of plasma synthetic jets," *Journal of Fluid Mechanics* Vol. 837, 2018, pp. 147-181.
- [30] Zong, H., and Kotsonis, M. "Effect of velocity ratio on the interaction between plasma synthetic jets and turbulent cross-flow," *Journal of Fluid Mechanics* Vol. 865, 2019, pp. 928-962.
- [31] Hoffmann, K. A., and Chiang, S. T. *Computational fluid dynamics volume I*, 2000.
- [32] Hoffmann, K. A., and Chiang, S. T. *Computational fluid dynamics volume II*, 2000.
- [33] Hoffmann, K. A., and Chiang, S. T. *Computational fluid dynamics. Volume III*, 2000.
- [34] Pletcher, R. H., Tannehill, J. C., and Anderson, D. *Computational fluid mechanics and heat transfer*: CRC press, 2012.
- [35] Toro, E. F. *Riemann solvers and numerical methods for fluid dynamics: a practical introduction*: Springer Science & Business Media, 2013.
- [36] White, F. M. *Fluid Mechanics*: McGraw-Hill, 2011.
- [37] Anderson, J. D. *Fundamentals of Aerodynamics*: McGraw-Hill Higher Education, 2007.

- [38] 노오현. 압축성 유체 유동: 박영사, 2004.
- [39] 노오현. 점성유동이론: 박영사, 2007.
- [40] White, F. M., and Corfield, I. Viscous fluid flow: McGraw-Hill New York, 2006.
- [41] Chen, F. F. Introduction to Plasma Physics and Controlled Fusion: Springer, 1984.
- [42] Lieberman, M. A., and Lichtenberg, A. J. Principles of Plasma Discharges and Materials Processing: Wiley, 2005.
- [43] Raizer, Y. P., Kisin, V. I., and Allen, J. E. Gas Discharge Physics: Springer Berlin Heidelberg, 1997.
- [44] Raizer, Y. P. Spark Discharge: CRC Press, 2017.
- [45] Anderson, J. D. Hypersonic and High Temperature Gas Dynamics: McGraw-Hill, 1989.
- [46] Fauchais, P. "Plasmas thermiques: aspects fondamentaux," Techniques de l'ingénieur. Génie électrique Vol. 3, No. D2810, 2005.
- [47] Gordon, S., and McBride, B. J. "Computer program for calculation of complex chemical equilibrium compositions and applications. I: Analysis," NASA Reference Publication. Vol. 1311, NASA Lewis Research Center, 1994.
- [48] McBride, B. J., and Gordon, S. "Computer Program for Calculation of Complex Chemical Equilibrium Compositions and Applications II: Users Manual and Program Description. 2; Users Manual and Program Description," NASA Reference Publication. Vol. 1311, NASA Lewis Research Center, 1996.
- [49] Popkin, S. H., Cybyk, B. Z., Foster, C. H., and Alvi, F. S. "Experimental Estimation of SparkJet Efficiency," Aiaa Journal Vol. 54, No. 6, 2016, pp. 1831-1845.
- [50] Park, J. H., Kim, K. H., Yeo, C. H., and Kim, H. K. "CFD analysis of arc-flow interaction in a high-voltage gas circuit breaker using an overset method," IEEE Transactions on Plasma Science Vol. 42, No. 1, 2013, pp. 175-184.
- [51] Kim, K. H., Kim, C., and Rho, O.-H. "Methods for the Accurate Computations of Hypersonic Flows I. AUSMPW+ Scheme," Journal of Computational Physics Vol. 174, No. 1, 2001, pp. 38-80.
- [52] Roe, P. L. "Characteristic-based schemes for the Euler equations," Annual review of fluid mechanics Vol. 18, No. 1, 1986, pp. 337-365.
- [53] Shu, C.-W., and Osher, S. "Efficient implementation of essentially non-

- oscillatory shock-capturing schemes," *Journal of Computational Physics* Vol. 77, No. 2, 1988, pp. 439-471.
- [54] Shu, C.-W., and Osher, S. "Efficient implementation of essentially non-oscillatory shock-capturing schemes, II," *Journal of Computational Physics* Vol. 83, No. 1, 1989, pp. 32-78.
- [55] Gottlieb, S., and Shu, C.-W. "Total variation diminishing Runge-Kutta schemes," *Mathematics of computation of the American Mathematical Society* Vol. 67, No. 221, 1998, pp. 73-85.
- [56] Cooley, J. W., and Tukey, J. W. "An algorithm for the machine calculation of complex Fourier series," *Mathematics of computation* Vol. 19, No. 90, 1965, pp. 297-301.
- [57] Kreyszig, E. *Advanced Engineering Mathematics*: John Wiley & Sons, 2010.
- [58] Ramirez, R. W. *The FFT fundamentals and concepts*: Prentice-Hall, Inc., 1985.
- [59] Harris, F. J. "On the use of windows for harmonic analysis with the discrete Fourier transform," *Proceedings of the IEEE* Vol. 66, No. 1, 1978, pp. 51-83.
- [60] Kim, H.-J., Shin, J. Y., Chae, J., Ahn, S., and Kim, K. H. "Research on Flow Analysis Program Development Considering Equilibrium Plasma Flow and Impulse Characterization of Sparkjet Actuator," *Journal of The Korean Society for Aeronautical and Space Sciences* Vol. 47, No. 2, 2019, pp. 90-97.
- [61] Kim, H.-J., Shin, J. Y., Chae, J., Ahn, S., and Kim, K. H. "Numerical investigation on jet characteristics and performance of SparkJet actuator based on pressure wave behavior inside a cavity," *AIP Advances* Vol. 10, No. 3, 2020, p. 035024.
- [62] Belinger, A., Naudé, N., Cambronne, J., and Caruana, D. "Plasma synthetic jet actuator: electrical and optical analysis of the discharge," *Journal of Physics D: Applied Physics* Vol. 47, No. 34, 2014, p. 345202.
- [63] Kim, Y. S., and Shin, J. "Performance Characteristics of a High-Speed Jet Produced by a Pulsed-Arc Spark Jet Plasma Actuator," *Journal of the Korean Society for Aeronautical & Space Sciences* Vol. 45, No. 11, 2017, pp. 907-913.
- [64] Lee, B., and Shin, J. "Experimental Study on Jet Characteristics of Sparkjet Actuator with Variation of Discharge Characteristics," *The Korean Society for Aeronautical & Space Sciences 2018 Spring Conference*, 2018, pp. 7-9.
- [65] Anderson, K. V., and Knight, D. D. "Plasma jet for flight control," *AIAA Journal*

Vol. 50, No. 9, 2012, pp. 1855-1872.

- [66] Huang, S., Zhang, Z., Song, H., Wu, Y., Sun, Z., and Li, Y. "Analytic Model and the Influence of Actuator Number on the Performance of Plasma Synthetic Jet Actuator Array," *Applied Sciences* Vol. 8, No. 9, 2018, p. 1534.
- [67] Shin, J. Y., Kim, H.-J., and Kim, K. H. "Development of One-Dimensional Analytic Model for a SparkJet Actuator," *AIAA Journal*, 2020.
- [68] Shin, J. Y., Kim, H.-J., Ahn, S., and Kim, K. H. "A Parametric Study and Analytic Model Development of Sparkjet Actuator Using CFD," *AIAA Scitech 2019 Forum*. 2019, p. 0999.

국문 초록

기존의 유동 제어 장치는 초음속 유동과 같은 고속 유동 제어에는 효과가 미비하기 때문에 많이 활용되지 못하고 있다. 플라즈마 액츄에이터는 운동량 전달과 열 전달 두 가지 방법을 모두 이용해 주변 유동에 교란을 주기 때문에 상대적으로 유동에 미치는 영향력이 다른 유동 제어 장치에 비해 우수하다. 그 중 신세탁 젯 액츄에이터의 일종인 스파크제트 액츄에이터는 비교적 구조가 간단하고 기계적 구동 장치 없이 높은 속도의 제트 유동과 압력파를 발생시킬 수 있기 때문에 고속 유동 제어의 가능성을 인정 받고 있다. 이와 같은 잠재성 때문에 최근까지도 많은 연구가 진행되었지만, 정성적인 연구에 머무는 한계가 있다. 아직까지 스파크제트 액츄에이터의 물리적 특성 파악이 충분히 되지 않았으며, 정량적 성능 평가와 관련된 연구가 전무하기 때문에 실질적인 유동 제어 연구가 어려운 실정이다.

이에 본 연구에서는 평형 플라즈마 해석이 가능한 유동 해석 프로그램을 이용하여 스파크제트 액츄에이터의 전산해석을 수행하고, 액츄에이터의 정성적, 정량적 특성 연구를 수행했다. 먼저 스파크제트 액츄에이터의 제트 유동 특성을 분석하고, 액츄에이터가 발생시키는 추력과 충격량 성능 특성을 분석했다. 그 과정에서 추력의 고속 푸리에 변환을 통해 스파크제트 액츄에이터의 두 특성 주파수를 확인했다. 특성 주파수가 발생하는 원인을 캐비티 내부 유동 구조로 확인했고, 그 진동 형상이 성능에 미치는 영향을 분석했다. 아울러 다양한 설계 변수가

성능 특성에 미치는 영향에 대해 연구했다. 그 결과로 다음과 같은 결론을 도출했다.

스파크제트 액추에이터의 유동은 에너지 주입 초기에 비평형성이 존재하지만, 평형 유동 해석을 수행해도 높은 정확도를 유지하면서 계산 비용을 줄일 수 있다. 제트 유동이 분출되는 동안에도 간헐적으로 압력파가 분출되면서 추력이 심하게 진동한다. 이 때문에 추력 손실과 음의 추력이 발생하지만, 충격량은 대체적으로 단조 증가하여 제트 분출이 끝나는 시점에 특정 값으로 수렴한다. 진동하는 추력을 FFT한 결과 두 개의 고유 주파수를 확인했으며, 이는 캐비티 내부의 반사파 거동에서 기인된다. 높은 고유 주파수를 제 1 고유 주파수로, 낮은 고유 주파수를 제 2 고유 주파수로 명명했다.

전극 모양과 축소각 변경을 통해 다음과 같은 스파크제트 액추에이터의 주파수 특성을 확인했다. r 축 반사파는 제 1 특성 주파수를 발생시키는 원인이며, z 축 반사파는 제 2 특성 주파수의 발생 원인이다. 두 개의 특성 주파수는 서로에게 독립적이다. 제 1 주파수를 제거할 경우, 충격량이 약 11 % 감소하고, 대부분의 진동을 제거했을 때는 충격량이 약 15 % 감소한다. 이를 통해 스파크제트 액추에이터의 성능 예측 및 평가에는 추력의 진동 현상 고려가 필수임을 확인했다. 또한, 액추에이터의 시스템 적용 시 고려해야 할 특성 주파수가 두 개라는 것을 확인했다.

스파크제트 액추에이터의 성능 특성을 확인하기 위해 매개변수 연구를 수행했다. 전극 모양은 충격량 성능에 약 3 %까지 영향을

미친다. 이는 r 축 반사파가 액츄에이터 작동 초기 이후에 소멸하기 때문이다. 에너지 주입 영역의 세장비가 1에서 많이 벗어나면 이와 같은 r 축 반사파 소멸이 발생해서 충격량 성능이 감소한다. 에너지 주입 영역 세장비와 관련된 설계 변수는 전극 지름, 전극 간격, 캐비티 지름이 있다. 축소각 변화에 따라 최대 16 %의 충격량 성능 차이를 보인다. 축소각이 작으면 캐비티 위쪽 벽면과 오리피스 목 사이에서 발생하는 유동 팽창과 박리가 오리피스 목 넓이를 줄이기 때문에 성능이 감소한다. 또한 축소각 변화는 액츄에이터의 원동력을 저하시키는 고온 유동 분출도 야기한다. 고온 유동 분출은 위상이 다른 캐비티 내부의 압력과 공명 현상에 의해 발생한다. 위상이 같은 공명 현상은 고온 유동을 캐비티 내부에 유지시킬 것으로 예상되고, 이에 따라 액츄에이터 성능을 증가시킬 것이다. 공명 현상은 특성 주파수의 비와 캐비티 반지름과 높이 비에 영향을 받는다. 오리피스 지름은 충격량 성능에 최대 약 20 %까지 영향을 미친다. 지름이 클수록 넓어지는 오리피스 목에 따라 분출되는 유량의 증가가 성능 증가의 원인이다. 하지만 오리피스 반지름 증가는 압력파에 의한 압력 강하도 크게 작용하여 충격량이 감소하는 구간도 나타난다. 스파크제트 액츄에이터의 설계 변수와 성능과의 상관 관계를 통해 설계에서 고려할 사항을 제시했다.

주요어: 유동 제어, 플라즈마 유동 제어, 플라즈마 액츄에이터, 스파크제트 액츄에이터, 성능 특성, 주파수 특성, 전산유체역학

학 번: 2016-30184

성 명: 김형진